

Copyright

by

Jacob Allan Adams

2014

**The Thesis Committee for Jacob Allan Adams
Certifies that this is the approved version of the following thesis:**

**Design of Vibrational and Solar Energy Harvesting Systems for
Powering Wireless Sensor Networks in Bridge Structural Health
Monitoring Applications**

**APPROVED BY
SUPERVISING COMMITTEE:**

Supervisor:

Richard H. Crawford

Raul G. Longoria

**Design of Vibrational and Solar Energy Harvesting Systems for
Powering Wireless Sensor Networks in Bridge Structural Health
Monitoring Applications**

by

Jacob Allan Adams, B.S. Mech. Eng.

Thesis

Presented to the Faculty of the Graduate School of

The University of Texas at Austin

in Partial Fulfillment

of the Requirements

for the Degree of

Master of Science in Engineering

The University of Texas at Austin

December 2014

Dedication

This thesis is dedicated to my family, whose encouragement and support has helped me go further than I ever thought possible.

Acknowledgements

I would like to thank Dr. Richard Crawford for not only providing superb technical expertise over the duration of this research, but for being an excellent mentor along the way. I'd also like to thank Dr. Raul Longoria for the all the excellent teachings in the fields of dynamic systems and controls as well as simulation. I am grateful for a fulfilling project opportunity from The National Institute for Standards and Technology's Technology Innovation Program and The University of Texas at Austin. I'd like to thank the researchers who came before me, Eric Dierks, Sumedh Inamdar, and Matthew Reichenbach (among others), who paved the way for my own work. Finally, I'd like to thank my peers, and friends, Brock Dunlap and Kevin Baldrige for always being there and making my time as a graduate student a joy.

December 3, 2014

Abstract

Design of Vibrational and Solar Energy Harvesting Systems for Powering Wireless Sensor Networks in Bridge Structural Health Monitoring Applications

Jacob Allan Adams, MSE

The University of Texas at Austin, 2014

Supervisor: Richard H. Crawford

Structural health monitoring systems provide a promising route to real-time data for analyzing the current state of large structures. In the wake of two high-profile bridge collapses due to an aging highway infrastructure, the interest in implementing such systems into fracture-critical and structurally deficient bridges is greater now than at any point in history. Traditionally, these technologies have not been cost-effective as bridges lack existing wiring architecture and the addition of this is cost prohibitive. Modern wireless sensor networks (WSN) now present a viable alternative to traditional networking; however, these systems must incorporate localized power sources capable of decade-long operation with minimal maintenance. To this end, this thesis explores the development of two energy harvesting systems capable of long-term bridge deployment with minimal maintenance. First, an electromagnetic, linear, vibrational energy harvester is explored that utilizes the excitations from passing traffic to induce motion in a translating permanent magnet mass. This motion is then converted to electrical energy

using Faraday's law of induction. This thesis presents a review of vibrational energy harvesting literature before detailing the process of designing, simulating, prototyping, and testing a selected design. Included is an analysis of the effects of frequency, excitation amplitude, load, and damping on the power production potential of the harvester. Second, a solar energy harvester using photovoltaic (PV) panels is explored for powering the critical gateway component of the WSN responsible for data aggregation. As solar energy harvesting is a more mature technology, this thesis focuses on the methodologies for properly sizing a solar harvesting system and experimentally validating the selected design. Fabrication of the prototype system was completed and field testing was performed in Austin, TX. The results validate the selected system's ability to power the necessary 14 W DC load with a 0° panel azimuth angle (facing direct south) and 45° tilt.

Table of Contents

List of Tables	xi
List of Figures	xii
Chapter 1: Introduction.....	1
1.1 Project Motivation	1
1.2 Project Overview	4
1.2.1 Project Description.....	4
1.2.2 Wireless Sensor Networks.....	6
1.2.3 Powering the Wireless Sensor Network.....	10
1.2.4 Energy Harvesting.....	12
1.3 Research Objectives.....	16
1.4 Thesis Organization	17
Chapter 2: Review of Vibrational Energy Harvesting Literature	19
2.1 Chapter Overview	19
2.2 Comparison of Common Inertial Harvesting Techniques	19
2.3 Summary of Relevant Literature	26
2.3.1 Overview of Electromagnetic Energy Harvester Literature	26
2.3.2 Literature Review of Low Frequency Specific Applications	29
2.4 Review of <i>Evaluating Vehicular-Induced Vibrations of Typical Highway Bridges for Energy Harvesting Applications</i>	36
2.4.1 Field Instrumentation and Data Acquisition.....	36
2.4.2 Spectral Analysis and Initial Findings.....	39
2.4.3 Potential Power Availability	42
2.4.4 Conclusions.....	46
2.5 Review of <i>Design of an Electromagnetic Vibration Energy Harvester for Structural Health Monitoring of Bridges Employing Wireless Sensor Network</i>	47
2.5.1 Numerical Model Development.....	47
2.5.2 Physical Embodiment and Experimental Validation	54

2.5.3 Beta Prototype Embodiment	59
2.5.4 Summary of Work by Dierks	61
2.6 Chapter Summary	61
Chapter 3: Development of Numerical and FEA Simulations	62
3.1 Analytical Model	62
3.1.1 Mechanical Components	62
3.1.2 Analysis of Electromagnetic Components.....	64
3.2 Numerical Simulation	67
3.2.1 Initial Design Decisions and Parameter Selection	67
3.2.2 Performance from Simulation.....	74
3.3 Electromagnetic FEA Analysis	80
3.4 Chapter Summary	82
Chapter 4: Design Embodiment and Experimental Testing	83
4.1 Embodiment	83
4.1.1 Fabrication	83
4.1.2 Prototype Assembly	88
4.2 Experimental Validation	90
4.2.1 Testing Apparatus	90
4.2.2 Experimental Results.....	91
4.2.3 Prototype Parameterization.....	95
4.2.4 Simulation Results with Prototype Parameters.....	99
4.3 Vibrational Harvesting Conclusion	101
Chapter 5: Solar Harvesting Overview and Prototype Validation.....	102
5.1 Overview of Solar Energy Harvesting.....	102
5.1.1 Introduction to Solar Power.....	102
5.1.2 Key Factors in a PV System	104
5.2 Review of <i>Design of a Solar Energy Harvesting System for Structural Health Monitoring Systems</i>	107
5.2.1 Analytical Modeling and Experimentation.....	107
5.2.2 Design Embodiment	112

5.3 Solar Prototype Field Testing	115
5.3.1 Prototype Deployment	115
5.3.2 Field Testing Results	119
5.4 Solar Harvester Conclusions	124
Chapter 6: Conclusions and Future Work	125
6.1 Summary and Conclusions	125
6.2 Future Work	130
Appendix A: Bill of Materials	132
Appendix B: Dimensioned Cross-Sectional View Sketches for Selected Vibrational Harvester Components.....	136
Bibliography	141

List of Tables

Table 1.1. Summary of Wireless Protocol Testing (NIST-TIP, 2014).....	9
Table 1.2. Summary of Power Requirements for WSN components (NIST-TIP, 2014).....	12
Table 1.3. Power Density Comparison of Energy Harvesting Technologies (NIST-TIP, 2014).....	13
Table 2.1. Compilation of Available Harvesters Power Outputs and Power Densities (Patel & Khamesee, 2013).....	29
Table 2.2. Optimization Parameters for Stator and Translator from (von Buren & Troster, 2007).....	35
Table 2.3. Optimal Geometries for Four Evaluated Designs from (von Buren & Troster, 2007).....	35
Table 3.1. Geometric Ratios and Properties Compiled from (von Buren & Troster, 2007)	69
Table 3.2. Translating Mass Parameters.....	71
Table 3.3. Coil Parameters.....	73
Table 4.1. Measured Experimental Prototype Parameters.	99
Table 5.1. PV Simulation Input Parameters (Inamdar, 2012).	107
Table 5.2. Results for Various PV and Battery System Configuration Simulations (Inamdar, 2012).....	110
Table 5.3. Design Specifications for Selected Concept (Inamdar, 2012).	112
Table 5.4. Daily Charge Controller Charge/Load Amp-Hours with Corresponding Cloud Cover Percentage.....	124

List of Figures

Figure 1.1. Age distribution of bridges in the United States (Federal Highway Administration, 2014).	2
Figure 1.2. Under bridge inspection unit, or Snooper, in use (N.E. Bridge Contractors Inc.).	4
Figure 1.3. Schematic of Wireless Sensor Network (WSN) architecture (Reichenbach, 2012).....	7
Figure 1.4. Proposed architecture for NI WSN (NIST-TIP, 2014).....	8
Figure 1.5. Average power requirements for a representative WSN node at varying sample rates (Weaver, Crawford, & Wood, 2010).	11
Figure 1.6. Solar powered waste receptacles (Sanders, 2013).....	14
Figure 2.1. Schematic of In-Plane Overlap Electrostatic Generator under normal operation and under off-axis actuation (Lueke & Moussa, 2011). ..	20
Figure 2.2. Schematic of an In-Plane Gap Closing Generator (Lueke & Moussa, 2011).....	21
Figure 2.3. Schematic of a Laminated Piezoelectric Beam Generator (Lueke & Moussa, 2011).....	22
Figure 2.4. Schematic of an Electromagnetic Generator (Lueke & Moussa, 2011).23	
Figure 2.5. Summary of common electromagnetic energy generators, including (a) Perpetuum VEH, (b) Guardian Shake Flashlight, (c) Seiko Kinetic Perpetual Watch, and (d) alternators in hydroelectric plant (Perpetuum; Survival Universe; Seiko (2014); Library of Congress (2014)).	25
Figure 2.6. Schematic for a vibrational generator (Williams & Yates, 1996).....	26

Figure 2.7. Plot of frequency spectrum of power generation around the resonance frequency of the generator for various damping factors (Williams & Yates, 1996).....	28
Figure 2.8. Bridge-specific energy harvester concepts form Clarkson University - (a) (Li & Pillay, 2007), (b&c) (Li & Pillay, 2011).	31
Figure 2.9. Assorted body-worn EM harvesters – (a) (Saha, O'Donnell, Wang, & McCloskey, 2008), (b) (Patel & Khamesee, 2013), (c) (von Buren & Troster, 2007)	32
Figure 2.10. Flowchart for geometry optimization (von Buren & Troster, 2007).	34
Figure 2.11. Image of I-35N Bridge over Medina River (Reichenbach, 2012)....	37
Figure 2.12. Under-view of Medina River Bridge with key components highlighted (Reichenbach, 2012).	38
Figure 2.13. Comparison of three sample PSD outputs: (A) Medina River Bridge, (B) US-290 Bridge, and (C) TX-71E Bridge (Reichenbach, 2012).....	40
Figure 2.14. Second modal frequency and temperature tracked as a function of time for TX-71E Bridge (Reichenbach, 2012).	41
Figure 2.15. Response spectrum for sample acceleration history for Medina River Bridge (top), US-290 Bridge (middle), and TX-71E Bridge (bottom) (Reichenbach, 2012).	43
Figure 2.16. Average weekly power response spectra for the five instrumented highway bridges (Reichenbach, 2012).	45
Figure 2.17. Average weekly power response spectrum for Medina River Bridge with 1.454 kg mass (Reichenbach, 2012).	46
Figure 2.18. Peak power under increasing swept sine wave over 120 seconds at 0.05 g amplitude and 2.9 k Ω load (Dierks, 2011).	48

Figure 2.19. Peak harvested power for amplitude sweep under sinusoidal excitation at 2.2 Hz and 2.9 kΩ load (Dierks, 2011).	48
Figure 2.20. Peak harvested power for load resistance sweep under sinusoidal excitation at 2.2 Hz and 0.01 g amplitude (Dierks, 2011).	49
Figure 2.21. Peak harvested power for load resistance sweep under 50 seconds of IH-35N-US-290E direct connector acceleration data (Dierks, 2011).	49
Figure 2.22. Bridge acceleration, relative displacement, peak harvested power, and harvested energy for 300 second of IH-35N-US-290E direct connector acceleration (Dierks, 2011).	52
Figure 2.23. Non-linear spring case for energy harvested for 300 seconds of IH-35N-US-290E direct connector (Dierks, 2011).	53
Figure 2.24. Solid model of (Dierks, 2011) test prototype.	54
Figure 2.25. Peak harvested power as a function of peak acceleration amplitude for a sinusoidal excitation at 2.2 Hz and 14 kΩ load (Dierks, 2011).	56
Figure 2.26. Peak harvested power as a function of increasing and decreasing frequency sweeps with acceleration amplitude of 0.01 g and load resistance of 14 kΩ (Dierks, 2011).	57
Figure 2.27. Peak harvested power as a function of time for bridge excitation from Medina River Bridge with a load resistance of 14 kΩ (Dierks, 2011).	58
Figure 2.28. Peak harvested power as a function of time for bridge excitation from Medina River Bridge with a load resistance of 14 kΩ and non-linear springs (Dierks, 2011).	59
Figure 2.29. Solid model of beta prototype (Dierks, 2011).	60
Figure 2.30. Completed harvester isometric and rear isometric views (Dierks, 2011).	60

Figure 3.1. Complex friction model (MathWorks, 2014).....	64
Figure 3.2. Spectral analysis results for 5 spans of the IH-35N-US-290E Bridge.	72
Figure 3.3. Load resistance sweep at 2 Hz sinusoidal frequency and 0.01 g amplitude.	74
Figure 3.4. Oscillation amplitude sweep with 2 Hz resonant frequency and 2.75 k Ω load resistance.....	75
Figure 3.5. Excitation frequency sweep for harvester tuned to 2 Hz resonant frequency at 2.75 k Ω load resistance.	76
Figure 3.6. Acceleration excitation (1), the associated relative displacement (2), instantaneous power output (3), and energy dissipated in load (4) for 300 seconds of data from the IH-35N-US-290E Bridge at 1.8 Hz resonant frequency and 2.75 k Ω load resistance.	77
Figure 3.7. Energy dissipated in load for 300 seconds of data from the IH-35N-US- 290E Bridge at 2 Hz resonant frequency and 2.75 k Ω load resistance.	78
Figure 3.8. Energy dissipated in load for 300 seconds of data from the IH-35N-US- 290E Bridge at 1.8 Hz resonant frequency, 2.75 k Ω load resistance, and increased damping ratio.....	79
Figure 3.9. Energy dissipated in load for 300 seconds of data from the IH-35N-US- 290E Bridge at 2 Hz resonant frequency, 2.75 k Ω load resistance, and increased damping ratio.....	79
Figure 3.10. (a) FEA solid model (b) shaded plot of resultant flux density and field contour lines.....	81
Figure 4.1. (a) Unwound coil bobbin after machining, (b) Finished, wound coil stator.	84
Figure 4.2. Completed stator mounts with coil assembly positioned.....	85

Figure 4.3. Completed translating magnetic mass assembly.	86
Figure 4.4. Finished bearing and mount assembly.	87
Figure 4.5. Top end cap with threaded brass rod attached to helical spring and shaft.	88
Figure 4.6. Completed harvester assembly with components labeled.	89
Figure 4.7. Schematic of laboratory testing apparatus.	90
Figure 4.8. Frequency sweep results for 7 k Ω load and 0.25 g amplitude.	92
Figure 4.9. Peak harvested power as a function of load resistance at 1.91 Hz excitation frequency and 0.25 g amplitude.	93
Figure 4.10. Peak harvested power under varying excitation amplitudes with 6.95 k Ω load resistor and 1.91 Hz excitation frequency.	94
Figure 4.11. Instantaneous harvested power (bottom) under replicated IH-35N Medina River Bridge acceleration data (top) with 6.95 k Ω load.	95
Figure 4.12. Load testing results to determine spring stiffness for prototype spring.	96
Figure 4.13. Sample of LabVIEW VI Front Panel used to calculate logarithmic decrement and associated damping ratio.	98
Figure 4.14. Simulation results for actual harvester parameters from Table 10. .	100
Figure 5.1. Solar irradiation spectrum at Earth’s atmosphere and surface (LASP, 2014).	104
Figure 5.2. Angles of interest for solar panel power output (Goswami, Kreith, & Kreider, 2000).	106
Figure 5.3. Average daily energy output for various tilt angles of a 50 W panel in Austin, TX (Inamdar, 2012).	108

Figure 5.4. Average daily energy output for various azimuth angles of a 50 W panel in Austin, TX (Inamdar, 2012).	109
Figure 5.5. Comparison of daily energy production (Inamdar, 2012).	111
Figure 5.6. Solid model of selected concept (Inamdar, 2012).	113
Figure 5.7. Color coded diagram of PV mount with part materials, fixtures, and forces listed (Inamdar, 2012).	114
Figure 5.8. Sample FEA simulation results with factor of safety highlighted for panel in 90 degree configuration (Inamdar, 2012).	114
Figure 5.9. Front view of PV panel, mount, and enclosure.	116
Figure 5.10. Rear view of PV panel, mount, and enclosure.	116
Figure 5.11. Internal view of the enclosure with associated electronics.	117
Figure 5.12. Comparison of enclosure temperature to ambient air.	119
Figure 5.13. Solar harvester power data from two weeks of testing.	120
Figure 5.14. Typical daily PV power output for 24 hour period in January.	121
Figure 5.15. Representative charging break-down for Li-ion batteries (Battery University, 2014).	122
Figure 5.16. Daily Ah charge and load over 60 days of data acquisition.	123

Chapter 1: Introduction

1.1 PROJECT MOTIVATION

A healthy national highway infrastructure has proven critical to the long-term success of the United States economy. These ubiquitous structures are the arteries that enable the American populace to successfully, and efficiently, distribute goods and services throughout the country. This national infrastructure has become so important that the annual miles of travel on the nation's roadways increased nearly every year from 1957 to 2007 and saw an almost five-fold total increase over that time-frame (Federal Highway Administration, 2012). Therefore, it must be of the highest priority for the owners and maintainers of these structures to effectively, and with minimal interruption to traffic, ensure they remain safe and able to adequately support the nation's needs.

Working in opposition to this goal is an ever-aging roadway network that must be constantly monitored, repaired, and upgraded to meet the increasing demand of American traffic. Perhaps the most important cogs in this roadway network are the bridges used to span the gaps in the traditional asphalt and concrete roadways, especially given their relative levels of sophistication, scale, and engineering complexity. Understanding how to efficiently inspect and monitor these structures becomes even more important when realizing that more than one third of the United States' bridges are at least 50 years old (Federal Highway Administration, 2014). Figure 1.1 illustrates the break-down of bridges in the US by age.

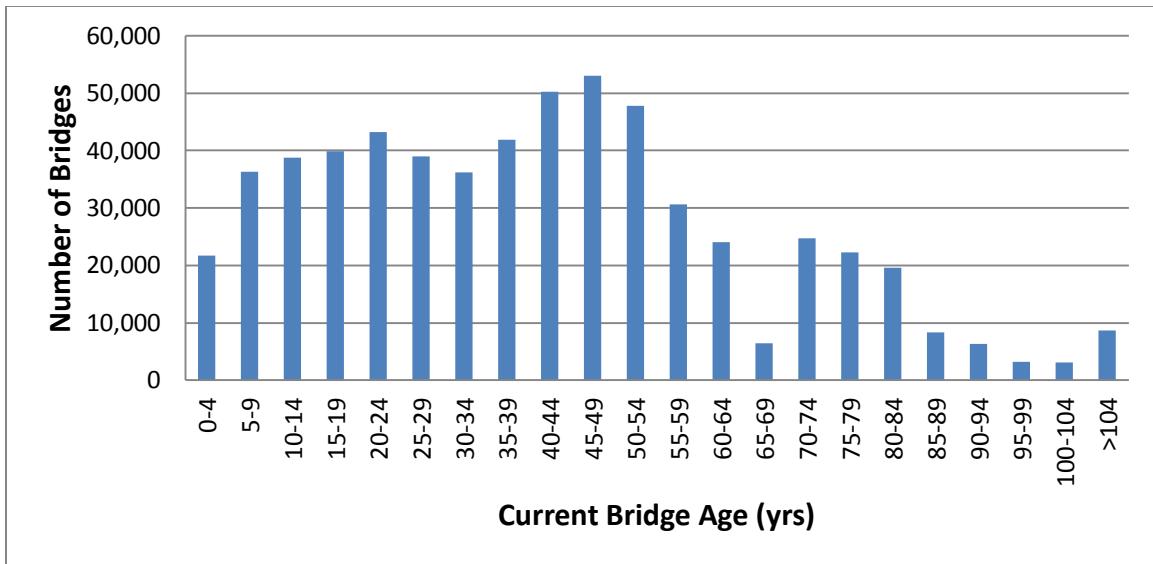


Figure 1.1. Age distribution of bridges in the United States (Federal Highway Administration, 2014).

While this information alone may not be a clear indicator of a bridge’s current health, it is indicative of an aging infrastructure that likely needs the aid of modern techniques to fully scrutinize. In addition, according to the Federal Highway Administration (FHA), 147,870 of 607,751 (24.3%) of the bridges in the United States were deemed either structurally deficient or functionally obsolete as of December 2013 (Federal Highway Administration, 2014). While holding one of these statuses does not inherently mean a bridge is unsafe, two recent high-profile bridge collapses indicate that these labels should be taken seriously. The I-5 Bridge over the Skagit River in Mount Vernon, WA collapsed when an exceptionally tall load struck a steel girder, injuring three people on the bridge at the time (Bello, 2013). This bridge was listed as functionally obsolete by the FHA in the National Bridge Inventory (NBI) database (The National Bridge Inventory Database). Similarly, the I-35 Bridge in Minneapolis, MN was listed as

structurally deficient when it collapsed in 2007, killing 13 people (Federal Highway Administration, 2012).

In order to prevent these types of tragedies from occurring, the FHA has implemented a set of National Bridge Inspection Standards (NBIS) to regulate the regular bridge inspections. These guidelines dictate that the standard bridge inspection interval should be at minimum biennially. On its surface, this may seem adequate; however, a review of the inspection interval for the I-35 Bridge in Minneapolis indicates its last inspection was just over one year before its collapse (Federal Highway Administration, 2012).

Traditionally, these inspections have been carried out in a manual fashion by trained individuals riding in large inspection trucks with articulating arms, known as Snoopers (Figure 1.2). This sort of manual inspection tends to require considerable financial and human resources. During the inspection process, highway lanes must be closed for the inspection unit, furthering the burden by disrupting the flow of traffic and requiring additional personnel to regulate traffic flow. Manual inspection also introduces a degree of human error that can lead to discrepancies in inspection detail between individual inspectors. While these manual inspections certainly serve an important purpose in the bridge-health monitoring process, it seems that an opportunity exists to implement a structural health monitoring system that relies less on direct human access to better understand a bridge's current status. Implemented as a supplement to the traditional inspection methodology, a cost-effective system could provide up-to-date information with high precision and a much lower investment in overall human resources.



Figure 1.2. Under bridge inspection unit, or Snooper, in use (N.E. Bridge Contractors Inc.).

1.2 PROJECT OVERVIEW

1.2.1 Project Description

Following the 2007 I-35 bridge collapse, the National Institute of Standards and Technology (NIST) allocated funds through its Technology Innovation Program (TIP) for several research projects geared at developing infrastructure monitoring and improving the inspection practices of civil infrastructure, specifically those related to bridges. In particular, a joint venture was funded entitled, “Development of Rapid, Reliable, and Economical Methods for Inspection and Monitoring of Highway Bridges”. The project was a multi-discipline collaboration led by The University of Texas at Austin, and included efforts from National Instruments Corporation (NI, Austin, TX, USA) and the

engineering firm Wiss, Janney, Elstner Associates, Inc. (WJE, Northbrook, IL, USA), beginning February 2009 and completed in January 2014.

The project's goal was to develop a pair of complimentary sensor networks for bridge inspection. Specifically, the goals were the development of an active, self-powered system for continuous monitoring for cracks or defects in fracture-critical bridges and a passive system for monitoring corrosion in reinforced concrete bridge decks (National Institute of Standards and Technology, 2009). Fracture-critical bridges – those susceptible to collapse from the failure of a single critical component, such as the I-5 Skagit River Bridge – were identified as the primary structures in need of such a health monitoring system due to their increased chance of catastrophic failure. It should be noted, however, that lessons learned from such a system could be applied beyond these bridges to a broad range of civil infrastructure.

The project was split among several distinct entities, the largest of which is the team from The University of Texas at Austin (UT). Within this group, a broad range of students and faculty collaborated from the Departments of Civil, Architectural, and Environmental Engineering, Mechanical Engineering, and Electrical and Computer Engineering. The structural engineering team from the Department of Civil, Architectural, and Environmental Engineering served as overall project managers. Based in the Ferguson Structural Engineering Laboratory (FSEL) at UT's Pickle Research Campus, the structural team's efforts focused on the instrumentation and data acquisition of bridges, evaluation and analysis of measured responses, and reliability testing of sensors (Reichenbach, 2012). The Mechanical Engineering team focused on developing innovative energy harvesting technologies to power the sensing equipment and maintain the wireless nature of the system. The Electrical and Computer Engineering Department focused on the passive sensor technologies.

In addition to the large research team at UT, engineers at National Instruments were enlisted to develop the wireless applications. An existing product from NI was leveraged initially, and further work was completed to meet requirements specifically mandated by the NIST-TIP project. Consultants from Wiss, Janney, Elstner Associates were brought in to provide expert insight from their previous field work in instrumentation and the demands of developing a system database to be used for the amalgamation of the real-time data being generated.

1.2.2 Wireless Sensor Networks

Developing a wireless network of sensors, as opposed to a standard wired network, offers several distinct advantages in a bridge health monitoring application. When considering the deployment of a wired system across a large bridge, it is critical to examine the labor and financial expenses involved. Bridges are usually large structures that require many thousands of feet of cabling to maintain traditional network connectivity; this likely means that large-scale infrastructure deployments are cost and labor prohibitive. Additionally, as bridges come in a variety of types and sizes, extensive preparation work is required to prepare for an individual bridge. By implementing a wireless network, this need to run vast lengths of cable can be mitigated as the primary data transfer can be accomplished wirelessly. The nature of a wireless network also provides an easy avenue for scalability. Wireless sensor networks (WSN) tend to have localized access points for data acquisition which can be added as necessary, depending on the desired instrumentation scale. This provides increased flexibility and lower costs when compared to traditional wired measurement systems (National Instruments).

Wireless sensor network architecture generally consists of several components: localized nodes directly connected to the sensing equipment, intermediate routers that

pass data through the network, and centralized gateways that compile the data and perform most of the necessary post-processing work. This is schematically illustrated in Figure 1.3 below. This multi-tiered scheme makes for a robust system that is more resilient than a wired system that could be crippled by a hardware failure in a single networking component. The nodes can be deployed as necessary to the locations of greatest interest with minimal impact on other components. In the event of a single node hardware failure, the remaining components of the system should be unaffected. The routers, which act as intermediaries in data transmission, can often be deployed in a manner that leads to some redundancy in the event of a failure. This leaves only the gateway as a device that can cripple the system in the event of a single hardware failure. However, an advantage of such a wireless system is that the gateway can often be positioned in a particularly “safe” location. This is important for deployments such as bridges where harsh environmental conditions are common.

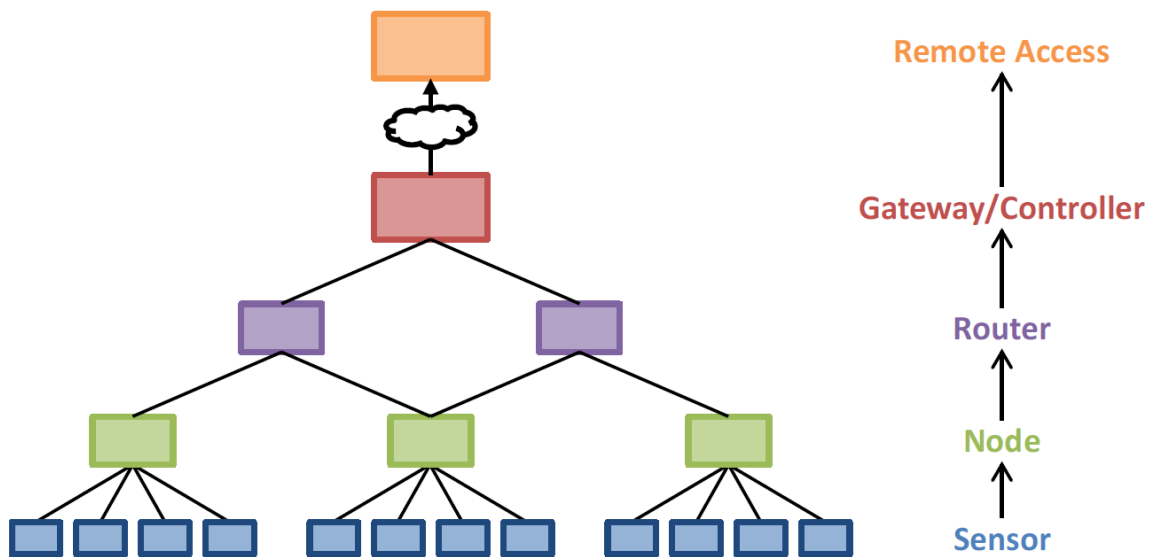


Figure 1.3. Schematic of Wireless Sensor Network (WSN) architecture (Reichenbach, 2012).

For the NIST-TIP project, the team elected to leverage an existing WSN that was developed by National Instruments. This served two primary purposes: (1) using off-the-shelf technology simplifies the scope of the project and reduces complexity; (2) this added a renowned company with a strong engineering background in wireless technology to the team. NI's WSN system incorporates two primary types of hardware, a gateway and a series of nodes. The nodes are developed for both generic sensor measurements (such as analog voltages) as well as niche units designed to work with specific types of sensors. The gateways have greater processing capability and can universally communicate with any combination of the series of nodes. The nodes have their own onboard processing capabilities, although more limited, and function as both the data acquisition point as well as the router access points (National Instruments). This architecture is depicted in Figure 1.4.

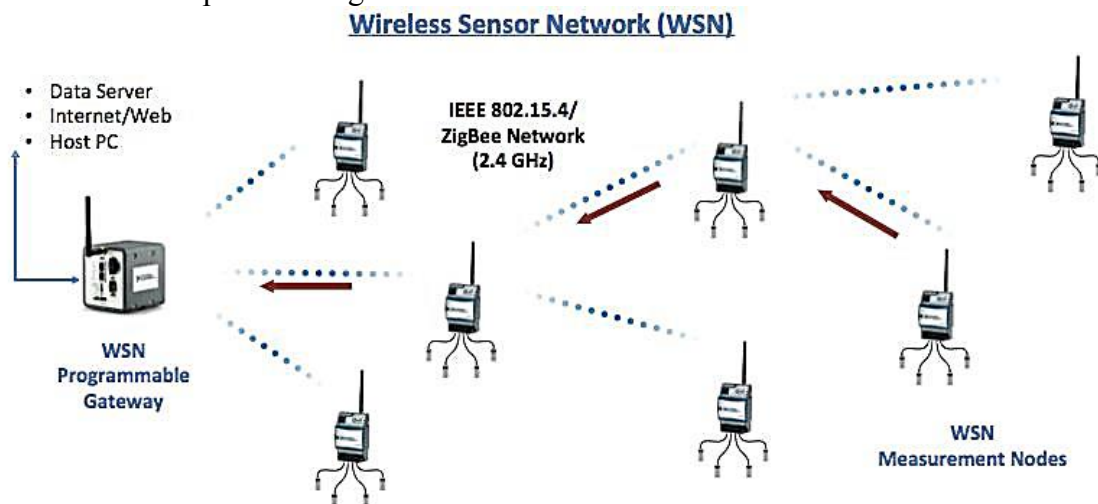


Figure 1.4. Proposed architecture for NI WSN (NIST-TIP, 2014).

Two key aspects that were investigated by the project were the most efficient wireless protocol for the project and methods for database management and interaction. Two readily available wireless technologies were examined and evaluated on five bridges

in Texas. The first, WiFi based on IEEE 802.11 standards, is ubiquitously used in general-purpose networking. The second, ZigBee based on IEEE 802.15.4, is a standard for low-rate and low-power networks. WiFi provides high data transmission rates, but is not optimized for low power operation; while, ZigBee includes power management features, longer range, and supports mesh networking for easily extending networks (NIST-TIP, 2014). The results of the testing are summarized in Table 1. Based on this, the team elected to proceed with ZigBee as the chosen wireless networking protocol.

Table 1.1. Summary of Wireless Protocol Testing (NIST-TIP, 2014).

Observation and Conclusions	Benefit
Narrowband nature of IEEE 802.15.4 reduces vulnerability to multi-path interference	More reliable in steel bridge structures where multipath effects are prevalent
IEEE 802.15.4 radios support longer range (in addition to formation of mesh networks)	Increased coverage of bridge structures; more reliable wireless communication
IEEE 802.15.4 supports low-power operation	More appropriate for long-term monitoring
High-gain and directional antennas do not improve performance significantly in bridge structures	Lower cost systems (specialized antennas not required)

In an effort to bring the system to a deployment ready state, the team from Wiss, Janney, Elstner Associates, Inc. developed a user interface that can easily be operated from a handheld tablet computer. This enables easy modification and visualization of the programming currently running on the system. WJE also worked to develop an enterprise management solution to compile the data generated by the sensor networks. This solution utilizes Cloud-based computing for easy data aggregation. By attaching a wireless cellular modem to each gateway, the system can upload data to this Cloud database in real-time. The team believes this system provides a viable solution that will not require engineers specialized in programming software to be on site during the data acquisition system installation (NIST-TIP, 2014).

1.2.3 Powering the Wireless Sensor Network

One major challenge facing the development of a truly wireless network is the source of power for the gateway and nodes. As bridges are often not pre-wired for grid electricity, alternative solutions must be examined. Attaching a bridge to an existing power grid faces many of the same challenges as wiring for data transfer, namely it is costly and labor intensive. Additionally, bridges in rural locations require additional efforts as existing power transmission lines may not be locally available. Similarly, using large generators at the bridge location still involves extensive wiring. Thus, wireless power sources are preferred for many implementations. As technology has become increasingly handheld, the rise of battery technology has been significant. Thus, it is logical to consider pre-charged batteries for this application. However, the proposed WSN is expected to have a life-cycle of at least ten years with minimal maintenance. Even with modern battery energy densities, this requires several battery changes over the life of the system. This is cost-intensive and is not ideal as a long-term solution.

As part of the project, Weaver, Crawford, and Wood (2010) examined the average power requirements of a representative WSN node. Figure 1.5 represents the results for a node under a variety of sampling rates. A critical takeaway is that the individual components of the WSN have differences in power requirements that are orders of magnitude apart. Powering a node in router mode, which requires it to always be powered on and available for passing data, can require more than 200 mW average power. Similarly, having an “always on” node that samples infrequently (<1/min) requires up to two orders of magnitude less average power than the much faster sampling techniques considered for this project.

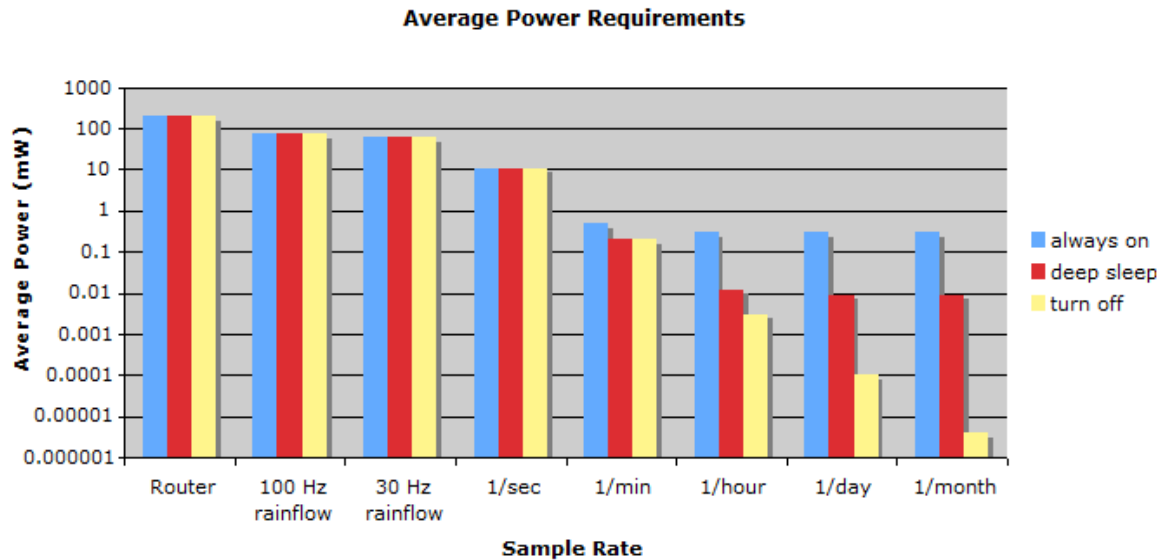


Figure 1.5. Average power requirements for a representative WSN node at varying sample rates (Weaver, Crawford, & Wood, 2010).

As might be expected, the gateway requires significantly more power; testing revealed that it consumes approximately 10 W of average power. A summary of the expected required power broken down by component is provided in Table 2. Given the vastly different power requirements of the constituent components, different power sources were examined based on the individual need. Specifically, the team elected to investigate several possible avenues of harvesting energy from available environmental sources. Utilizing energy harvesting techniques to provide localized power sources eliminates the need to run power distribution networks across the bridge structure. In addition, given the large variety of techniques currently being utilized, different components can be sized based on the design requirements.

Table 1.2. Summary of Power Requirements for WSN components (NIST-TIP, 2014).

Scenario	Description	Average Power	Yearly Energy	
Router mode	Radio always transmitting	207 mW	6.53 MJ	1.81 kWh
Rainflow mode	Sampling at 30 Hz (10 weeks) / hourly rest of year	60.7 mW (30Hz) 0.3 mW (hourly)	375 kJ	104 Wh
Hourly mode	One sample / hour	0.3 mW	9.47 kJ	2.63 Wh
Deep sleep mode	One sample / day (with deep sleep)	0.009 mW	284 J	79 mWh
Gateway	cRIO or NI 9792 gateway node	10 W	315 MJ	87.6 kWh

1.2.4 Energy Harvesting

In a world that increasingly requires technology to be more mobile, battery technology is gradually improving and the power requirements of electronics have generally dropped; however, they are still not keeping pace with the demands of many WSN applications (Gilbert & Balouchi, 2008). Therefore, there is considerable movement towards finding solutions from the available environmental energy. Numerous energy sources have been exploited on all scales; these include ambient light, wind, thermal gradients, vibrational sources, and more. Each has advantages and disadvantages based on environmental conditions, energy requirements, mounting locations, and spatial restrictions.

For this project, preliminary work by Weaver, Crawford, and Wood (2010) analyzed three common means of energy harvesting that could feasibly be implemented in a bridge setting. The three potential technologies examined were solar energy harvesting using photovoltaic cells, wind energy using turbines, and vibrational energy via either piezoelectric or inductive technologies. The practical maximum energy density – based on typical environmental conditions and realistic efficiencies – is highlighted in Table 3.

Table 1.3. Power Density Comparison of Energy Harvesting Technologies (NIST-TIP, 2014)

Domain	Model	Theoretical maximum	Practical maximum	Parameters
Solar (direct)	$P=\eta EA$	100 mW/cm ²	3,750 μW/cm ²	1 kW/m ² irradiation, 15% efficiency, 6 hours insolation
Wind	$P=0.5\rho Sv^3C$	4.5 mW/cm ²	380 μW/cm ²	5 m/s, 5% conversion eff.
Vibration	$P=m\zeta_e A^2/4\omega\zeta_t^2$	19 mW/cm ³	300 μW/cm ³	Tungsten mass, 1 Hz, .01 ζ_e , 0.02 ζ_t

A comparison of the practical maximum power densities quickly reveals that solar power has an order of magnitude greater potential than either wind or vibration. Even with this information, it is important to keep the constraints of each energy domain in mind when selecting for a particular application. Solar energy harvesting has become a prominent choice for replacing grid power in lower power applications where access to existing infrastructure is difficult and sunlight is plentiful. Lights attached to LED safety signs, electric fence chargers, spotlights, and even trash compactors in public waste receptacles, such as those in Figure 1.6, can commonly be seen with photovoltaic power sources.



Figure 1.6. Solar powered waste receptacles (Sanders, 2013).

Such devices provide evidence that solar energy can potentially power comparable devices, such as components in a wireless sensor network. It must be noted, however, that these devices all require ample direct sunlight for adequate electricity generation. Removing the solar harvester from direct sunlight reduces the energy density up to three orders of magnitude ($\sim 10 \mu\text{W}/\text{cm}^2$) (Lueke & Moussa, 2011). While bridge applications will largely have direct sun access, this means the panels must extend beyond the existing bridge structure and cannot be tucked away underneath. This may be undesirable if many panels are required to power individual devices. Similarly, using a large centralized array requires the same large-scale wiring efforts as grid power sources.

Similar constraints can be seen with both wind and vibration energy sources. Wind energy requires turbines positioned to maximize the ambient wind speed. As part of

this project, a constraint was provided by potential adopters of such a system that no component may hang below the lowest part of the bridge. As such, McEvoy (2011) concluded that such a device's power output is highly dependent on the depth of the girders of the bridge. This information, combined with normal wind pattern fluctuations, means that the capabilities of such a system will vary greatly depending on geographical installation location and bridge geometry.

Most vibration harvesters described in the literature have the advantage of being small enough to easily install on bridge girders without hanging below the bridge structure. Unlike solar or wind applications, they require no components be positioned outside the existing bridge structure for effective energy harvesting. While vibration harvesting has the lowest energy density of the three proposed methods, this installation advantage makes it desirable for localized installs powering low energy consumption components, namely the nodes in the WSN. Reichenbach (2012) found, however, that the available vibrational energy is highly dependent on bridge design, geometry, and traffic patterns.

As the NIST-TIP project has been completed at the time this thesis is being written, much of the energy harvesting research undertaken by the team was completed beforehand. Wind harvesters were explored thoroughly by McEvoy (2011) and Zimowski (2012); therefore, their work was not expanded upon. Solar harvesting techniques were researched by Inamdar (2012) with some success, but prototyping work was not completed. Chapter 5 of this work focuses on testing the prototype begun by Inamdar. The general viability of bridge vibrations for powering energy harvesters was explored by Reichenbach (2012). In addition, Dierks (2011) explored the design and prototyping of a harvester for bridge health applications. Chapters 2-4 of this thesis explore and expand upon their findings.

1.3 RESEARCH OBJECTIVES

This research focuses on two primary objectives. The first is to design and construct an electromagnetic energy harvester to provide 0.5 mW average power for an NI WSN node using available bridge excitations. This objective is broken down into the following tasks:

- *Analyze appropriate literature to guide design development decisions;*
- *Select a harvester topology optimized for the low excitation frequency deployment locations found in bridge structures;*
- *Develop a numerical simulation to explore key design parameters and predict harvester performance;*
- *Use finite element analysis software to verify the selected design topology and finalize relevant parameters;*
- *Fabricate a high-precision prototype of the selected concept;*
- *Test and validate the experimental prototype; and*
- *Analyze the results within the project requirements.*

The second objective focuses on the completion of the solar harvesting prototype. For this project, the primary goal is to produce a photovoltaic system capable of powering a static DC 14 W load indicative of an NI WSN Gateway and cellular modem. This objective requires the following tasks:

- *Complete fabrication of the selected prototype design;*
- *Select a location for field testing representative of a bridge structure;*
- *Monitor internal electronics temperatures to ensure the selected enclosure provides adequate thermal safety; and*
- *Experimentally validate the prototype for long-term power generation capability using a real-world load test.*

1.4 THESIS ORGANIZATION

Chapter 1: Introduction

The NIST-TIP project is introduced and motivation is discussed. The concept of wireless sensor networks is introduced and the architecture is explored. Specific project power requirements are analyzed. Finally, the research objectives are presented.

Chapter 2: Review of Vibrational Energy Harvesting Literature

An overview of inertial energy harvesting techniques is described. The focus is then narrowed to electromagnetic energy harvesting systems, specifically focusing on low frequency applications. Finally, two previous NIST-TIP team members' work is reviewed and summarized to serve as an introduction to further work.

Chapter 3: Development of Numerical and FEA Simulations

The physical principles of EM energy harvesting are explored to create an analytical model. A design topology is selected to aid in the parameterization of the model. The analytical model is transformed into a numerical simulation to explore key design parameters and predict harvester performance. Lastly, an EM FEA model is developed to finalize design parameters and serve as proof of concept.

Chapter 4: Design Embodiment and Experimental Testing

A prototype is produced and the manufacturing process documented. Laboratory testing is undertaken and the results are presented in the context of the design requirements. Recommendations for future development of EM harvesters for this application are presented.

Chapter 5: Solar Harvesting Overview and Prototype Validation

A brief overview of solar harvesting is provided. The work of NIST-TIP team member Inamdar is presented to provide context. The solar harvesting prototype is analyzed and a field testing summary provided.

Chapter 6: Conclusions and Future Work

This chapter serves as a summary of the work presented in Chapters 1-5. Final recommendations are provided and future work is discussed.

Chapter 2: Review of Vibrational Energy Harvesting Literature

2.1 CHAPTER OVERVIEW

Electromagnetic induction has been widely studied and implemented since its discovery in 1831 by Michael Faraday. With nearly 200 years of research since its inception, it is generally considered a mature technology with many applications in use today. This chapter provides an introduction to electromagnetically based vibrational energy harvesting and a review of the relevant literature used during this research project.

Section 2.2 provides a review and comparison of inertial energy harvesting techniques commonly in use. This is refined to a study of the available literature deemed most valuable to the specific goals of this research in 2.3. The final two sections provide a more comprehensive review of the work previously completed by members of the NIST-TIP team. Work done by Reichenbach (2012) provides a feasibility study of the potential for using an induction-based energy harvester in several representative bridge applications. This work provides a theoretical baseline that a physical harvester prototype can achieve based on acceleration data gathered from sample bridges. Dierks (2011) provides a first iteration of an electromagnetic harvester design and is the basis for much of the work performed for this thesis. Given that these works are directly applicable to the goals of this project, their reviews provide an introduction to the research conducted for this project.

2.2 COMPARISON OF COMMON INERTIAL HARVESTING TECHNIQUES

There are three primary types of vibrational, or inertial, generators commonly referenced in literature. The first is the electrostatic harvester. Figure 2.1 below represents the basic concept. In these devices, power is generated by a capacitance variance that causes charge transfer when the device moves. This movement is driven by

placing the device in the correct plane for scavenging the vibrations available in its environment. For these devices to function, the capacitor must be held in a charged state; therefore, some polarization source must be present in the device. Generally, this is accomplished using an electret layer or charge pump. The electret layer is often simply a silicon wafer with layers of silicon oxide and charged silicon nitride that is attached to the capacitor during manufacturing.

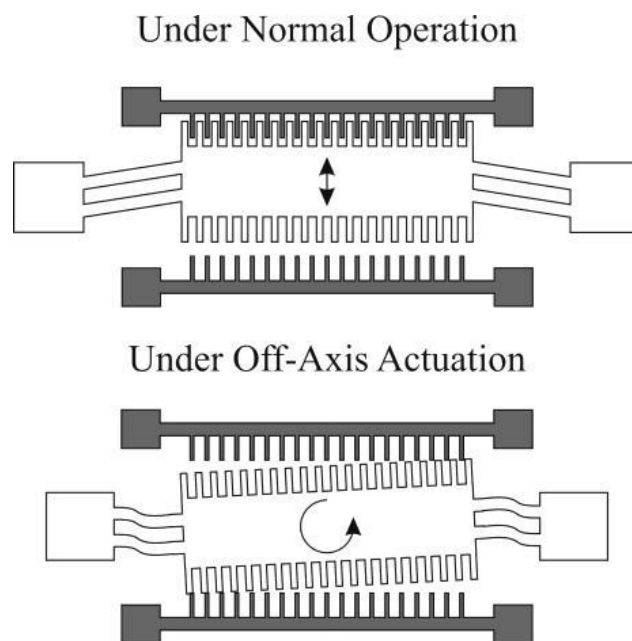


Figure 2.1. Schematic of In-Plane Overlap Electrostatic Generator under normal operation and under off-axis actuation (Lueke & Moussa, 2011).

Under normal operation, electrostatic harvesters have shown fairly large power outputs ranging from 20 to $\sim 120 \mu\text{W}/\text{cm}^2$ (Lueke & Moussa, 2011). The outputs can vary greatly depending on the input vibration frequency, amplitude, and harvester orientation. Like all vibrational harvesters, the device must be optimized based on the vibrations available in the deployment environment. As noted, the device can be modified to harvest

vibrations in several orientations. Figure 2.1 above presents the basic ‘in-plane overlap’ version of the device; while, Figure 2.2 below shows the ‘in-plane gap closing’ variant. An ‘out-of-plane gap closing’ version of the device can also be created but is not pictured. The best orientation is likely based on the available vibrations and confining geometry for an individual location. Besides the need for a polarization source, the greatest challenge in implementing an electrostatic harvester is that off-axis actuation is difficult to control for. The second image in Figure 2.1 represents the off-axis acceleration a harvester might experience. If the device is not carefully designed, electrical contact and shorting can result.

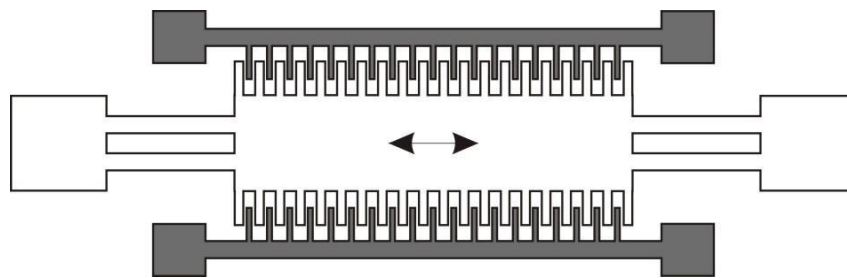


Figure 2.2. Schematic of an In-Plane Gap Closing Generator (Lueke & Moussa, 2011).

Piezoelectric devices have become commonplace in many sensors and actuators, especially in the microelectromechanical systems (MEMS) world. In addition to serving as effective sensors and actuators, piezoelectric materials can also be capable generators of electricity. A piezoelectric device produces power due to the direct piezoelectric effect. This is the phenomenon that occurs when the crystal structure of a piezoelectric material is loaded. In order to maintain electrical equilibrium, electrons within the material become mobile and shift, creating an electrical current. Standard piezoelectric devices use a mass, known as a proof mass, on the end of a cantilever beam that is sandwiched

between layers of piezoelectric thin films. While the piezoelectric materials will react to loading in any direction, the use of a cantilever beam dictates a particular oscillation direction. Figure 2.3 illustrates a basic piezoelectric energy harvester.

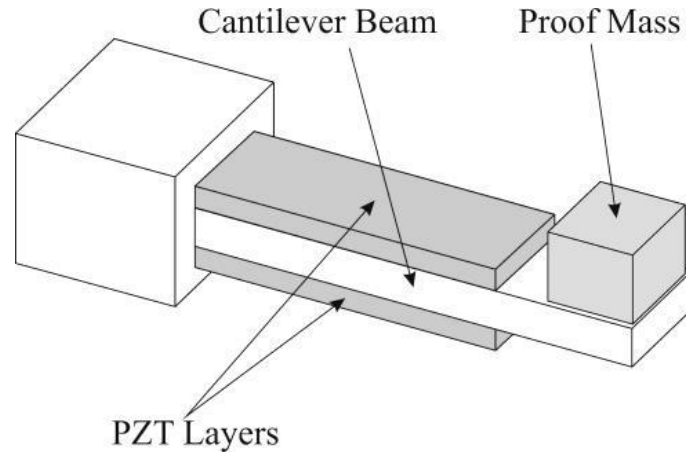


Figure 2.3. Schematic of a Laminated Piezoelectric Beam Generator (Lueke & Moussa, 2011).

There are three primary piezoelectric materials in use today: lead zirconate titanate (PZT), zinc oxide (ZnO), and aluminum nitride (AlN) (Lueke & Moussa, 2011). For power generation purposes, the PZT thin film is generally regarded as the best material as it has a piezoelectric coefficient that is an order of magnitude larger than either ZnO or AlN. ZnO and AlN are primarily utilized in sensors and actuators as they are slightly easier to fabricate. Piezoelectric harvesters tend to excel in systems with vibration frequencies in the hundreds or thousands of Hz as they are difficult to design to resonate at lower frequencies due to their high stiffness and impedance (Dierks, 2011). While this makes them viable in many higher energy, regular vibratory systems, such as those found on manufacturing machinery, developing a system to resonate at the <10 Hz typically seen in bridges may prove challenging.

The final common type of vibrational energy harvester is the electromagnetic harvester. This type of device relies on the principles of electromagnetic induction discovered by Michael Faraday and is described mathematically by Faraday's law of induction. The electromagnetic energy harvester is traditionally a fairly simple device composed of a permanent magnet and metallic coils. When the magnets move in relation to the metallic coils a change in the magnetic flux is introduced in the coils. This changing flux imparts an electromotive force on the coils, causing a current to flow when a load is attached. A basic electromagnetic energy harvester design for a MEMS application is depicted in Figure 2.4.

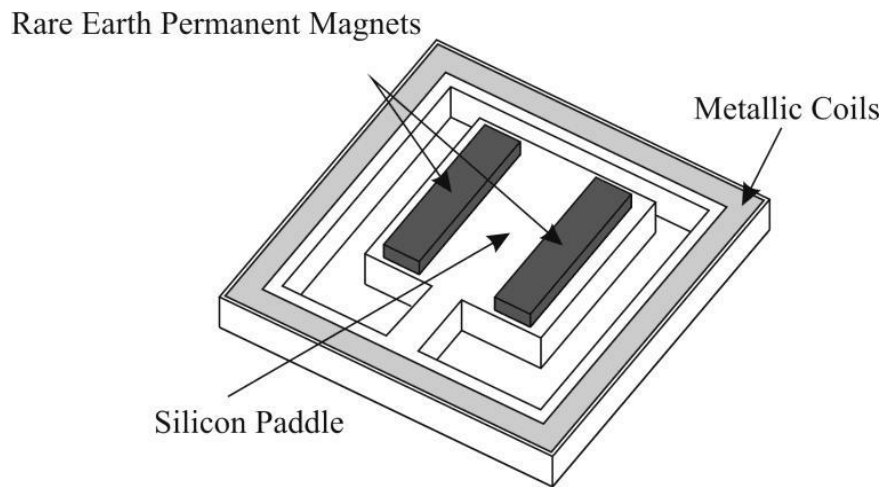


Figure 2.4. Schematic of an Electromagnetic Generator (Lueke & Moussa, 2011).

In these devices, the coils are generally stationary and the magnets are built to be excited by the vibrations applied to the device. This is because it is easiest to make reliable electrical connections with stationary objects. In addition, the permanent magnets utilized, often Neodymium Iron Boron (NdFeB), are very dense in relation to the coils. This makes them logical starting points for the proof mass. While the generator is capable

of harvesting in any direction, the design intent is usually limited to a single oscillation direction so as to maximize the harvester's potential for a given environment.

Electromagnetic generators constitute the majority of the electricity generators used today. These include devices as diverse and massive as power-grid driving turbines or alternators down to micro-scale generators found in “kinetic” watches or new bio-implantable devices found in literature. Of some interest are “shaker” flashlights that operate on a scale similar to those expected of a WSN energy harvester. Additionally, several commercial inertial harvesters have been brought to market relying on induction techniques. Notably, the Perpetuum Vibration Energy Harvester (VEH) is available with six off-the-shelf frequency models: 25 Hz, 30 Hz, 50 Hz, 60 Hz, 100 Hz, 120 Hz (Perpetuum). Figure 2.5 summarizes several commercially available electromagnetic generators.



Figure 2.5. Summary of common electromagnetic energy generators, including (a) Perpetuum VEH, (b) Guardian Shake Flashlight, (c) Seiko Kinetic Perpetual Watch, and (d) alternators in hydroelectric plant (Perpetuum; Survival Universe; Seiko (2014); Library of Congress (2014)).

Electromagnetic vibrational harvesters show several advantages over other inertial generators. As the technology is used so widely in consumer applications, it is more

mature and often easier to manufacture on the macro scale than either electrostatic or piezoelectric devices. Perhaps more importantly, inductive generators are preferred in low frequency applications (such as those seen in bridge oscillations) as the impedance of inductive systems is directly proportional to frequency (Dierks, 2011). In opposition to the other techniques, this translates to a relatively low voltage but high current outputs. For these reasons, electromagnetic inductive harvesters are the primary focus for this work.

2.3 SUMMARY OF RELEVANT LITERATURE

2.3.1 Overview of Electromagnetic Energy Harvester Literature

One of the earliest works that discusses the development of vibrational energy harvesting is a feasibility study performed by Williams & Yates (1996) at the University of Sheffield, U.K. The work serves as an excellent resource for the development of a basic analytical model for a simple generator. Treating the system as a second-order model, a simple derivation for the estimated power generated can be achieved. This serves as starting point for identifying critical components in any inertial energy harvester.

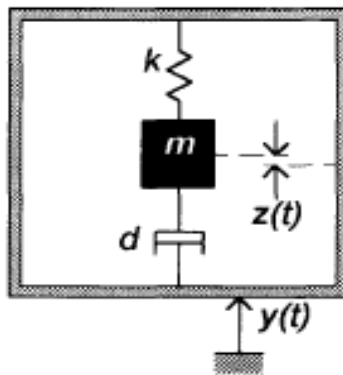


Figure 2.6. Schematic for a vibrational generator (Williams & Yates, 1996).

Here, the mass displacement relative to the generator housing is represented by $z(t)$ when the system is subject to some displacement, $y(t)$. The moving proof mass is represented by m , k is a spring constant, and d is the damping constant. In these devices, the creation of electricity damps the moving mass and should be the primary component of d . A good harvester design has an electrical damping coefficient at least one order of magnitude larger than the less desirable damping losses (Williams & Yates, 1996). From this, the basic second-order differential equation of motion can be obtained, as shown in Equation 2.1.

$$m\ddot{z}(t) + d\dot{z}(t) + kz(t) = -m\ddot{y}(t) \quad (2.1)$$

Then, knowing that the force on the mass is equal to the force on the mass-spring-damper ($F = -m\ddot{y}(t)$), an equation for instantaneous power can be derived as the product of force and velocity.

$$p(t) = -m\ddot{y}(t) * [\dot{y}(t) + \dot{z}(t)] \quad (2.2)$$

For a given sinusoidal excitation vibration, $y(t) = Y_0 \cos(\omega t)$, the net electrical power generated can then be found, as shown in Equation 2.3.

$$\text{Generated Power} = \frac{m\zeta Y_0^2 \left(\frac{\omega}{\omega_n}\right)^3 \omega^3}{\left[1 - \left(\frac{\omega}{\omega_n}\right)^2\right]^2 + \left[2\zeta \frac{\omega}{\omega_n}\right]^2} \quad (2.3)$$

Here, m is the moving mass, ζ is the damping factor, ω_n is the system's resonant frequency, Y_0 is the amplitude of vibration, and ω is the angular frequency of excitation.

Equation 2.3 provides insight into several key design aspects for vibrational energy harvesters. The first is that these devices are heavily dependent on available vibrational energy; higher frequencies and amplitudes of vibration produce greater power

outputs. This means that devices should be deployed in bridge locations with the greatest amount of vibrational energy based on these two factors. The second is that the maximum power output occurs when the device's natural frequency is matched with the frequency of vibration. Figure 2.7 illustrates this point by plotting average power against the frequency for various damping factors. It can be seen that larger damping factors create broader harvesting "bands" while smaller damping factors maximize power output in a smaller frequency range. This means it is desirable to reduce total damping for high peak power if the excitation is of a known frequency, but larger damping values are preferred if the frequency may shift. Last, increasing the proof mass is desired, within reason, based on the installation location constraints.

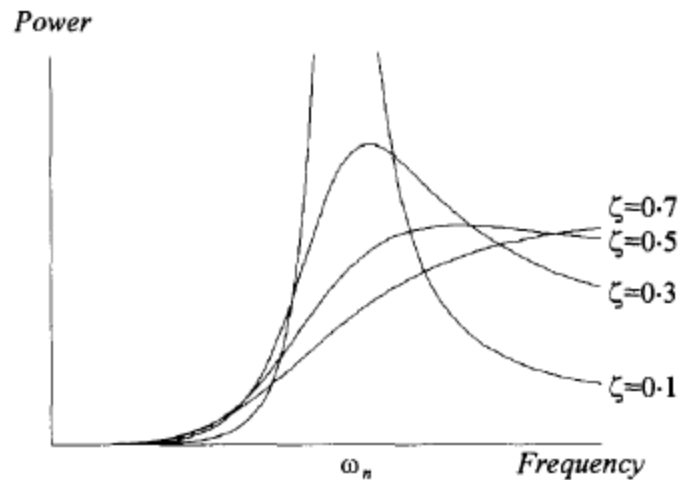


Figure 2.7. Plot of frequency spectrum of power generation around the resonance frequency of the generator for various damping factors (Williams & Yates, 1996).

Numerous works with a variety of energy production goals and desired deployment locations have been observed in literature. Many works focus on MEMS scale devices for such purposes as bioimplantability to power devices such as pacemakers. Patel & Khamesee (2013) provide a comparison of several prominent

vibrational harvesters found in the literature, shown in Table 4. As is evident, the harvesters have a variety of dimensions and power capabilities. Of note, most harvesters tend to focus on frequencies in the tens or hundreds of Hz. A specific challenge to efficiently harvesting ambient energy from bridge vibrations is that the available frequencies tend to be lower than any comparable devices found in literature currently.

Table 2.1. Compilation of Available Harvesters Power Outputs and Power Densities (Patel & Khamesee, 2013).

References	Volume (cm ³)	Frequency (Hz)	Amplitude (m/s ²)	Power (W)	Power density (W/cm ³)
Glynne-Jones et al. (2000)	0.84	322	2.7	1.80E-04	2.14E-04
Williams et al. (2001)	0.0054	4,400	382	3.00E-07	5.56E-05
Ching et al. (2002)	1	110	95.5	8.30E-04	8.30E-04
Beeby et al. (2007)	0.15	52	0.589	4.60E-05	3.07E-04
Wang et al. (2009)	3.15	280	10	1.72E-05	5.46E-06
Domme (2008)	112	16	3.74	5.50E-03	4.91E-05
Saha et al. (2008)	12.5	8	0.38	1.50E-03	1.20E-04
Hoffmann et al. (2009)	0.68	390	88.29	5.00E-06	7.35E-06
Hadas et al. (2010)	100.9	17	4.9	5.00E-03	4.96E-05

2.3.2 Literature Review of Low Frequency Specific Applications

Current literature features a number of electromagnetic harvesters operating at a variety of frequencies. While this is expected given the large number of potential applications, many sources simply use an arbitrary excitation frequency for numerical or experimental testing. As generator power is dependent upon the cube of this frequency, it seems that development of a harvester for the particularly low frequencies found in bridge spans must focus on this limitation. Two particular types of low frequency applications are found in the literature. First, a series of harvesters was developed at Clarkson University to power wireless sensors in an effort similar to the project goals laid out here. The second major application is derived from research focused on developing EM harvesters for body-worn applications. Most of these studies target resonant

frequencies less than 10 Hz. As these are the closest examples of devices designed near bridge excitations, they are presented here.

Beginning in 2007, a team from Clarkson University in New York began investigating the potential to power wireless sensors using traffic induced vibrations from a bridge span. Li and Pillay published works detailing two specific harvester iterations. In Li & Pillay (2007), the schematic shown in Figure 2.8 (a) was proposed as a feasibility study of the applicability of EM harvesting techniques on bridge structures. While specific reasoning for the topology of the design was not provided, the system is a basic mass-spring-damper second order type. In this case, a linear spring provides the movement energy storage. A pair of magnets is used with an ironless “mover” attachment mechanism that oscillates when excited by the bridge vibrations. A static central coil (stator) is then utilized and mounted to the device housing, which is directly attached to the bridge structure. A second design was developed by the same team in Li & Pillay (2011) and depicted schematically in Figure 2.8 (b) and in embodiment in Figure 2.8 (c). This revised design utilized a tubular, axisymmetric design with three circular permanent magnets and three associated coils. These magnets were placed with opposing poles facing and iron disks between them. This has the effect of concentrating the magnetic field over the coils and minimizing flux leakage. In comparison to the initial design, the second design requires a lower overall volume and increases the flux in the coil. This design also maintained the three coils as separate entities, effectively creating a three-phase voltage in hopes of boosting circuitry efficiency.

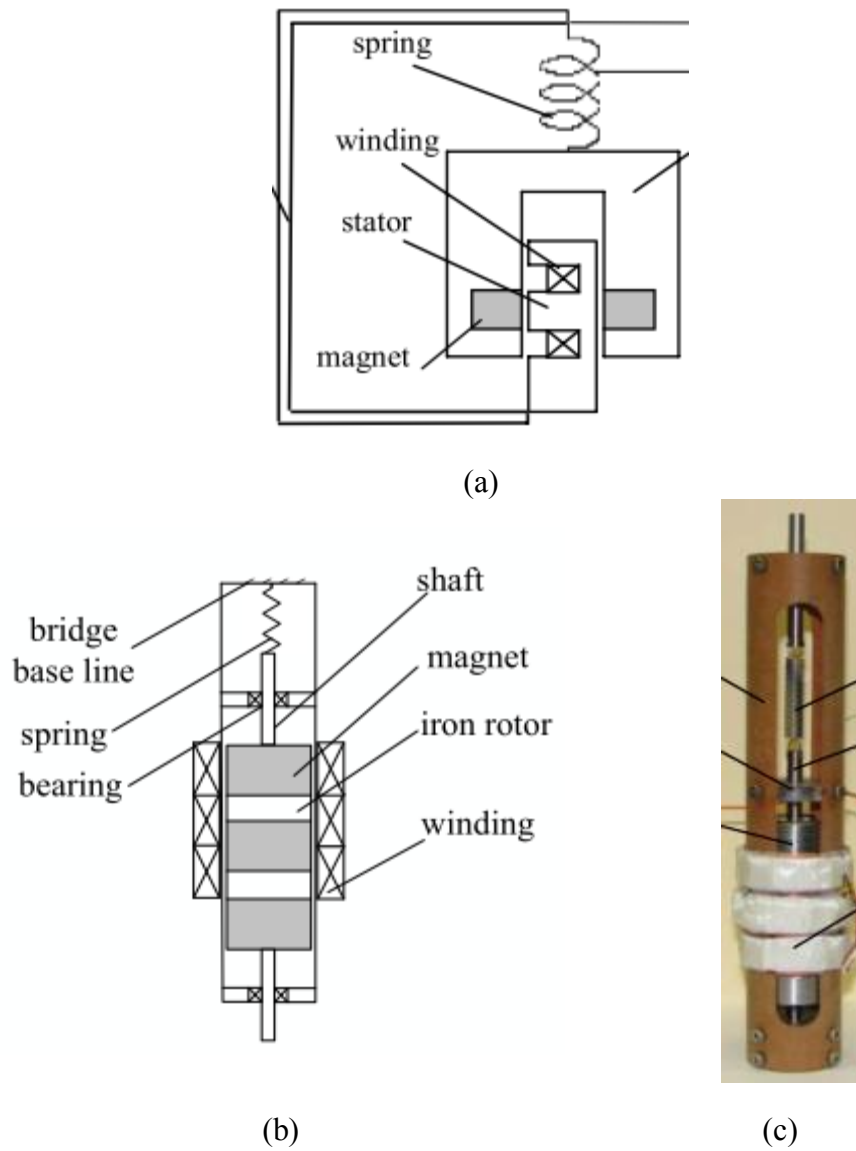


Figure 2.8. Bridge-specific energy harvester concepts from Clarkson University - (a) (Li & Pillay, 2007), (b&c) (Li & Pillay, 2011).

Three body-motion driven harvester designs were also located in literature, Saha, O'Donnell, Wang, & McCloskey (2008), Patel & Khamesee (2013), and von Buren & Troster (2007). Body-motion excitations share many characteristics with bridge excitations, such as low frequencies and non-sinusoidal waveforms, making them

promising references for bridge work comparison. All three examples focus on similar geometries: a tubular, axisymmetric harvester with a permanent magnet “mover” and copper coil stators. They also focus on similar volumes, with overall sizes approximating that of an AA battery so as to be feasible in a body-worn application.

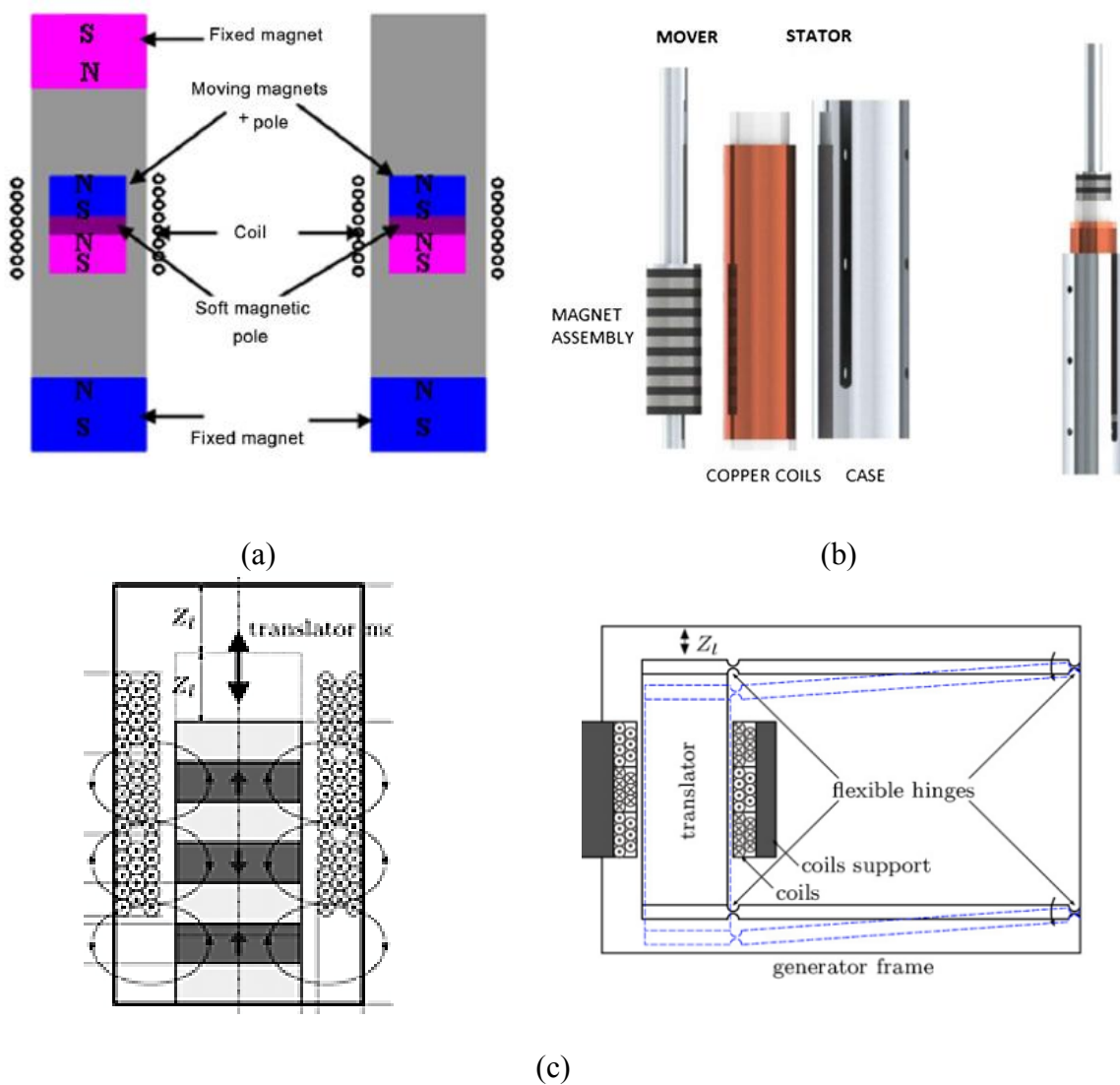


Figure 2.9. Assorted body-worn EM harvesters – (a) (Saha, O'Donnell, Wang, & McCloskey, 2008), (b) (Patel & Khamesee, 2013), (c) (von Buren & Troster, 2007)

Saha et al. developed a simple harvester relying on only a single coil and magnet pair (Figure 2.9 (a)). One interesting design choice was the replacement of the traditional linear spring with a magnet pair positioned with poles opposing the translator. This has the advantage of reducing the overall size, as magnetic springs require less translational distance than corresponding helical springs. This topology is similar to that found in many “shaker” flashlights, with the noted difference that the normal single axially magnetized translator is replaced with two opposing magnets and a central iron pole (similar to Li & Pillay (2011)). Using finite element analysis (FEA) they showed that the flux density using this topology provides nearly a two-fold increase in the coil compared to the single magnet design. Patel & Khamesee (2013) developed a generator (Figure 2.9 (b)) very similar to that described by Li & Pillay (2011). The only notable change was an increase in the number of magnets in the mover assembly. This device tested favorably with a power density near the best harvesters previously seen.

One of the most detailed design methodologies was presented by von Buren & Troster (2007). While the proposed harvester demonstrates an architecture similar to those previously discussed (a tubular, axisymmetric design with opposing axial magnets and soft magnetic poles depicted in Figure 2.9 (c)), particular attention was paid to optimizing the geometries of the device. A methodology was proposed to independently determine the optimal stator and translator geometry using FEA and an analytical model with the simulated annealing algorithm (as they do not inherently depend on the available excitation frequencies) first; then, the spring and load were optimized based on the desired installation location (Figure 2.10).

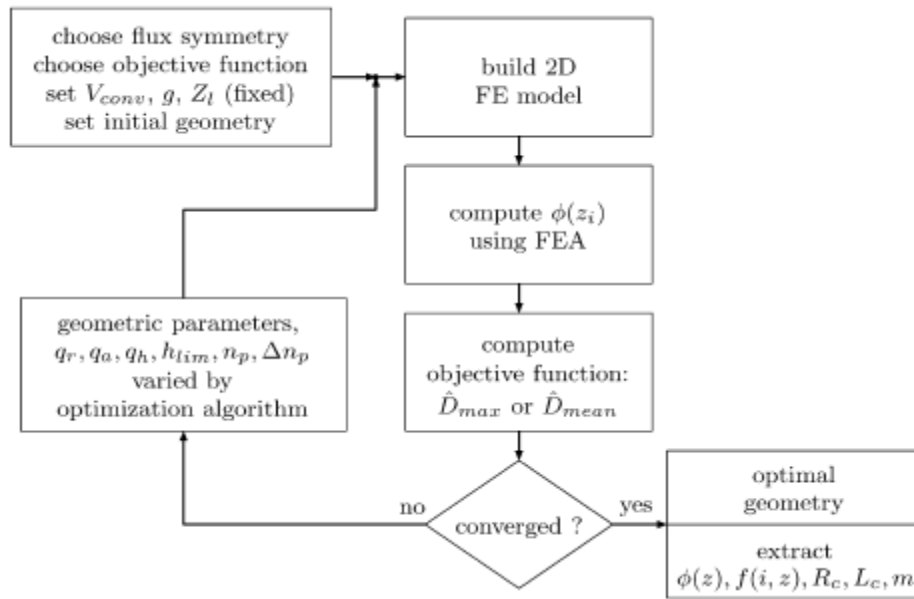


Figure 2.10. Flowchart for geometry optimization (von Buren & Troster, 2007).

An important takeaway from the results is that the optimal geometry of the stator and translator are presented as ratios of lengths. This means the geometry can be scaled to fit a particular deployment location and power requirement combination. Tables 5 and 6 present their findings. Several designs were evaluated (Table 6) using these methods with variations in the number of magnets, coil turns, etc. and a final design was chosen and prototyped for validation using low frequency, non-sinusoidal excitations found in body-motion. The device also featured a unique four-bar mechanism with living hinges as the compliant member. This was justified by fewer moving parts for longevity but limits the available displacement of the translator.

Table 2.2. Optimization Parameters for Stator and Translator from (von Buren & Troster, 2007).

Parameter	Description	Values
Fixed		
V_{conv}	Combined volume of stator and translator	0.25 cm ³
g	Air-gap length	0.15 mm
Z_1	Maximum translator displacement	2 mm
Variable		
$q_r = R_m/R_o$	Ratio of magnet radius to outer radius	[0.05, 0.95]
$q_h = h_m/h_p$	Ratio of magnet height to pole pitch	[0.05, 0.95]
$q_a = h_{conv}/R_o$	Aspect ratio: total height to outer radius	[2.95, 10.03]
h_{lim}	Height-limitation	('translator-limited' or 'coil-limited')
n_p	Number of poles on length-limiting part	[1, 25]
Δn_p	Difference in pole numbers between parts	[-5, 5]

Table 2.3. Optimal Geometries for Four Evaluated Designs from (von Buren & Troster, 2007).

Objective function	\hat{D}_{max}		\hat{D}_{mean}	
	Odd Design A	Even Design B	Odd Design C	Even Design D
Flux symmetry				
$q_{r,Opt}$	0.74	0.74	0.75	0.73
$q_{h,Opt}$	0.84	0.84	0.83	0.86
$q_{a,Opt}$	10.00	9.97	10.02	9.35
h_{tr} limited by	Translator	Translator	Translator	Translator
$n_{m,Opt}$	8	8	9	6
Δn_p	1	0	1	0
\hat{D}_{max} (N s/m)	0.32	0.31	0.30	0.30
\hat{D}_{mean} (N s/m)	0.16	0.17	0.17	0.20
n_c	9	8	10	6
h_m (mm)	1.64	1.64	1.44	2.11
h_p (mm)	1.95	1.95	1.74	2.46
R_o (mm)	2.00	2.00	2.00	2.04
t_c (mm)	0.37	0.37	0.37	0.40
h_{tr} (mm)	16.0	16.0	16.0	15.1
h_{conv} (mm)	20.0	20.0	20.0	19.1
d_w (μ m)	25	25	24	27
n_{tot}	12087	10608	12580	9384
R_c (k Ω)	4.83	4.15	5.57	3.28
m (g)	0.82	0.82	0.84	0.79

Based on these reviews, it seems the tubular, axisymmetric harvester topology proves the most popular for low frequency applications. This topology presents minimal flux leakage with a simple design that eases fabrication. In addition, the usage of soft magnetic poles between opposing axially magnetized permanent magnets shows

considerably higher flux densities than axial magnets alone and is worthy of further investigation. The spring design should also be considered, as numerous devices are seen in literature: helical, magnetic, cantilever beams, and a four-bar mechanism with living hinges.

2.4 REVIEW OF *EVALUATING VEHICULAR-INDUCED VIBRATIONS OF TYPICAL HIGHWAY BRIDGES FOR ENERGY HARVESTING APPLICATIONS*

As part of the NIST-TIP team project, a study was undertaken by Reichenbach (2012) to determine the feasibility of powering an electromagnetic energy harvester by measuring the dynamic responses of five representative bridges using accelerometers. This work serves to highlight the challenges encountered when exploring bridges of varying superstructures, age, traffic patterns, and more. In addition, it provides some background on design choices when selecting a harvester design.

2.4.1 Field Instrumentation and Data Acquisition

In order to understand the response characteristics of assorted bridges, five steel bridges in Texas and Oregon were outfitted with accelerometers at varying locations. The most exhaustive survey was of the I-35N Bridge over the Medina River in San Antonio, TX. This bridge is particularly interesting as it has undergone several retrofits to serve traffic capacities beyond its original intended design as well as to extend its original service life. It is also the oldest bridge surveyed by several decades and represents an optimal choice for a wireless health monitoring system. The three middle spans are pictured in Figure 2.11.



Figure 2.11. Image of I-35N Bridge over Medina River (Reichenbach, 2012).

For this bridge, acceleration data was acquired over five separate months in 2010-2011 at 28 different locations. Compared to the other bridges studied, this was the most robust data acquisition effort as it evaluated more locations and accounted for greater temperature effects than any other. Each data capture point was measured continually for at least one week. The bridge has several different components that were studied for instrumentation, pictured in Figure 2.12. The longitudinal girders, floor beams, and lateral braces were all studied with accelerometer measurements at various locations. While the effects of an attached energy harvester could be ignored on the girders and floor beams, the lateral braces were studied with an attached 13 lb mass as they are considerably slimmer. As a fully developed energy harvester may weigh more than 10 lbs, this added mass allowed the team to study the effects the harvester might have on the available vibrations.

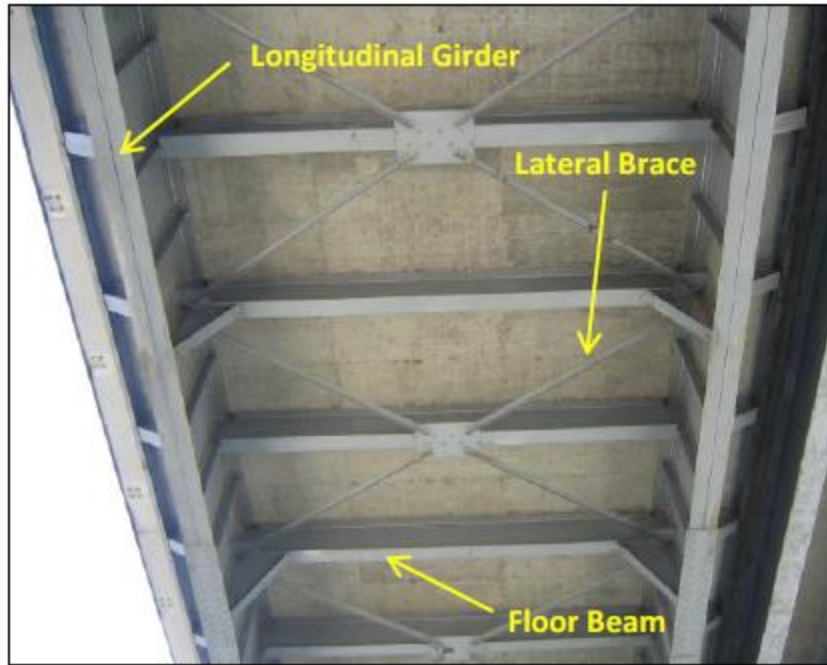


Figure 2.12. Under-view of Medina River Bridge with key components highlighted (Reichenbach, 2012).

While the Medina River Bridge was the most extensively tested, four more bridges were examined: the TX-71E Bridge over US-183 in Austin, TX, the I-35N to US-290E Direct Connector in Austin, TX, the I-205W to I-5S Interchange Bridge in Tualatin, OR, and the I-5 Bridge over the Columbia River in Portland, OR. The acceleration data for all the bridges was sampled at 50 Hz continuously. Since bridges tend to have dominant oscillations at very low frequencies, this was deemed adequate for the desired analysis. As the Nyquist frequency is half the available sampling rate, frequency domain analysis could be performed for a range of 0-25 Hz. Additionally, the data was band-pass filtered between 0.5 Hz and 24 Hz to remove noise found at the extremes of the frequency range.

2.4.2 Spectral Analysis and Initial Findings

Before spectral analysis was performed, a time-domain analysis using the root mean square (RMS) was examined. This resulted in several notable conclusions. Higher RMS values generally indicate larger peak acceleration amplitudes. This is important as larger acceleration amplitudes can be linked to greater generator output. By comparing this with traffic patterns, it was found that bridges with larger RMS values usually correlated with greater large truck traffic. From this, it was determined that spans experiencing greater truck traffic are more likely to contain more vibrational energy than those serving mostly small vehicular traffic. It was also found that traffic volume associated with the busiest roadway hours (rush hour) has a direct effect on the power potential.

Frequency domain analysis was performed by creating power spectral density (PSD) plots using Fourier transforms. Figure 2.13 presents PSD results from samples of data from three bridges: (a) the Medina River Bridge, (b) US-290 Bridge, and (c) TX-71E Bridge. These PSD plots effectively present the dominant modes for a particular accelerometer location. This information is important in the design of a potential harvester, as it should be tuned to the resonance at the desired deployment location. These samples showcase the huge variability seen during the instrumentation of the bridges. The Medina River sample provides a very wideband location, the US-290 shows two distinct modes that could be designed for, and the TX-71E location shows very little oscillation at all.

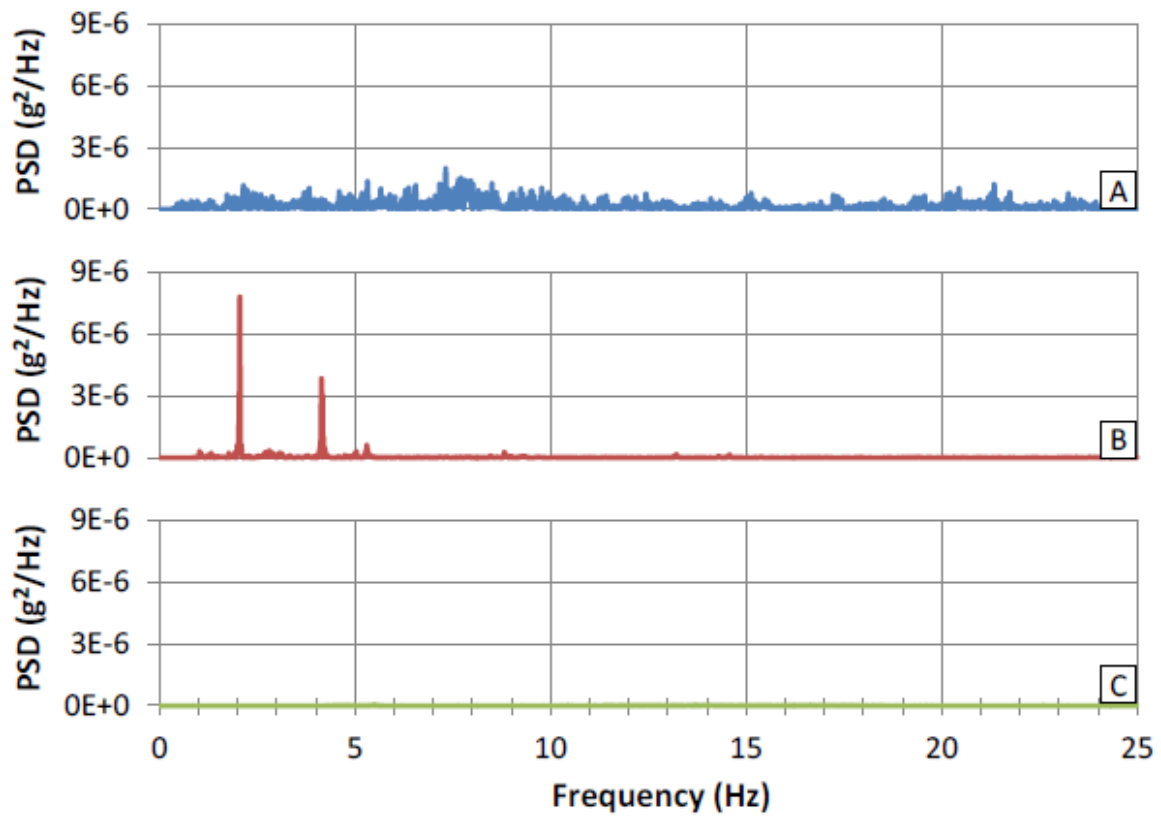


Figure 2.13. Comparison of three sample PSD outputs: (A) Medina River Bridge, (B) US-290 Bridge, and (C) TX-71E Bridge (Reichenbach, 2012).

By examining the gathered data, several challenges were observed with identifying the proper frequencies for an energy harvesting device. In addition to huge discrepancies in bridge frequencies based on geometry and deployment location, it was found that a particular location on a single bridge can also vary. This can be due to several affects. As a bridge ages, it tends to accumulate damage, which can alter the stiffness. The findings show these changes in stiffness can cause the dominant modes to drift slightly over time; however, substantial shifts are unlikely (Reichenbach, 2012). Additionally, traffic patterns can determine which mode is activated at a particular time. In general, smaller vehicles tend to activate higher frequency modes, while larger trucks

activate low frequency modes. This can become even more challenging when analyzing the effects of multiple vehicles crossing simultaneously.

Similarly, natural temperature fluctuations over the course of a year alter the relative stiffness of the bridge. Figure 2.14 demonstrates the effects of temperature on the second modal frequency of a span of the TX-71E Bridge. While these fluctuations are relatively small, they represent only a single potential deployment location. As such, some spans might see a larger change, especially as temperature fluctuations can be quite dramatic over the course of an entire year. In addition, as bridge damage accumulates over time, these natural fluctuations can be exaggerated which may drive the resonant frequency farther from the originally tuned value of a generator. This all indicates that great care must be taken to thoroughly evaluate the dominant modes of any potential deployment locations as changes in desired frequency can have considerable detrimental effects on harvester efficiency. Therefore, it may be determined that more “broadband” harvesters will be required in some situations.

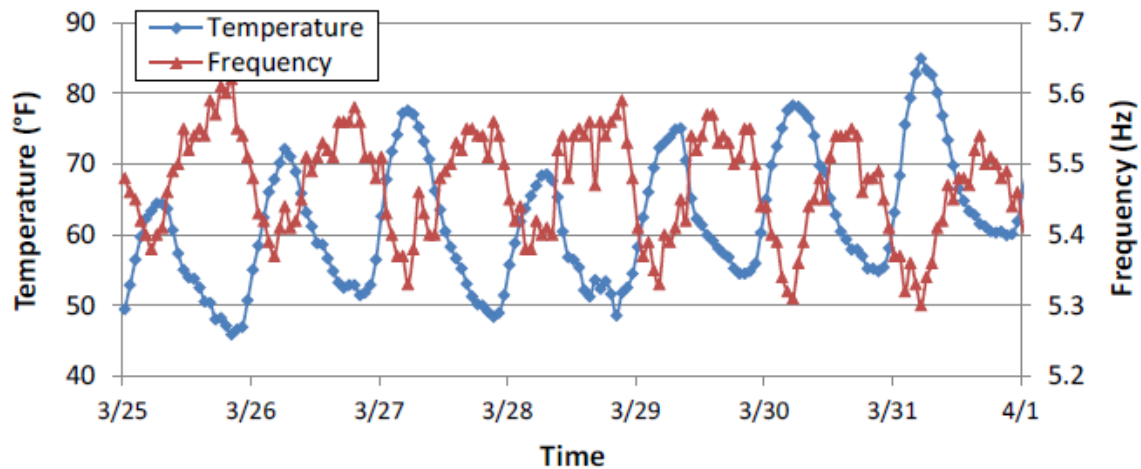


Figure 2.14. Second modal frequency and temperature tracked as a function of time for TX-71E Bridge (Reichenbach, 2012).

2.4.3 Potential Power Availability

By developing a numerical model for potential harvester outputs, the samples of acceleration data can be utilized to provide theoretical power response spectrums. It should be noted that for such a model, several key harvester parameters were estimated from early work by Dierks (2011) to provide a baseline. Using this methodology, several key aspects of a harvester were explored. First, an analysis of the average power (normalized per kg of oscillating mass) versus frequency for varying damping ratios was explored (Figure 2.15).

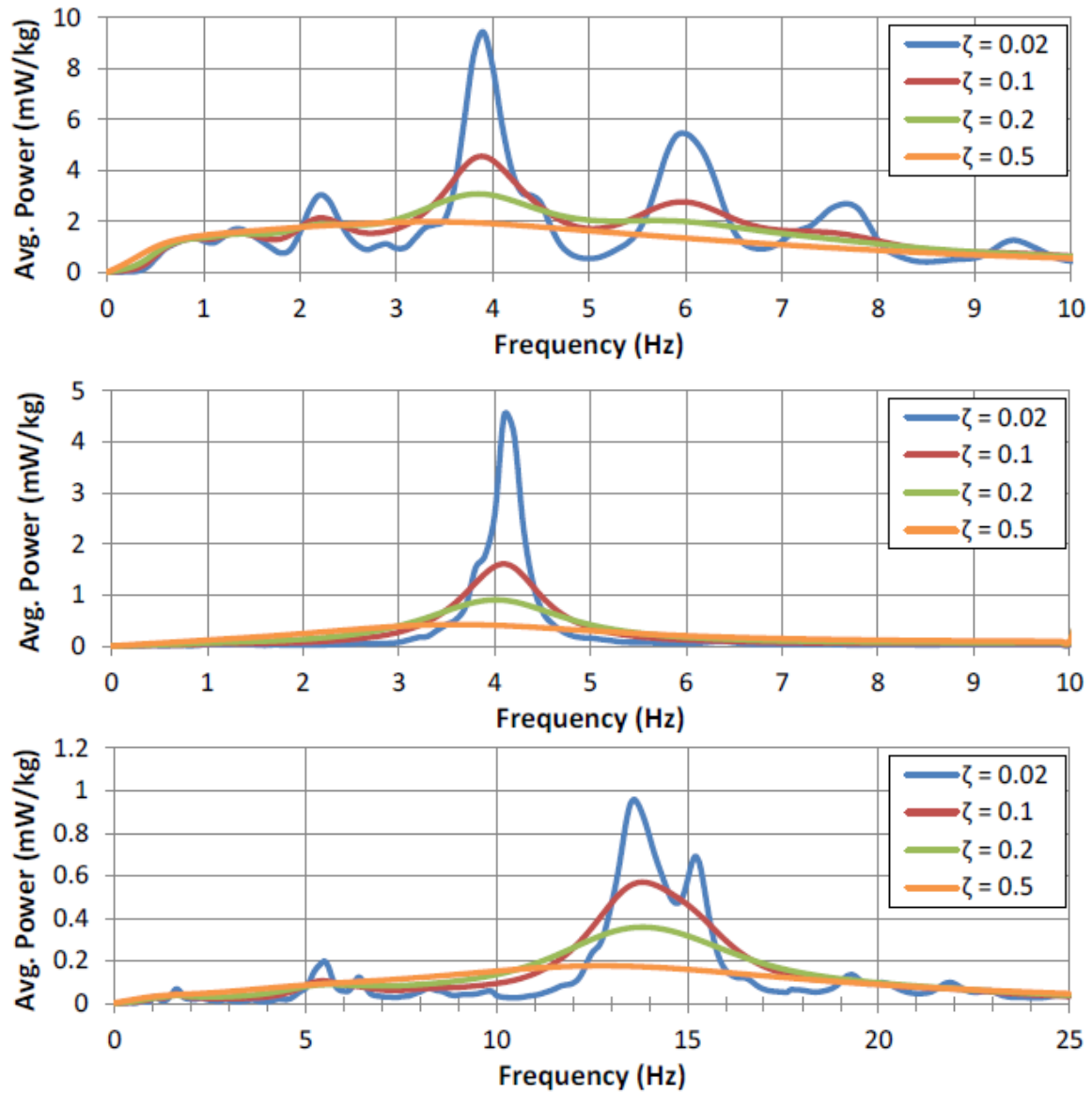


Figure 2.15. Response spectrum for sample acceleration history for Medina River Bridge (top), US-290 Bridge (middle), and TX-71E Bridge (bottom) (Reichenbach, 2012).

Several important results can be inferred from this analysis. First, the Medina River Bridge sample provides considerably more average power than the other two samples overall. This holds true for most data locations instrumented, making the Medina

River Bridge the best candidate for powering a vibrational energy harvester. In addition, the designed damping ratio has an obvious and significant impact on the overall power generated, as expected. A design decision must be made for an optimal damping ratio to enable maximum power generation over the lifetime of a harvester, with consideration of the variability of bridge frequencies over time. Based on these graphs, it seems a damping ratio of approximately 0.1 provides a reasonably large bandwidth without reducing total power output too drastically. While some bridges might have adequately narrow frequencies for lower damping ratios, physical limitations in minimizing mechanical damping must be considered as they are incorporated in total damping.

In order to estimate long term feasibility, full-week power response spectra were calculated using optimal mount location datasets for each bridge. Figure 2.16 compares the results. Based on these indications, it seems the US-290 Bridge, the Columbia River Bridge, and SH-71E Bridge are unsuitable for vibrational energy harvesting. Original project goals set out to provide a minimum of 0.5 mW average power (enough to power a single wireless node). Without unrealistically large masses, adequate power generation is not currently feasible. The I-5/I-205 Bridge shows more promise, albeit in a fairly narrow frequency band. As these plots utilized the 0.1 damping ratio, a slightly larger bandwidth might be implemented (at the cost of maximum power generation) to help reduce the efficiency losses incurred during the expected frequency variations. Provided an adequate mass could be utilized, the 0.5 mW goal seems attainable. Even more promising is the Medina River Bridge. This bridge demonstrates a large bandwidth and it seems a harvester tuned to any frequency from approximately 1 to 12 Hz can be sized to provide adequate power.

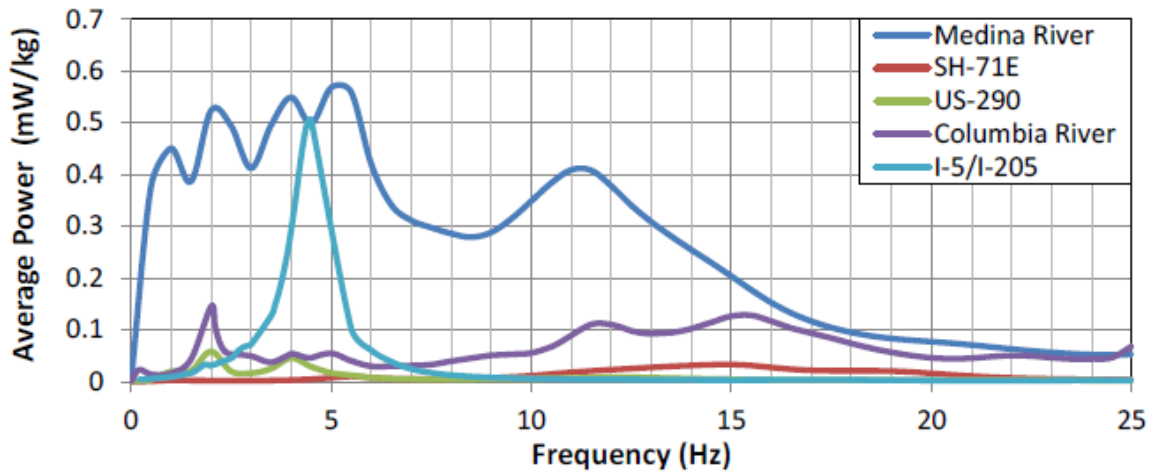


Figure 2.16. Average weekly power response spectra for the five instrumented highway bridges (Reichenbach, 2012).

To further explore these results, the average power output from the Medina River Bridge span was again analyzed with the 1.454 kg mass suggested by Dierks (2011). Figure 2.17 demonstrates that a harvester using this mass and tuned from 1 to 6 Hz should provide adequate power generation. This is promising going forward, suggesting that at least some bridge spans will be capable of the power goals proposed for this project.

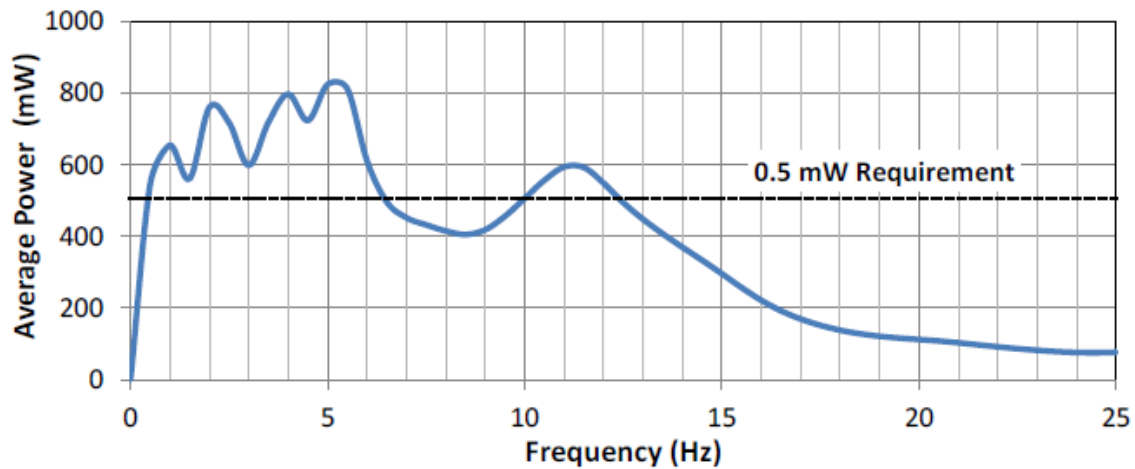


Figure 2.17. Average weekly power response spectrum for Medina River Bridge with 1.454 kg mass (Reichenbach, 2012).

2.4.4 Conclusions

These results outlined from the work by Reichenbach provide considerable insight into the potential viability of a vibrational energy harvester for powering a bridge WSN system. Overall, each bridge must be examined individually as large discrepancies in power potential exist between the various bridge geometries and some bridges will prove unsuitable for reasonable energy harvesting. Further, a spectrum of deployment locations on a particular bridge should be investigated to locate optimal deployment locations with maximum energy density. Spectral analysis of dynamic response data captured using accelerometers can be performed to locate dominant frequencies that can then be used to drive harvester design. Additional care should be taken to design a generator with adequate bandwidth such that natural variations in bridge frequency associated with aging and temperature fluctuations do not render the system underpowered. Simulations performed by Reichenbach indicate that powering a 0.5 mW WSN node with an EM harvester is feasible for at least some bridge spans, with the Medina River Bridge seemingly an ideal candidate.

2.5 REVIEW OF *DESIGN OF AN ELECTROMAGNETIC VIBRATION ENERGY HARVESTER FOR STRUCTURAL HEALTH MONITORING OF BRIDGES EMPLOYING WIRELESS SENSOR NETWORK*

The work by Dierks (2011) constitutes the first effort by the NIST-TIP team to produce a viable electromagnetic vibrational energy harvester to power a WSN node using bridge oscillations. Throughout this work, several key questions were investigated to provide solutions to the challenges found in a bridge application. In addition to the overall performance of the harvester, special care was taken to compare the efficiency of linear versus non-linear spring elements and to address the challenges of mounting a completed design to the highly variable bridge structures. This work was divided into three major segments: (1) the creation of a numerical model to investigate and verify model parameters, (2) an alpha prototype to experimentally validate power generation capabilities, and (3) a beta prototype focused on deployment mounting solutions and simplifying the manufacturing process. A brief overview of this work is presented here, while the entirety can be examined in the original literature (Dierks, 2011).

2.5.1 Numerical Model Development

In order to predict the performance of a particular harvester configuration and explore the key variables, a numerical model was first developed. This allowed a number of parameters to be explored and optimized for a given configuration, including the simulated excitation signal, linear and nonlinear spring elements, mechanical and electrical damping elements, and the geometric properties of a harvester. Given the prevalence of the tubular, axisymmetric design in literature, this was chosen for the basic geometry.

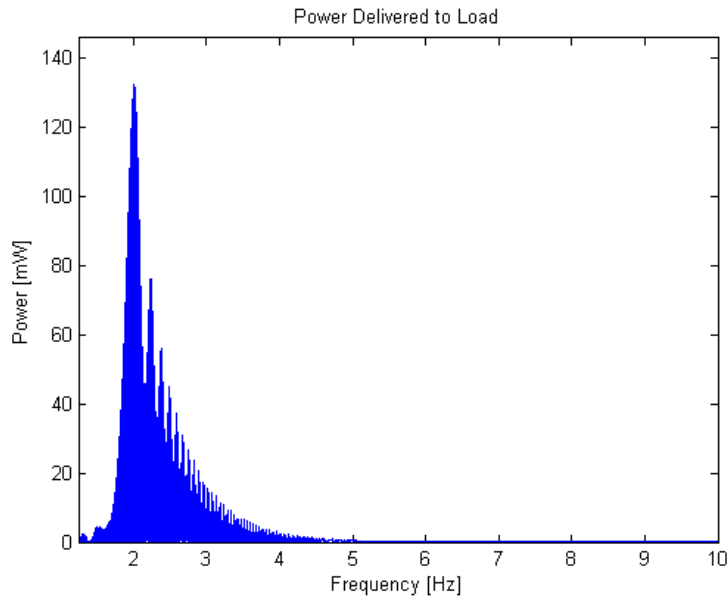


Figure 2.18. Peak power under increasing swept sine wave over 120 seconds at 0.05 g amplitude and 2.9 k Ω load (Dierks, 2011).

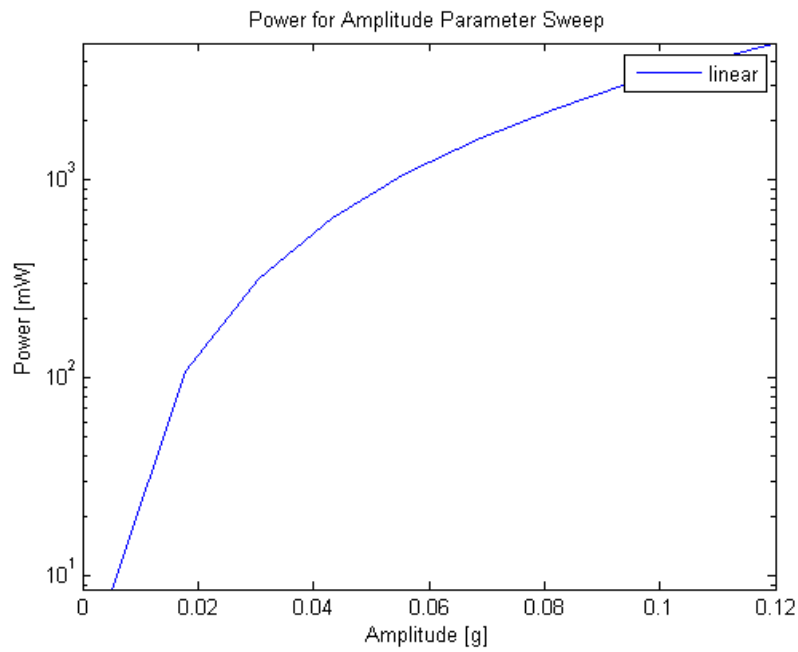


Figure 2.19. Peak harvested power for amplitude sweep under sinusoidal excitation at 2.2 Hz and 2.9 k Ω load (Dierks, 2011).

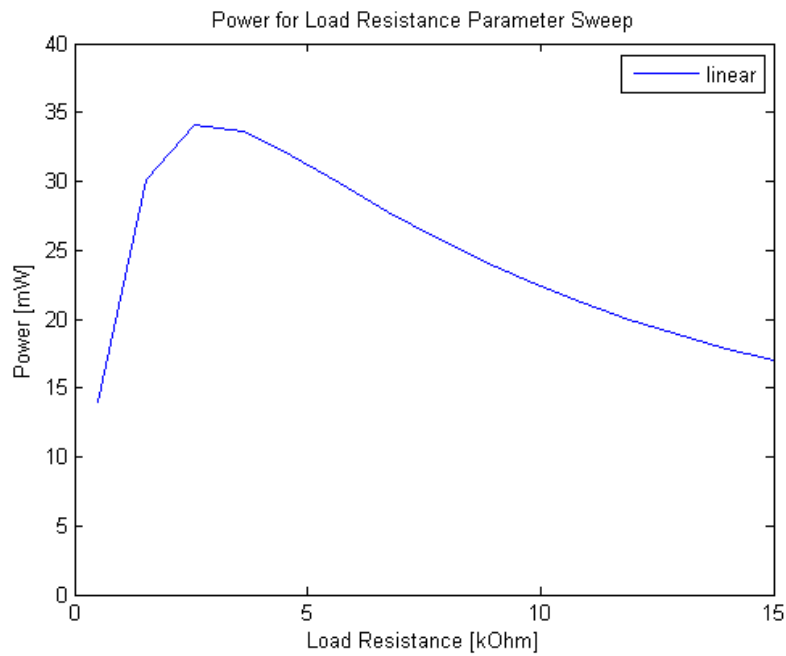


Figure 2.20. Peak harvested power for load resistance sweep under sinusoidal excitation at 2.2 Hz and 0.01 g amplitude (Dierks, 2011).

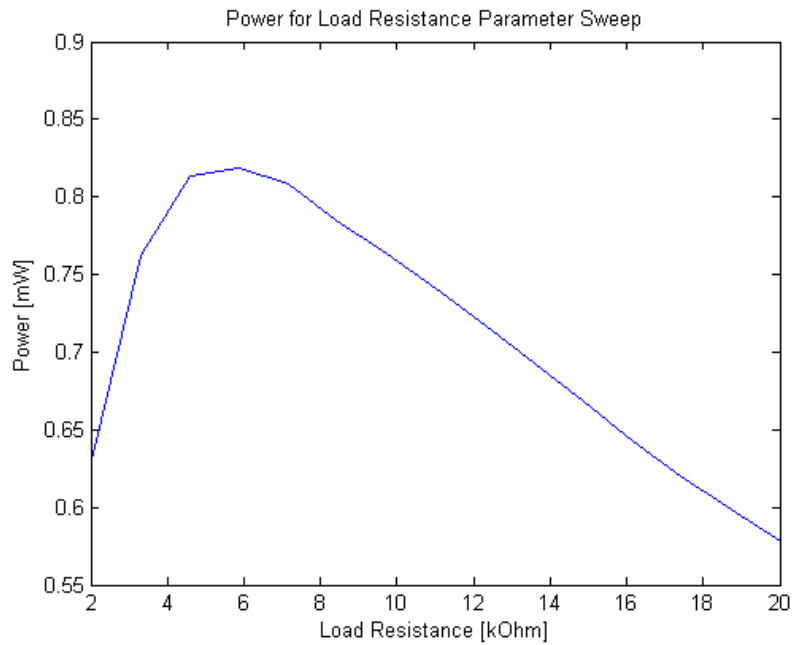


Figure 2.21. Peak harvested power for load resistance sweep under 50 seconds of IH-35N-US-290E direct connector acceleration data (Dierks, 2011).

By assuming initial geometric properties based on realistic final values, generator power outputs were measured using the developed numerical model. From this, several key tunable parameters were explored. First, the response was examined for a harvester tuned to approximately 2 Hz over a sinusoidal frequency sweep. Figure 2.18 shows results consistent with the expected analytical equations, as the maximum power is generated at the resonant frequency of the harvester. It is interesting to note that the power output decays more slowly above the resonant frequency of the harvester than below. Given the natural tendency for bridge vibrations to change with time (as discussed previously), this should be considered when deploying a device. If a particular bridge span tends to decrease in frequency with age, it might be prudent to design a device to resonate at the slightly lower frequency anticipated in the future.

Figure 2.19 highlights the large effect the acceleration amplitude has on the power generation potential. A single order of magnitude increase in oscillation amplitude (0.01 to 0.1 g) results in two orders of magnitude increase in peak power output. This further reinforces the need to fully evaluate a potential bridge location for sufficient amplitudes. Figures 2.20 and 2.21 illustrate how a change in the load impedance varies the power output of the generator. Figure 2.21 provides a sample of power generation using accelerometer data from a potential bridge source. Using spectral analysis, its dominant frequencies were shown to be near 2 Hz. Comparing Figure 2.20 to Figure 2.21 indicates that the optimal load is likely to change with individual location acceleration characteristics, even though both sources had very similar dominant frequencies. Based on these results, a final harvester device should include circuitry to dynamically change the load for optimal efficiency. Similar devices are routinely employed in high-power solar energy harvesting systems in the form of maximum power point tracking (MPPT),

and newer research such as Lopez-Lapena, Penella, & Gasulla (2010) has presented techniques that can increase the efficiency to be viable for low-power applications.

Further evaluation resulted from plotting the power output over a longer 300 second set of accelerometer data from the 35N-290E direct connector bridge. Figure 2.22 provides a corresponding view of the bridge acceleration data, the relative calculated displacement between the oscillating mass and bridge, the instantaneous power output, and total energy harvested. Analyzing the accelerometer response, the individual traffic events are obvious. The largest amplitudes are indicative of large trucks, while the smaller events are likely small vehicle traffic. Based on this, it is clear that the instantaneous power generation is orders of magnitude larger during the large truck events.

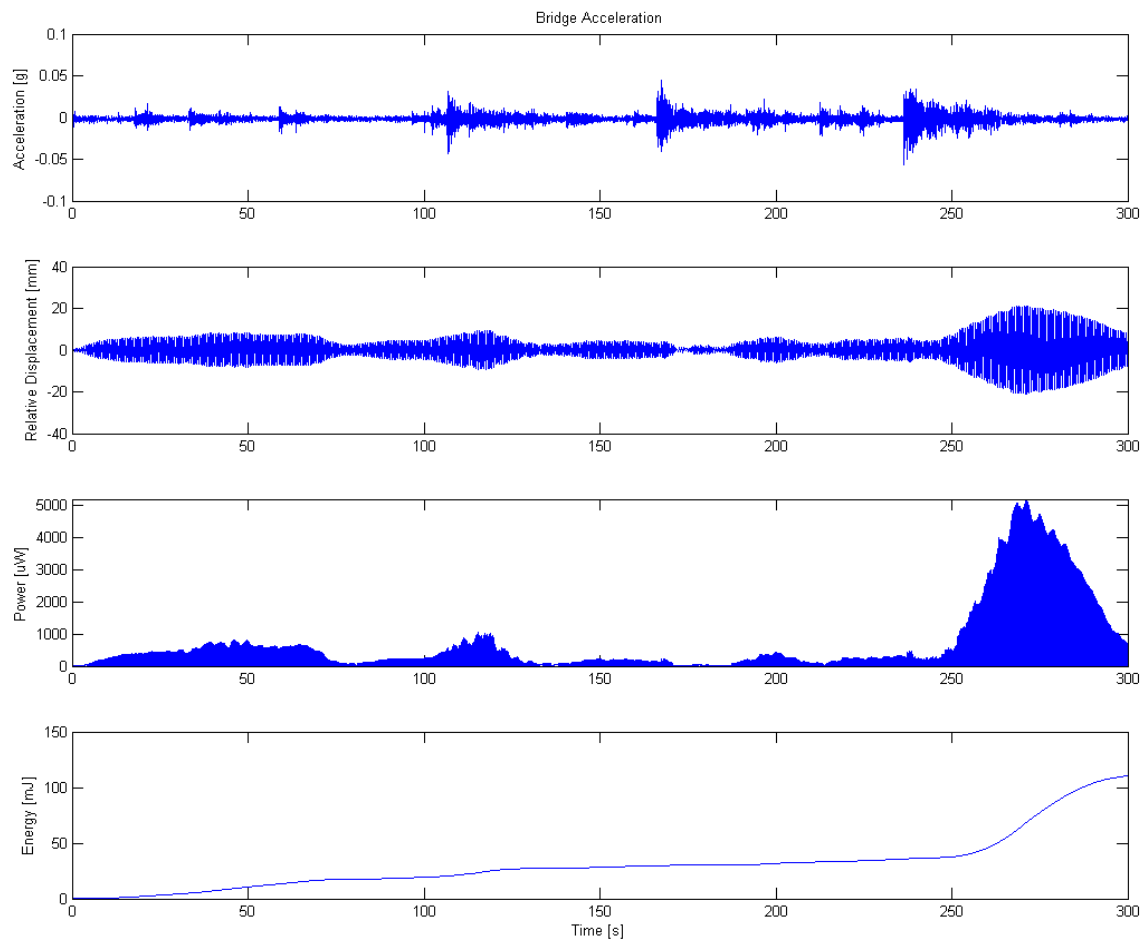


Figure 2.22. Bridge acceleration, relative displacement, peak harvested power, and harvested energy for 300 second of IH-35N-US-290E direct connector acceleration (Dierks, 2011).

One of the key concepts explored by Dierks was the use of non-linear springs in the form of a magnet pair positioned above and below the oscillating magnet mass, similar to the work by Saha, O'Donnell, Wang, & McCloskey (2008). By placing these magnets with poles opposing the axially magnetized mass, they act as the spring element in the system. When compared to standard helical extension springs, these require far less overall volume, reducing the total harvester size. After tuning for optimal separation

distance between the fixed magnets and mass, the power response from Figure 2.22 was repeated for the non-linear case, as shown in Figure 2.23.

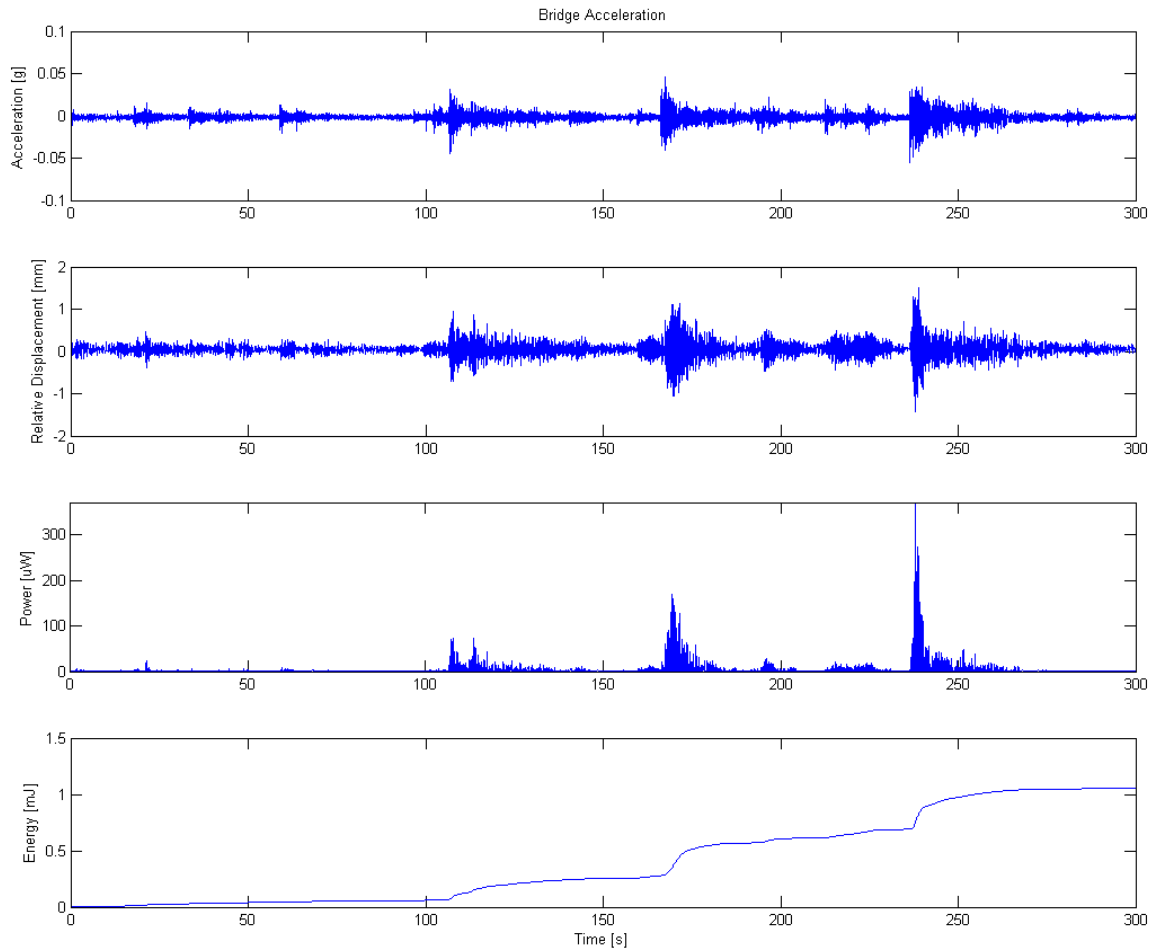


Figure 2.23. Non-linear spring case for energy harvested for 300 seconds of IH-35N-US-290E direct connector (Dierks, 2011).

Compared to the non-linear case, the linear harvester outperformed the non-linear version by a factor of 100 for the same set of acceleration data. Literature comparing these two cases often finds greater output from the non-linear generator. The reason for the discrepancy is because the bridge vibrations are fairly random and intermittent, and the nonlinear harvester excels with consistent excitation (Dierks, 2011). Therefore, it was

concluded that the linear case should be the focus for bridge-based vibrational energy harvesters.

2.5.2 Physical Embodiment and Experimental Validation

A beta prototype was next produced to experimentally validate the numerical model. The solid model is illustrated in Figure 2.24. As shown, this model uses the expected tubular design. It also allows for the use of either an extension spring or spring magnets to verify the results of the linear versus non-linear spring element. It should be noted that nearly all components were created using non-magnetic materials. Using 316 stainless steel for the parts that required metals reduces the interactions with the magnets that could guide the magnetic field away from the coils, thereby reducing power output.

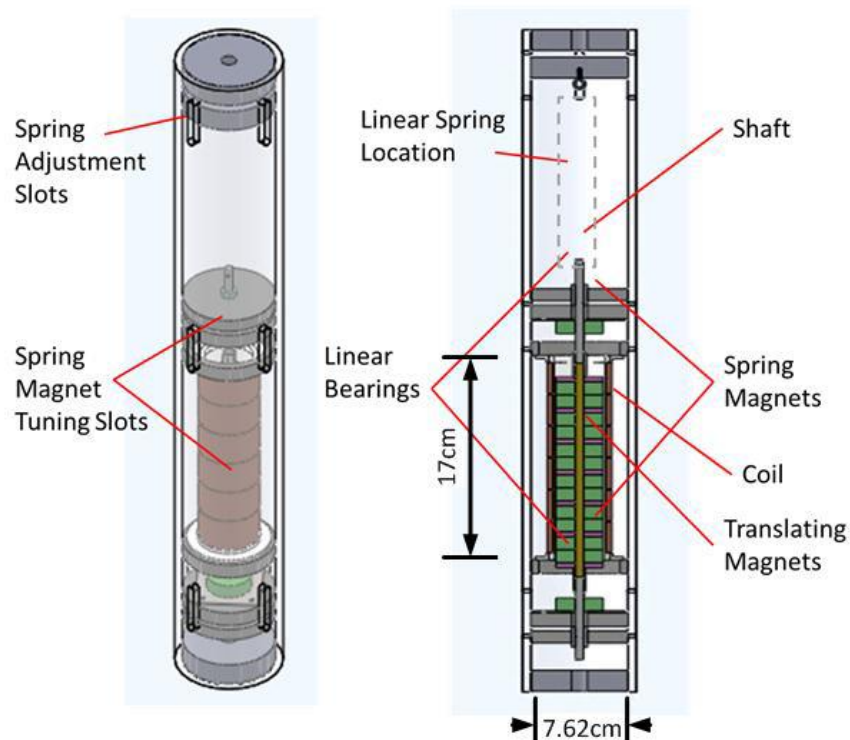


Figure 2.24. Solid model of (Dierks, 2011) test prototype.

During fabrication, the prototype was subject to several manufacturing limitations that altered its final parameters from the desired values. During winding, the coil was damaged such that one-sixth of the intended length was removed from one end. In addition, the bobbin the coil was wound on had an internal diameter larger than desired. This left less room for windings than originally intended. Combined with the removed section at one end, this resulted in significantly fewer windings than anticipated and decreased the expected total magnetic flux through the coil. This was likely partly to blame for the reduced power output seen during testing.

The prototype was tested using an EM shaker table and data was logged using National Instruments hardware running the LabVIEW software. A number of tests were performed to verify measurements from the numerical model and set an optimal load resistance to maximize power for a given configuration. Figure 2.25 demonstrates the peak power performance for the device as a function of acceleration amplitude at a frequency similar to that used in the numerical trials.

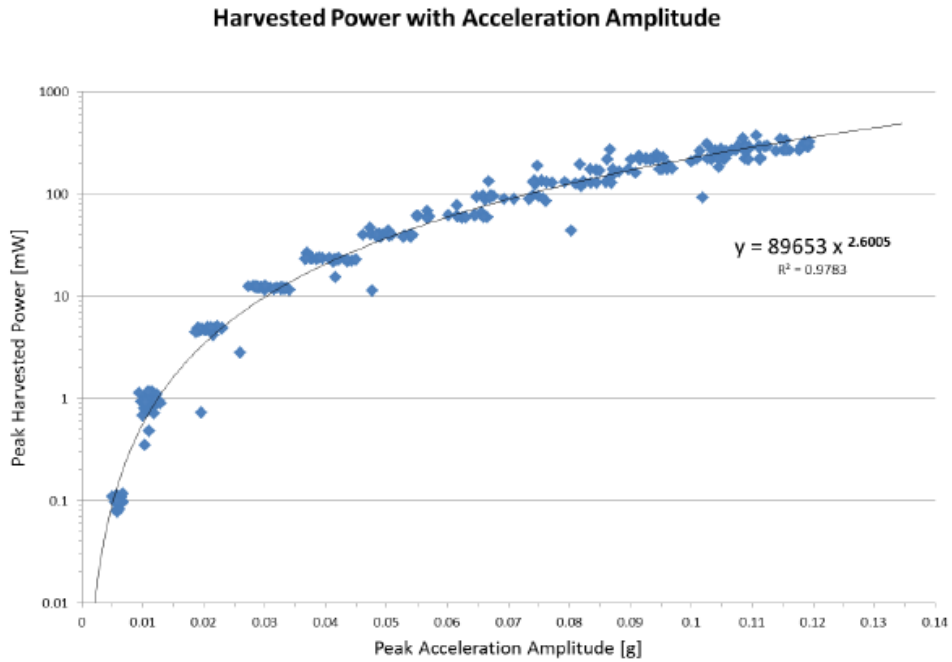


Figure 2.25. Peak harvested power as a function of peak acceleration amplitude for a sinusoidal excitation at 2.2 Hz and 14 k Ω load (Dierks, 2011).

While the curvature matches the numerical model, the associated peak energy harvested is substantially diminished. This is at least somewhat expected, given the efficiency losses and discrepancies from the desired geometric parameters. A similar pattern was embodied by the frequency sweeps used to verify that the harvester provided the greatest power at the expected resonant frequencies (Figure 2.26).

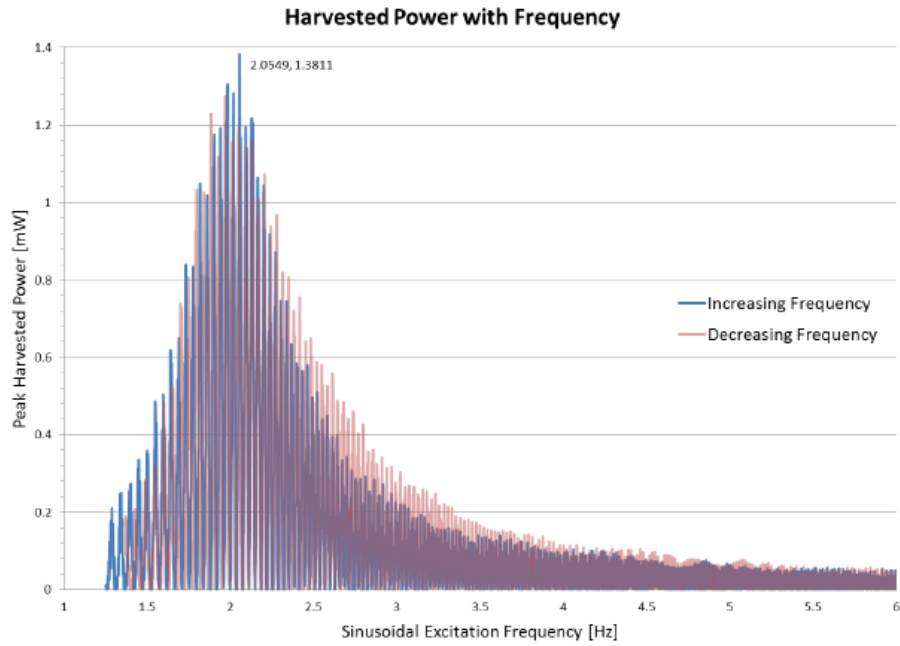


Figure 2.26. Peak harvested power as a function of increasing and decreasing frequency sweeps with acceleration amplitude of 0.01 g and load resistance of 14 k Ω (Dierks, 2011).

Finally, a test was run to capture the total power output using a 50 second sample of data from a Medina River Bridge accelerometer capture (Figure 2.27). This resulted in an average power output of 80 μ W, or about 6 times less than the desired output of 0.5 mW to power one WSN node. Given the discrepancies in desired versus realized parameters, it should be possible to increase this efficiency. This seems promising as a first iteration. In addition to better conforming to the desired manufacturing specifications, refinements can be made to the mass or damping to increase the power capabilities.

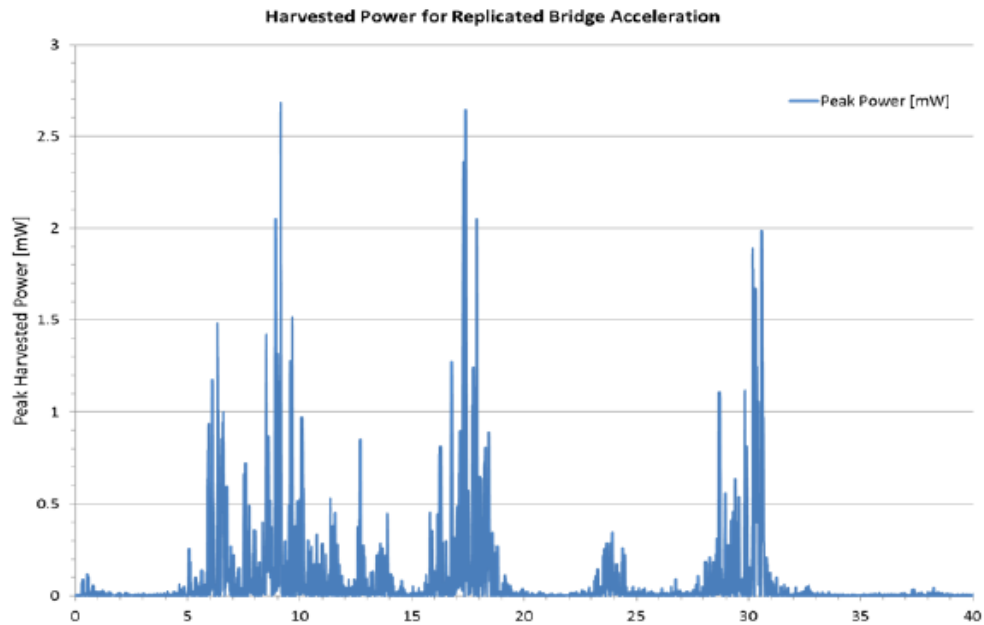


Figure 2.27. Peak harvested power as a function of time for bridge excitation from Medina River Bridge with a load resistance of 14 k Ω (Dierks, 2011).

As the prototype allowed for non-linear magnet springs as well, these were tested using the same conditions as Figure 2.27. Figure 2.28 demonstrates a considerably reduced output, as expected from the simulation studies. While it was found that the non-linear springs allowed for a larger bandwidth, it can be concluded that linear springs are preferred when peak power generation is desired.

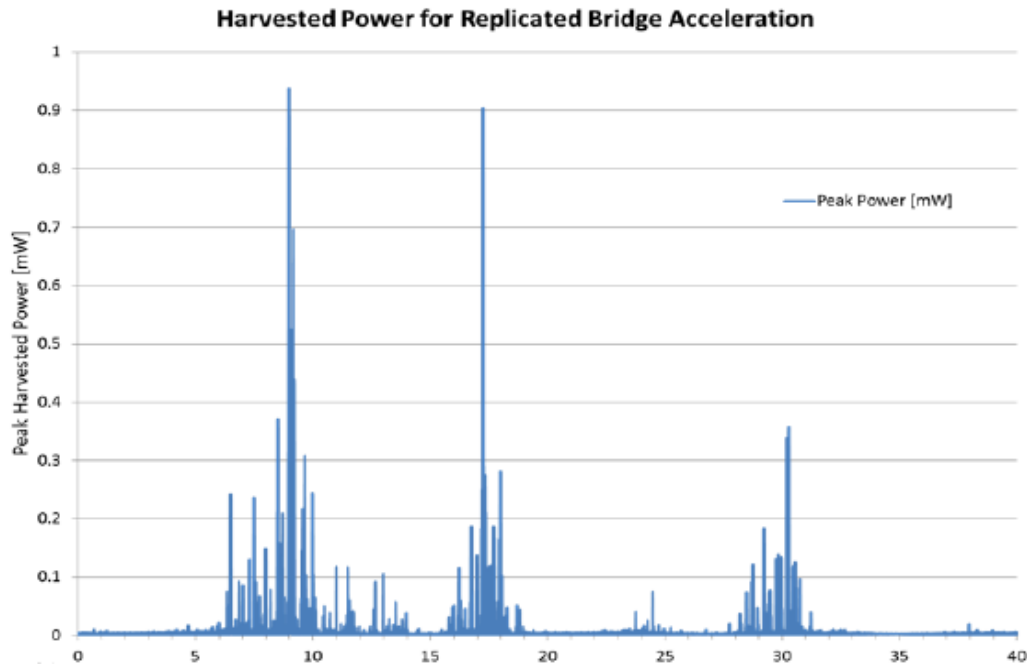


Figure 2.28. Peak harvested power as a function of time for bridge excitation from Medina River Bridge with a load resistance of 14 k Ω and non-linear springs (Dierks, 2011).

2.5.3 Beta Prototype Embodiment

An effort was made to design field ready packaging for the device. This included the development of a prototype housing using laser sintering (LS) technology. Figure 2.29 represents the solid model and Figure 2.30 the completed prototype. This design reduced the total complexity, making an easier assembly during manufacturing. As this was produced in parallel with the experimental prototype, spring magnets were chosen as the stiffness elements. Therefore, a future iteration would require slight elongation to account for a more standard extension spring. The most novel part of this design was the clamping mechanism. It provides two major clamps that can be attached to exposed bridge elements. In addition, they can be rotated 360 degrees, allowing for a multitude of potential mounting locations.

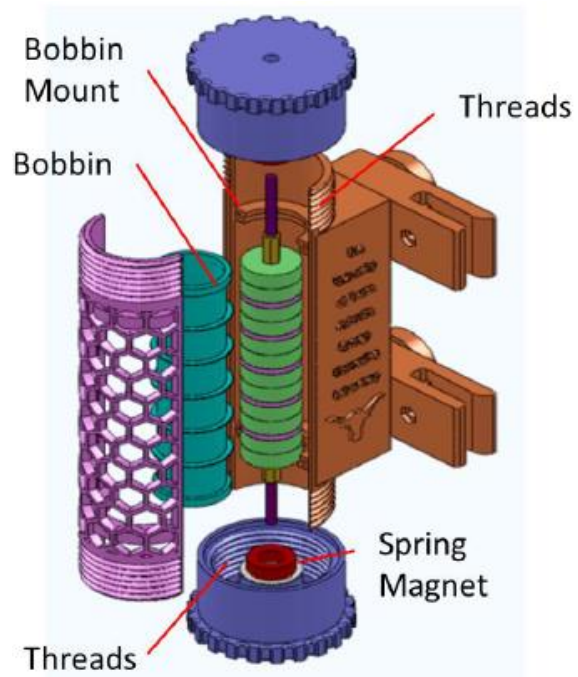


Figure 2.29. Solid model of beta prototype (Dierks, 2011).

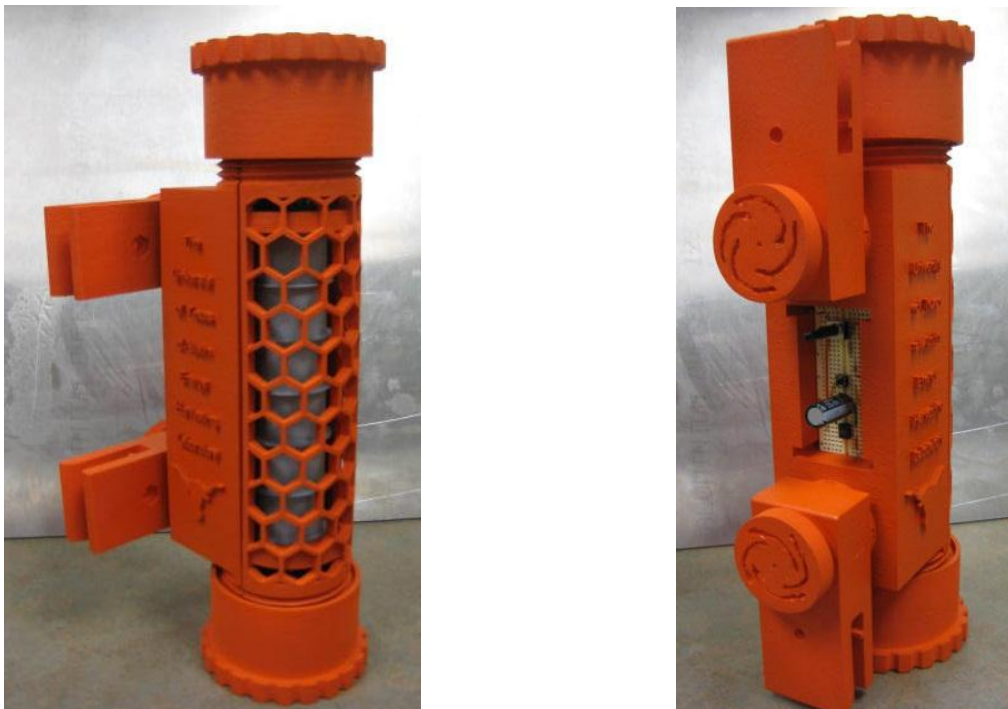


Figure 2.30. Completed harvester isometric and rear isometric views (Dierks, 2011).

2.5.4 Summary of Work by Dierks

The work by Dierks represents a significant undertaking in developing a vibrational energy harvester for a bridge health monitoring network. The numerical model served as a fairly reasonable estimate for predicted performance of a harvester. While the physical embodiment did not provide the expected performance, deviations from the planned geometry due to manufacturing limitations likely played a key role. The tubular, axisymmetric design still seems promising in this type of application with small increases in efficiency and tweaks to the final parameters. The beta prototype represents a significant development in attachment methodology. The proposed design seems feasible and requires no modification to the existing structure while still being relatively quick and simple for an installation crew to deploy.

2.6 CHAPTER SUMMARY

The review of electromagnetic vibrational energy harvesting literature provides several insights. In general, the work by Reichenbach indicates that bridges oscillate at even lower frequencies and amplitudes than those studied in comparable low frequency literature. As these are key attributes in determining maximum power potential, the limitations must be considered for future optimal design work. Additionally, it was found that bridges tend to have minor fluctuations in resonant frequency over their lifetimes due to damage accumulation and temperature fluctuations. A good harvester must account for this using bandwidth compensation via damping and load tuning. The work by Dierks provides an example of a working first iteration harvester using the axisymmetric, tubular designs that are well-represented in low-frequency literature. Improved focus on machining tolerances and careful fabrication make it possible to build a refined prototype that more closely follows a prescribed geometry.

Chapter 3: Development of Numerical and FEA Simulations

The knowledge gained during the literature review was used to develop a simulation to evaluate and explore potential harvester geometry and performance. This chapter reviews the process of modeling the associated physical principles necessary to create an analytical model for the harvester. Then, the work by Dierks (2011) was adapted to develop a numerical simulation using MATLAB (Mathworks, Natick, MA, USA) with Simulink/Simscape for analyzing specific design choices. This evaluation was used to develop the final model for experimental validation in Chapter 4. In addition, an electromagnetic finite element analysis simulation was developed to aid in final design decisions and to check the validity of earlier assumptions.

3.1 ANALYTICAL MODEL

3.1.1 Mechanical Components

As previously discussed, the basic electromagnetic vibrational harvester can be modeled as a second order system consisting of a translating mass (m), damping coefficient (c), and spring stiffness (k). This assumes a linear spring stiffness, which was shown to provide greater power production potential by Dierks (2011). The equation of motion for a second order system is

$$m\ddot{x} + c\dot{z} + kz = m\ddot{y} \quad (3.1)$$

where x is the displacement of the translating mass, y is the displacement of the bridge, and z is the relative displacement between the bridge and mass ($z=x-y$). The damping coefficient is composed of both the mechanical (c_m) and electrical (c_e) damping coefficients such that

$$c = c_m + c_e \quad (3.2)$$

The natural frequency of a spring mass system is defined by Equation 3.3.

$$\omega_n = \sqrt{\frac{k}{m}} \quad (3.3)$$

And a damping ratio (ζ) can be defined as

$$\zeta = \frac{c}{2\sqrt{mk}} = \zeta_m + \zeta_e \quad (3.4)$$

Equations 3.1, 3.3, and 3.4 can then be arranged to form Equation 3.5.

$$\ddot{x} + 2\zeta\omega_n\dot{z} + \omega_n^2z = \ddot{y} \quad (3.5)$$

In addition to a linear stiffness term, the current model only represents the linear viscous friction seen in the system. While this is often adequate for a first-run model, it may be inadequate in cases where viscous friction is not dominant and greater precision is required. In these cases a more complex model for friction can be developed incorporating breakaway friction (also called stiction), Stribeck friction, Coulomb friction, and the viscous component. The Simscape plugin for MATLAB provides an easy means to incorporate such a model. Figure 3.1 describes this model as a function of relative velocity. As the mechanical damping in a vibrational harvester is a pure loss, it is important to minimize this term. Relying only on a viscous model could cause an overestimation in harvester potential, so it is preferred to attempt to incorporate the more complex model in a numerical simulation.

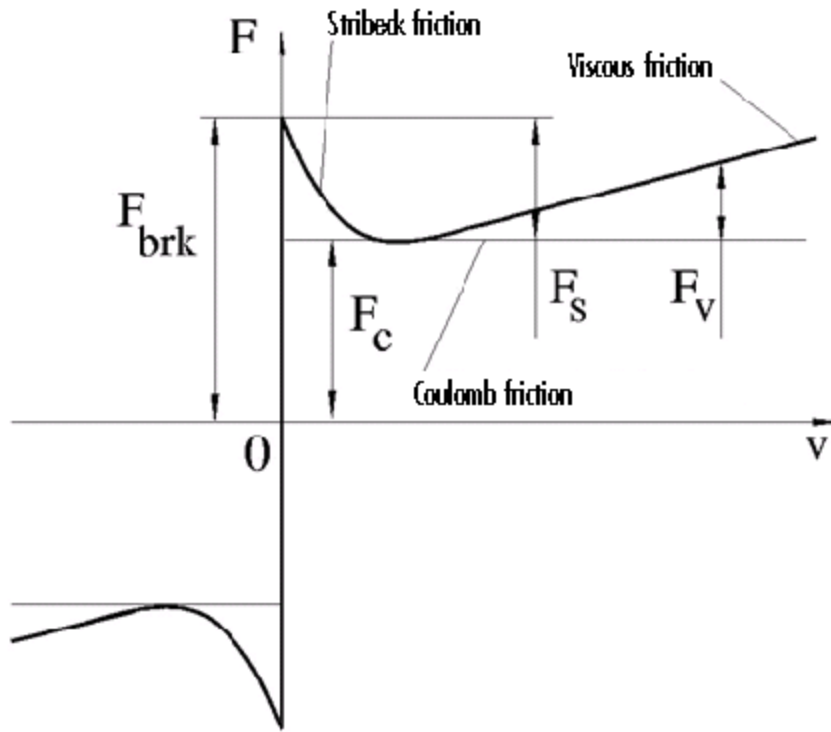


Figure 3.1. Complex friction model (MathWorks, 2014).

3.1.2 Analysis of Electromagnetic Components

The electromagnetic components of an EM generator rely on the law of induction developed by Faraday in 1831 when he discovered that an electrical conductor moving through a magnetic field induces a potential difference between the ends of the conductor. In essence, the induction is used to convert the kinetic energy of the moving mass to electrical energy in a coil (by damping the system). The principle of Faraday's law states that the electromotive force (EMF), or voltage, induced in a circuit is proportional to the time rate of change of the magnetic flux linkage (Φ) in that circuit (Equation 3.6).

$$EMF = -\frac{d\Phi}{dt} \quad (3.6)$$

In the case of a circuit consisting of a number of coil turns (N), the total flux linkage can be calculated as the product of the average flux linkage through each turn (φ) and N , where the average flux is calculated as the area surface integral of magnetic flux density (B) over the total coil area (A).

$$\Phi = N\varphi = \sum_{i=1}^N \int B \cdot dA \quad (3.7)$$

Combining 3.6 and 3.7 yields an expression that represents the EMF by the product of the flux gradient and velocity.

$$EMF = -N \frac{d\varphi}{dz} \frac{dz}{dt} \quad (3.8)$$

Equation 3.9 is then created by calculating the average flux gradient in each term as the product of the average flux density (B_{avg}) and the length of the wire in the coil (l_{wire});

$$EMF = -NB_{avg}l_{wire}\dot{z} = -K\dot{z} \quad (3.9)$$

where K is known as the average electromechanical coupling coefficient.

Using Kirchhoff's voltage law (KVL), Equation 3.10 is obtained, quantifying the induced current (i) and electrical load.

$$-K\dot{z} + i * (R_l + R_c + j\omega L_c) = 0 \quad (3.10)$$

The impedance is composed of the load resistance (R_l), coil resistance (R_c), and coil inductance (L_c). Solving for current, Equation 3.11 follows.

$$i = \frac{K\dot{z}}{R_l + R_c + j\omega L_c} \quad (3.11)$$

The magnetic force (F_e) created by this current opposes the motion of the translating magnet assembly, as shown in Equation 3.12. The force may also be represented mechanically as the velocity-dependent damping force. The electric damping coefficient (c_e) is given by Equation 3.13.

$$F_e = Ki = c_e \dot{z} \quad (3.12)$$

$$c_e = \frac{K^2}{R_l + R_c + j\omega L_c} \quad (3.13)$$

The total instantaneous power (P_e) generated is then represented in Equation 3.14.

$$P_e = \frac{EMF^2}{R_l + R_c + j\omega L_c} = c_e \dot{z}^2 \quad (3.14)$$

This equation can be further broken down into the power dissipated in the load ($P_{e,load}$) and the power lost ($P_{e,loss}$) (largely in the form of heat) in Equations 3.15 and 3.16, respectively.

$$P_{e,load} = \frac{R_l}{R_l + R_c + j\omega L_c} P_e = c_{e,load} \dot{z}^2 \quad (3.15)$$

$$P_{e,loss} = \frac{R_c}{R_l + R_c + j\omega L_c} P_e = c_{e,loss} \dot{z}^2 \quad (3.16)$$

Stephen (2006) found that the maximum power is generated when the resistance in the load matches the impedance of the system. With this information, the optimal load resistance can be calculated from Equation 3.17;

$$R_l = R_c + j\omega L_c + \frac{K^2}{c_m} \quad (3.17)$$

where c_m is the mechanical damping coefficient. Additionally, the coil inductance (L_c) can be calculated with Equation 3.18.

$$L_c = \frac{4}{5} * \frac{r_m^2 N^2}{6r_m + 9h + 10t} \quad (3.18)$$

These are all measurable parameters, including the mean radius for the coil (r_m), total number of turns (N), height of the coil (h), and thickness of the coil (t).

3.2 NUMERICAL SIMULATION

Combining the mechanical and electrical components, a numerical simulation was developed using MATLAB, Simulink, and Simscape. This provided the capabilities to evaluate potential harvester performance under a number of excitations and potential configurations. While the harvester can be evaluated without a specific topology selected, it is important to use feasible values, from both a manufacturing and component availability viewpoint, in order to explore a design space that can be experimentally validated later. Therefore, before simulation work was completed, some decisions regarding a final design topology were made to ease the process of setting simulation parameters.

3.2.1 Initial Design Decisions and Parameter Selection

Certain design parameters can be difficult to estimate without a general final embodiment in mind. One such parameter is the sizing of the translating mass, which is critical to the predicted power output. As no devices in the literature (outside Dierks (2011)) were scaled to the appropriate power generation capabilities, it is necessary to evaluate the device to assure that it can: a) reasonably fit within the structure of a bridge-mounted harvester, b) be manufactured using readily available means, and c) have components that are acquirable in the marketplace at a reasonable cost for a mass-

deployed WSN harvester. Therefore, the parameter sizing process began by examining the translating mass topology.

Several different topologies exist in the literature, including the use of a cantilever beam, an oscillating “mover” (with and without an iron connecting component) with magnets (such as the early work by Clarkson University (Li & Pillay, 2007)), and the opposing pole magnet structure seen in many low frequency applications ((Li & Pillay, 2011), (Saha, O'Donnell, Wang, & McCloskey, 2008), (Patel & Khamesee, 2013), (von Buren & Troster, 2007), and (Dierks, 2011)). Given the prevalence of the opposing pole magnet structure, this general topology was selected. Most works featuring this design do not explicitly detail why their particular component selection was chosen, the notable exception being the work by von Buren & Troster (2007). By creating a lumped parameter model, they were able to evaluate four different potential designs with varying numbers of magnets and coils. After using a simulated annealing optimization algorithm combined with electromagnetic finite element analysis to determine the flux in the coil at discrete translator position, Tables 5 and 6 (from Section 2.3.2) summarize their results. Interestingly, the final results tabulate geometric dimensions as ratios of magnets, poles, and coils. This means the size of the device can be scaled according to final design requirements and the overall geometry optimization is still valid. Therefore, it was determined that these could be used to pursue an initial device configuration.

From their four potential devices, design four represented the best overall concept as it maintained the highest mean EM damping while still maintaining a high max. This was an “even” design as it maintained the same number of magnets as coils. In addition, it had the same number of poles as magnets. The other parameter borrowed from this work was the total number of desired coil turns, with 9,384 turns evenly distributed over the six coils. Table 7 represents the geometric properties compiled from this work.

Table 3.1. Geometric Ratios and Properties Compiled from (von Buren & Troster, 2007)

<i>Parameter</i>	<i>Value</i>
Ratio of Magnet Radius to Outer Radius	0.73
Ratio of Magnet Height to Coil Height	0.86
Aspect Ratio: Total Height to Outer Radius	9.35
Number of Magnets	6
Number of Poles	6
Number of Coils	6
Total Number of Coil Turns	9384

With these values selected, either the magnets or pole pieces must be selected to determine the final dimensions. The magnets chosen for these sorts of harvesters are almost exclusively made of Neodymium Iron Boron (NdFeB) as this is the strongest type of permanent magnet commercially available. This material is notoriously difficult to machine as it loses its magnetic properties if heated above a defined operating temperature (the Curie temperature); usually, the Curie temperature of NdFeB magnets is approximated as 320° C maximum (Precision Magnetics, Inc, 2014). Therefore, it is likely that the commercial availability of a particular size magnet will be the limiting factor when sizing the remainder of the device.

When exploring potential magnets, several key attributes must be kept in mind: a) total mass, b) cost, c) strength, and d) available volume of mounting location. The mass of the magnets themselves represents the majority of the oscillating mass. As shown by Reichenbach (2012), the total oscillating mass is a key component in determining the total harvester power output. Therefore, the largest total mass, and consequently the largest feasible magnets that will fit in the allowable total volume, are desired. In the

bridge-mounted design, the total volume is quite flexible. While minimizing the overall device volume is preferred, it is of lesser concern given the other limiting factors. Large magnets quickly become considerably more expensive than their smaller counterparts. As six total magnets were desired, magnets with individual costs over \$50 were excluded to maintain a reasonable total final production cost. Another concern is that large axially magnetized cylindrical magnets can have pull-off forces exceeding 300 lbf. This can make manipulation during assembly difficult and can even create a safety hazard if “pinching” between magnets is not avoided. Lastly, available magnets tend to come in sizes in $\frac{1}{4}$ inch increments at smaller sizes, increasing to $\frac{1}{2}$ inch increments above 1 inch in diameter.

With these criteria in mind, magnets were chosen with a 1.5 inch outer diameter and 1 inch thickness, as they represented a reasonable trade-off between total mass, size, and strength. Using this as the starting point, the remaining parameters were calculated. It should be noted that, given the arbitrary magnet sizes found in the marketplace, it was not possible to explicitly meet all the criteria provided by the ratios selected. Therefore, when applicable, the first two were preferred in determining dimensions as the aspect ratio tended to lie on a boundary condition in the von Buren optimization that simply suggested tall and slim systems are preferred. Table 8 represents the parameters selected for the oscillating mass.

Table 3.2. Translating Mass Parameters

<i>Parameter</i>	<i>Value</i>
Height of Magnet	1 in
Height of Pole	0.14 in
Magnet/Pole Diameter	1.5 in
Number of Magnets/Poles	6
Translating Assembly Mass	3.275 lbm
Desired Resonant Frequency	2.0 Hz
Spring Stiffness	1.340 lbf/in

The mass of the translating assembly was calculated from the material properties of NdFeB and iron (for the poles). Once this was known, a resonant frequency was chosen based on spectral analysis of available acceleration data from the IH-35N-US-290E Bridge (Figure 3.2). It should be noted that this is still an arbitrarily selected value for this data set, and for any given deployment location the desired resonant frequency must be correlated with the available excitation data spectral analysis. With a known mass and desired frequency, the desired spring stiffness can be calculated using the expression $k = m\omega_n^2$. For a known mass, the correct spring stiffness should be recalculated for any desired excitation frequency.

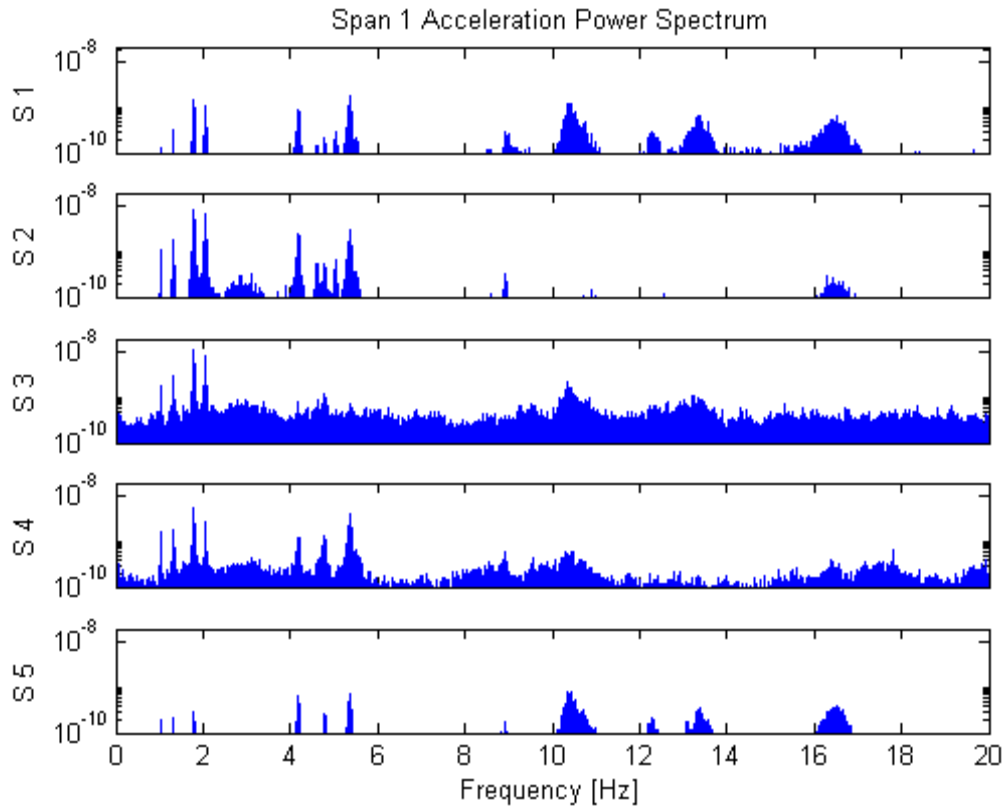


Figure 3.2. Spectral analysis results for 5 spans of the IH-35N-US-290E Bridge.

Once the translating mass parameters are selected, the coil parameters can be computed. Table 9 illustrates the selected parameter values. The outer radius is computed from the ratios previously mentioned. The inner radius should be located as close to the magnets as is feasible to minimize flux leakage in the air gap. To help determine this, a machinist was consulted to determine the feasible values to ensure adequate clearances. The key component to consider is the bobbin the coil will be wound on. The act of boring a soft material, such as a plastic, that could be used to wind the bobbin can be challenging. As the boring tool has a tendency to flex over the length of tube, it can leave the two ends with different radii. Therefore, a 0.050" clearance between the magnet and inner bobbin radius was chosen as a safe value. Additionally, the bobbin material itself

must take up some space between the magnet and inner coil radius. This was chosen to be 0.025” to make sure the material has adequate structural strength while reducing the thickness to an acceptable level.

Table 3.3. Coil Parameters

<i>Parameter</i>	<i>Value</i>
Coil Outer Diameter	2.055 in
Coil Inner Diameter	1.6 in
Coil Height	1.14 in
Number of Coils	6
Total Number of Turns	9384
Wire Gage	30 AWG
Resistance	405 Ω
Inductance	934 mH

The coil wire gage was calculated from the available volume, such that the wire diameter (w_d) was found from

$$w_d^2 = \frac{4fV_T}{\pi N} * \left(r_i + \frac{(r_o - r_i)}{2} \right) \quad (3.19)$$

where f is the fill factor (from 0 to 1), N is the number of turns, r_o and r_i are the outer and inner coil radii respectively, and V_T is the total volume calculated from Equation 3.20.

$$V_T = \pi(r_o^2 - r_i^2)t \quad (3.20)$$

The coil thickness, t , refers to the height of the coil. The resistance (R_c) was calculated from Equation 3.21;

$$R_c = \rho \frac{N^2 \pi (r_o + r_i)}{f (r_o - r_i) t} \quad (3.21)$$

where ρ is the resistivity of the coil material. The inductance can be calculated using Equation 3.18 previously discussed.

3.2.2 Performance from Simulation

Using the previously prescribed parameters, a series of tests was performed using a pure sine input to explore the effects on harvester output. First, a test was performed that swept the load to identify the optimal load resistance. Figure 3.3 presents these results. Based on this, at an oscillation frequency of 2 Hz, the harvester generates the greatest power at approximately 2.75 k Ω . Additional tests were performed, implying that the amplitude of vibration does not change the load resistance for a particular frequency harvester, as expected. For the remaining sine tests, this was subsequently set as the load resistance to generate the maximum power output.

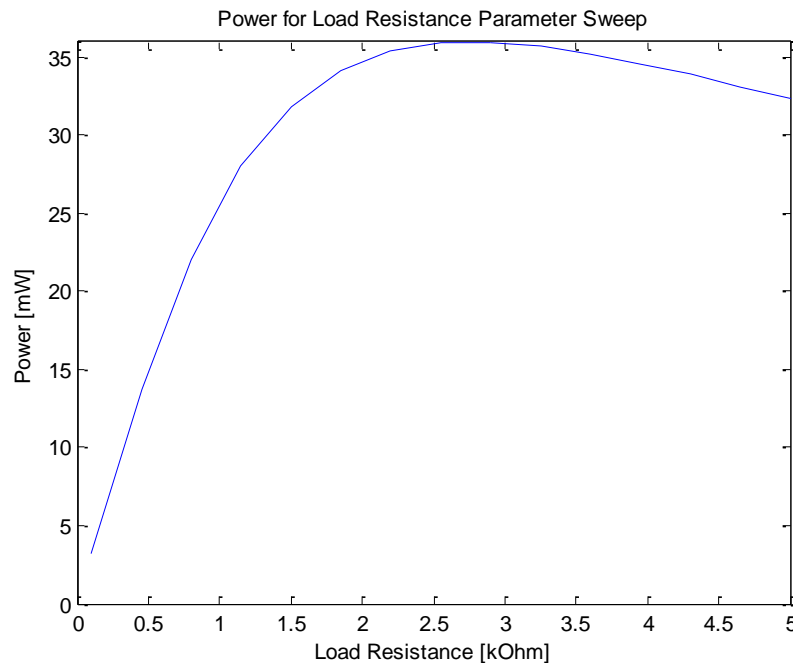


Figure 3.3. Load resistance sweep at 2 Hz sinusoidal frequency and 0.01 g amplitude.

Next, the effect of oscillation amplitude on the harvester was explored by sweeping the amplitudes from 0 to 0.12 g. Figure 3.4 plots these results with a logarithmic power scale. As can be inferred from Equation 2.3, greater amplitudes show significant increases in potential harvester power output. A single order of magnitude increase in amplitude increases the power output by approximately two orders of magnitude, coincident with the results previously shown by Dierks. Figure 3.5 provides the power output using an excitation frequency sweep. Note that the maximum power output actually occurs just above the resonant frequency of the harvester. This could be an artifact of greater power output occurring at higher frequencies, indicating that the increase in power potential with a slightly higher frequency is large enough to overcome the currently tuned natural frequency.

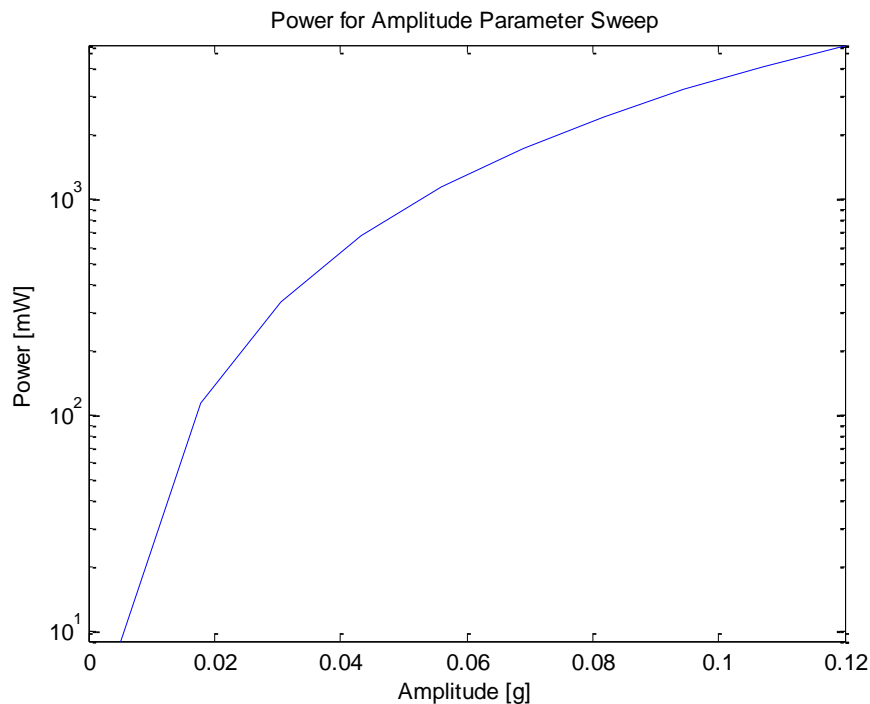


Figure 3.4. Oscillation amplitude sweep with 2 Hz resonant frequency and 2.75 k Ω load resistance.

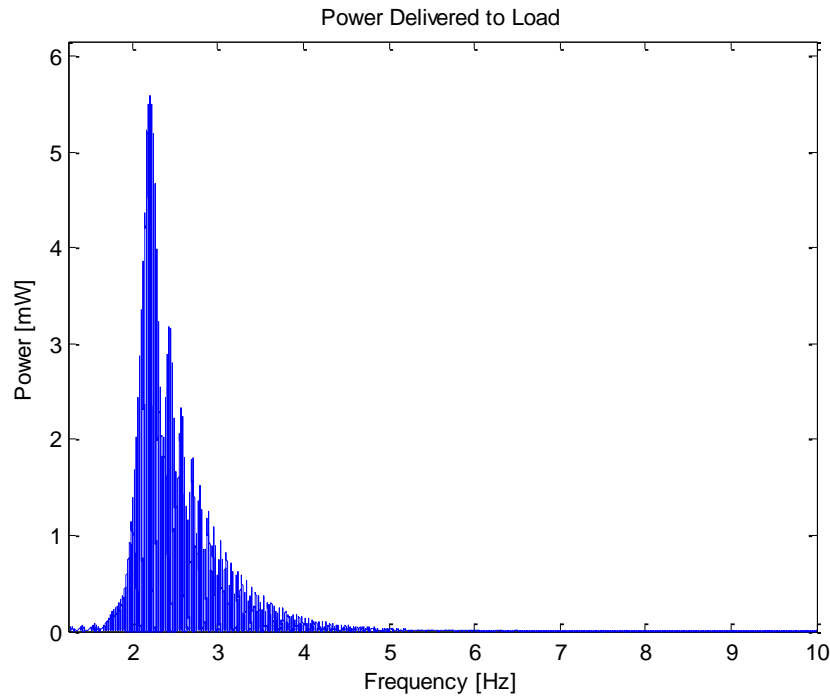


Figure 3.5. Excitation frequency sweep for harvester tuned to 2 Hz resonant frequency at 2.75 k Ω load resistance.

In order to further understand the energy generation potential for the vibrational harvester, several simulations were performed using samples of acceleration data taken from the IH-35N-US-290E direct connector bridge. To best determine the optimal power output, first a frequency sweep was performed using the relevant data to determine the optimal harvester resonant frequency. Once this value was set, a load sweep was performed (similar to Figure 3.3) to optimize for the load resistance. Figure 3.6 presents the results of the analysis. In addition to the instantaneous power output, the excitation acceleration signal, calculated relative displacement (z), and energy delivered to the load over time are plotted for reference.

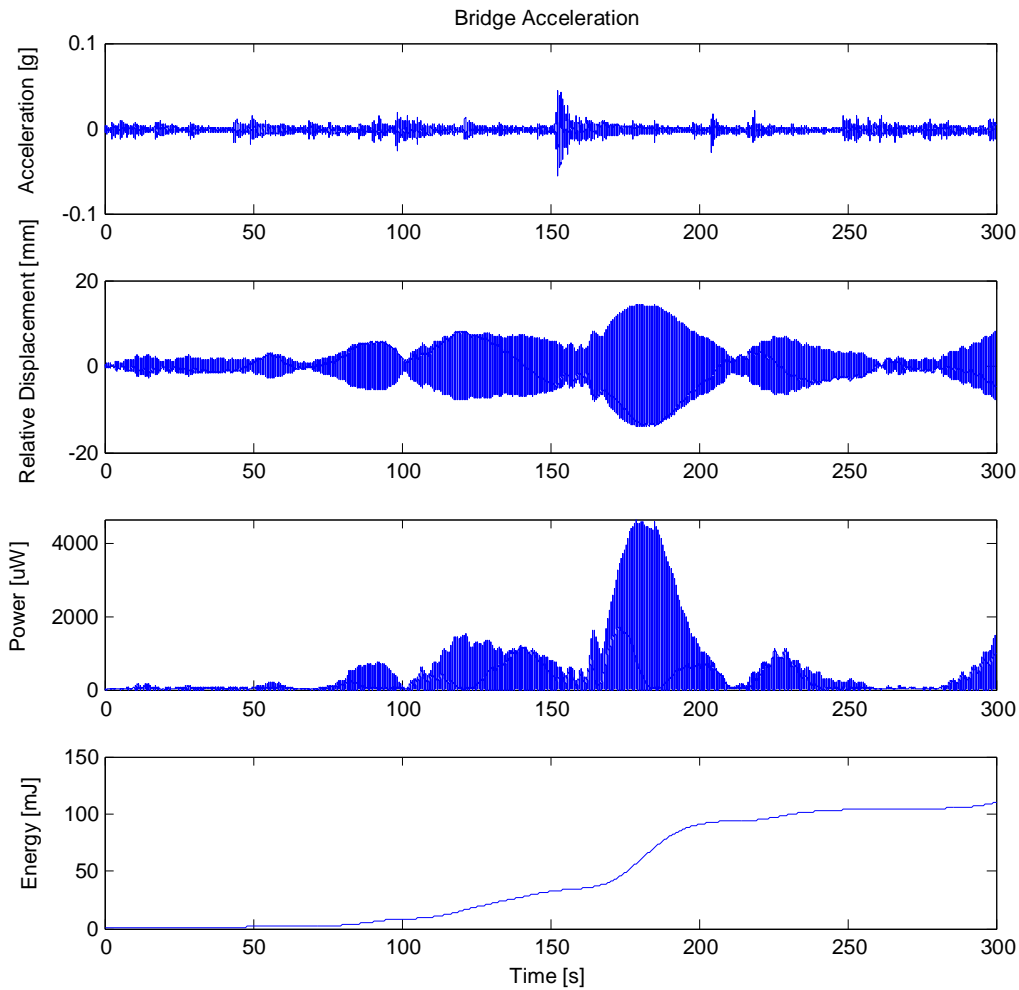


Figure 3.6. Acceleration excitation (1), the associated relative displacement (2), instantaneous power output (3), and energy dissipated in load (4) for 300 seconds of data from the IH-35N-US-290E Bridge at 1.8 Hz resonant frequency and 2.75 k Ω load resistance.

Figure 3.6 provides insight into several key design aspects. As might be expected from the amplitude sweep in Figure 3.4, the power generated during the peak acceleration bridge event constitutes the majority of the overall energy gathered. This is likely the result of a heavy passing truck. Without these events, the overall power generated is

relatively small. In order to examine harvester “bandwidth”, tests were performed with changing damping values. All results presented thus far used damping values inferred from similar literature, such that the total damping was very small ($\zeta \approx 0.01$), with the electrical damping coefficient an order of magnitude larger than the mechanical damping coefficient ($c_e = 10 * c_m$). To test the bandwidth effect on the energy generated, the harvester resonant frequency was changed from the optimal value of 1.8 Hz to 2 Hz and the simulation from Figure 3.6 was rerun (Figure 3.7). This relatively small change might represent the effect of a small discrepancy in desired vs actual spring stiffness (as this is a relatively small change in stiffness, the precise spring rate desired can be difficult to locate in commercially available springs). Next, the damping ratio was increased to 0.1, as was indicated by Reichenbach (2012) as a good trade-off for bandwidth and power generated, and the electrical/mechanical damping coefficient ratio was maintained (Figures 3.8 and 3.9).

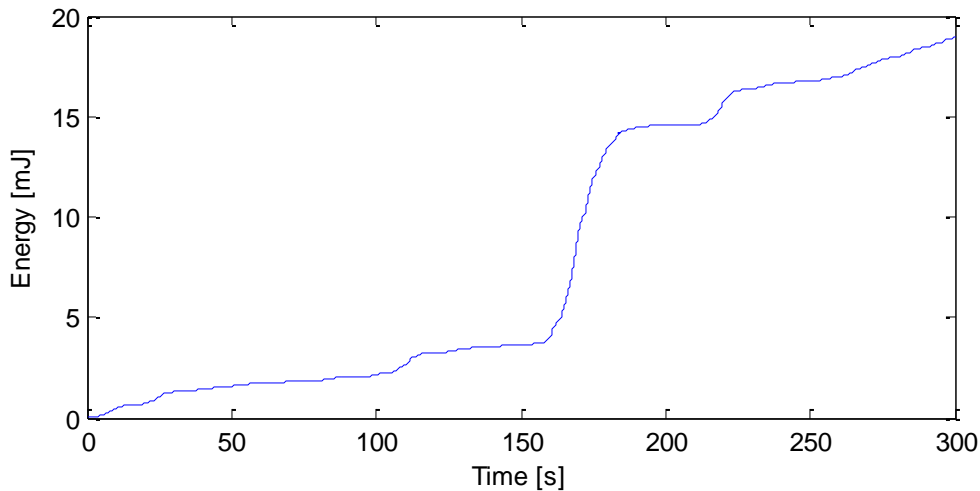


Figure 3.7. Energy dissipated in load for 300 seconds of data from the IH-35N-US-290E Bridge at 2 Hz resonant frequency and 2.75 k Ω load resistance.

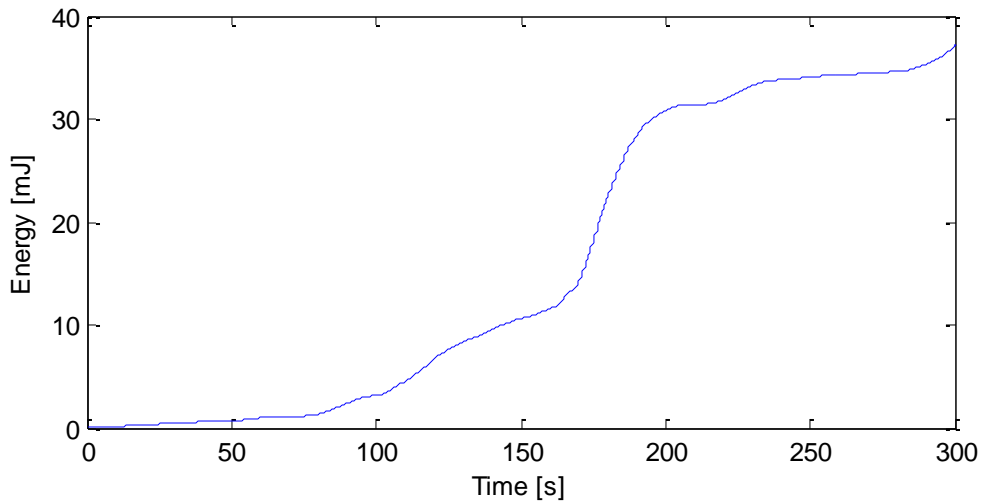


Figure 3.8. Energy dissipated in load for 300 seconds of data from the IH-35N-US-290E Bridge at 1.8 Hz resonant frequency, 2.75 k Ω load resistance, and increased damping ratio.

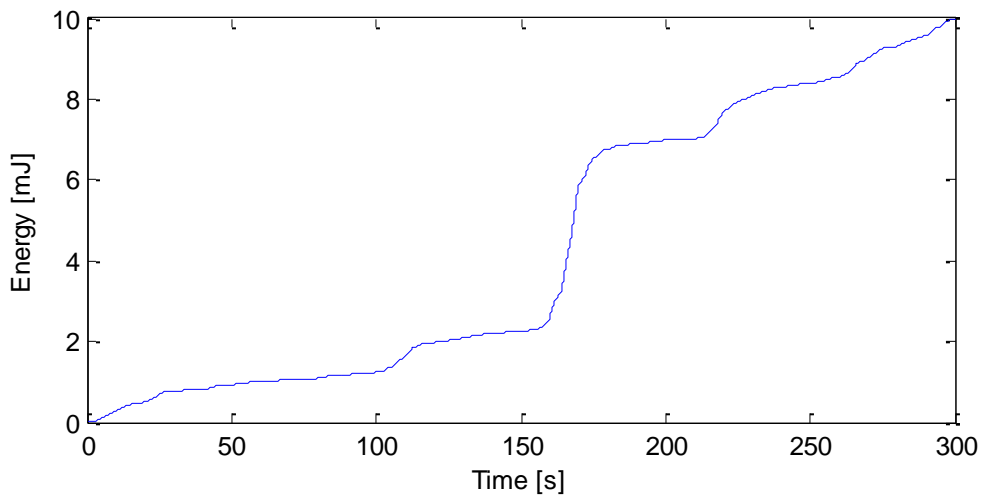


Figure 3.9. Energy dissipated in load for 300 seconds of data from the IH-35N-US-290E Bridge at 2 Hz resonant frequency, 2.75 k Ω load resistance, and increased damping ratio.

First, it can be noted that a harvester tuned to 2 Hz instead of the ideal 1.8 Hz only generates approximately one-sixth the energy over the selected dataset. When the damping ratio is increased to 0.1, the drop in energy is about one-third the original value.

This drop is expected and could be beneficial in a particular application if the frequency offset is such that the damping increase causes a greater energy capture. In this case, however, Figure 3.9 indicates that there is still an approximately 50% drop in energy dissipated at the chosen frequency offset and the higher damping value. While a cross-over point exists for choosing the optimal damping, it seems that if a bridge vibration can be adequately characterized, maintaining a very low damping value is still preferred in this case. This just further confirms the necessity to adequately analyze any potential mounting location so that the harvester may be tuned for the desired bandwidth and frequency.

3.3 ELECTROMAGNETIC FEA ANALYSIS

To help investigate the device parameters and explore material selection, an electromagnetic finite element analysis (FEA) was performed using MagNet software from Infolytica (Montréal, Québec, Canada). The design's axisymmetric nature was exploited to simplify the model by using a 2-D simulation. Figure 3.10 presents the solid model (a) and the calculated response (b). This helps illustrate the basic harvester design. The translator consists of six axially magnetized disc magnets separated by soft magnetic spacers. Neighboring magnets have opposing magnetization directions. The spacers act as flux concentrators that consequently form the magnetic poles and reduce the repellent force between the magnets sufficiently to allow the device to be constructed. The coils are equal in height to a single magnet-spacer combination. The translating mass is offset from the coils such that one of the poles lines up with center of an associated coil at the neutral position. This effectively maximizes the flux in the coils. The coils are wound opposing their neighbors to match the alternating poles and connected in series.

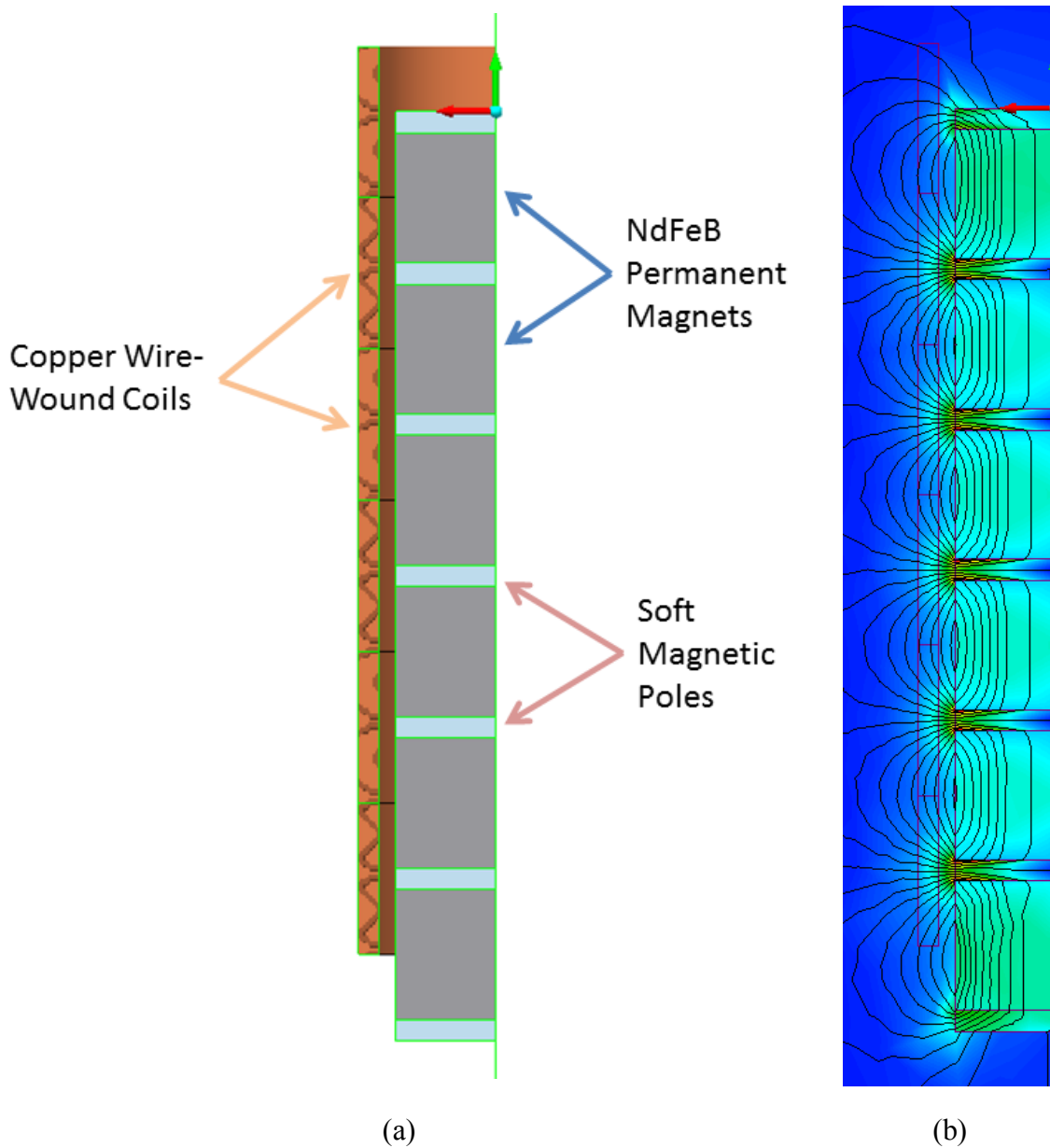


Figure 3.10. (a) FEA solid model (b) shaded plot of resultant flux density and field contour lines.

Figure 3.10 (b) presents a representative shaded plot of the flux density with the magnetic field contour lines. As it is preferred to minimize the flux leakage, it is obvious that minimizing the distance between the translating mass and coils is preferred. Two key

questions were explored with these simulations. First, the addition of a seventh iron pole at the bottom of the system was examined (as pictured). Performing the simulation with and without this component in place, the resultant flux linkage was calculated. From this, it was determined that it has a minimal effect on the flux in the bottom coil and can be ignored (as per the original design). Another concern is the saturation of the magnetic spacers if they are of inadequate thickness. Using the original design parameters, it was determined that a material with a relative permeability on the order of 10^4 was sufficient. This is readily available in the marketplace in the form of low carbon magnetic “core” iron.

3.4 CHAPTER SUMMARY

An analytical model was developed and transformed into a numerical simulation to explore and optimize design parameters. In order to ensure a feasible final design that could be fabricated for experimental testing, a topology was selected based on work by von Buren & Troster (2007). From this, an exploration of commercially available magnets was conducted to begin the parameterization process. Numerical simulations were performed with results indicating several key parameters must be optimized: the load resistance, the natural frequency of the device (by selecting the correct spring stiffness), and the damping for the device. This work also indicates that increases in the excitation oscillation amplitudes can provide orders of magnitude greater power generation capabilities. The development of an EM FEA model concluded that the previously prescribed geometries are viable with materials available in the marketplace. With these values determined, an experimental model can be developed for testing and validation.

Chapter 4: Design Embodiment and Experimental Testing

4.1 EMBODIMENT

The selected design was prototyped for experimental validation. In order to simplify design and assembly, the final design chosen was a simple stacking, modular setup. For this purpose, an outer tubular housing was selected and all internal components were turned on a lathe to a loose fit with the inner diameter (ID) of the tubing. By turning the diameters of the components down on a lathe to the desired dimensions, the overall components maintained axial alignment within 0.005 in. Using this methodology, the internal components simply slide down and stack on one-another during assembly. The ends of the device were then screwed to the side wall of the housing to keep the components stationary in the vertical direction. As the goal for this prototype was laboratory testing, it was manufactured for mounting with the available electromagnetic shaker table. For a more detailed view of the work in this section, Appendix A adds a Bill of Materials and Appendix B contains several dimensioned sketches of the primary harvester components.

4.1.1 Fabrication

In order to minimize magnetic interaction, all primary components were created using nonferrous materials. To begin, a transparent acrylic tube was selected for the outer housing. A transparent housing allows the internal components to be visually inspected for proper alignment during assembly. The inner diameter (ID) required a value larger than the desired coil outer radius, thus a 2.5 in ID tubing with $\frac{1}{4}$ in wall thickness was selected for clearance and strength. Additionally, acrylic provides an excellent medium for the necessary drilling required to mount the end cap components to the sides of the housing as it is not brittle and does not easily crack or chip.

Next, the coil component was fabricated. The bobbin was created from an acetal (marketed as Delrin® by DuPont) tube with 2 in OD and 1.5 in ID. Acetal was chosen due to its machinability, ability to hold tight tolerances, and lack of magnetic interaction. The ID was then bored to allow a 0.050 in clearance with the oscillating mass assembly as per the dimensions from Table 9. Next, 6 slots were cut into the material corresponding to the individual coils to be wound. These slots were cut so as to leave a 0.050 in wall thickness. Additionally, a 0.050 in wall was left between the slots to differentiate between coils during the winding process. Finally, the ends of the bobbin were faced using the lathe as this is critical within the stacking methodology. The completed bobbin is pictured in Figure 4.1 (a).

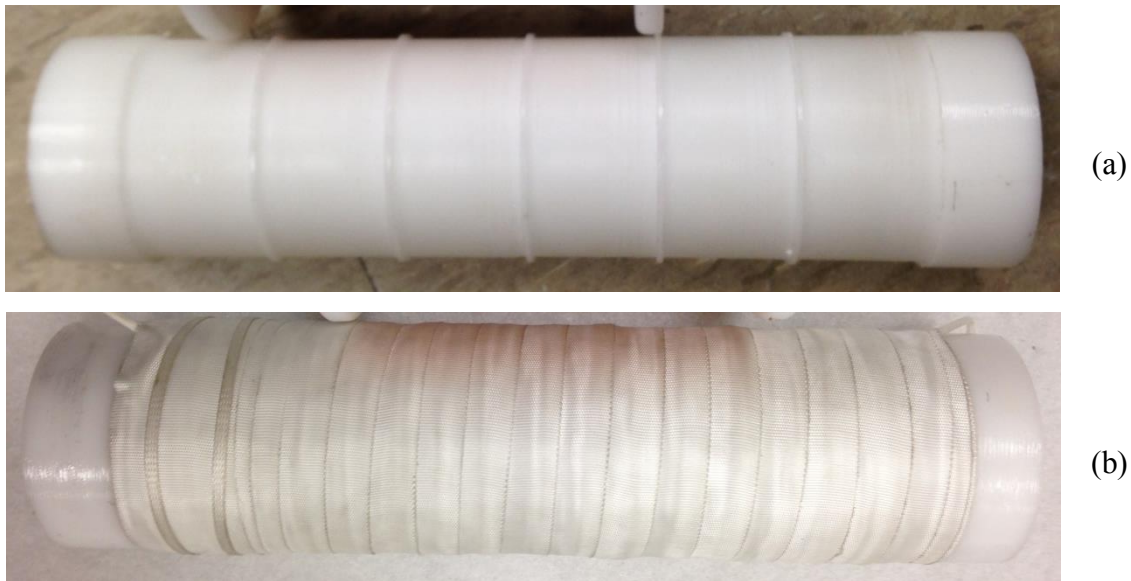


Figure 4.1. (a) Unwound coil bobbin after machining, (b) Finished, wound coil stator.

30 AWG magnet wire was purchased for the coil and the bobbin was taken to a local electric motor shop for winding. In the end, the shop was only able to wind 1300 turns per coil (of the desired 1564) in the available dimensions. The coil was then

covered to protect it during transportation and installation, creating the finished stator. To hold the stator centralized in the housing, mounts were fabricated. Initially, aluminum was considered, but it was found that eddy currents created during oscillation presented considerable damping at the extremes of the translating mass's movement. Therefore, they were also fabricated using acetal resin stock. For this purpose, a 2.5 in acetal bar stock was purchased and the interior was bored to match the interior of the coil (to allow movement of the oscillating mass). Then, the outer diameter was turned down to match the ID of the acrylic housing. To actually mount the stator, a lip was bored $\frac{1}{2}$ in deep into each mount to allow a press-fit between the OD of the stator and the ID of the new mount. The bottom mount was extended 1 in longer than the top mount to account for the offset final magnet location. The mounted stator is pictured in Figure 4.2.



Figure 4.2. Completed stator mounts with coil assembly positioned.

The translating mass is composed of several components. To maintain alignment, a shaft was used with linear bearings. The shaft is made of anodized aluminum precision ground for linear applications. Aluminum was chosen to minimize magnetic interaction. For the mass, a set of N48 NdFeB magnets were acquired from K&J Magnetics (Pipersville, PA, USA), with each magnet having a 1.5 in OD, 0.25 in ID, and 0.5 in length. As 1 in long magnets were desired, the magnets were utilized in pairs to form the

total length. This was due to availability at the time of ordering, and likely resulted in a slight decrease in overall magnetic flux. The spacers were created from a Vim Var Core Iron rod that was purchased from Ed Fagan, Inc. (Franklin Lakes, NJ, USA). This was then drilled and faced to the proper dimensions using an engine lathe. This low carbon magnetic iron has a maximum relative permeability of 10,000, which the FEA indicated would not reach saturation.

The magnets, arranged in pairs, were then installed on the shaft with the desired opposing poles and magnetic flux concentrators placed between. To overcome the repellant forces of the magnets, aluminum shaft couplers with set screws were installed on each end of the magnet system. Finally, a small hole was drilled in the top end of the shaft to allow a helical spring to be attached. The completed translating mass assembly is depicted in Figure 4.3.



Figure 4.3. Completed translating magnetic mass assembly.

For axial symmetry, the aluminum shaft is designed to use linear bearings. Two NB (Hanover Park, IL, USA) steel, fixed-alignment, linear ball bearings were acquired for this purpose and lubricated with oil prior to assembly. To maintain their own alignment inside the housing, bearing mounts were fabricated using 6061 aluminum bar stock. For this purpose, the stock was first turned down such that the OD matched the ID of the acrylic housing, similar to the stator mounts. Next, it was through-drilled to allow ample room for the $\frac{1}{4}$ in shaft translation, and finally this was bored out to accommodate

a press-fit between the linear bearings and mounts. Figure 4.4 presents a completed bearing assembly with a representative shaft positioned inside.



Figure 4.4. Finished bearing and mount assembly.

To complete the design, two end caps and a spacer were created from the aluminum stock. The “spacer” is simply a 6 in hollow pipe that was turned to the proper OD and faced using the lathe; this provides space for the spring to oscillate internally. The end caps were similarly cut and turned to match the proper OD. As their primary purpose is to secure the system to the housing, three holes were drilled and threaded into their OD corresponding to holes drilled in the acrylic housing. The bottom end cap serves a secondary purpose of mounting the harvester to the laboratory testing setup with a long screw through its axis. Similarly, the top end cap was also center-drilled and tapped to allow a threaded brass rod to be screwed through it. This rod is then used to secure the top of the helical spring. As it is threaded, it can be adjusted to modify the neutral position of the magnetic mass assembly for different spring lengths. Figure 4.5 illustrates this.



Figure 4.5. Top end cap with threaded brass rod attached to helical spring and shaft.

4.1.2 Prototype Assembly

Assembly of the prototype is accomplished by simply stacking the components in the outer housing. The first step is to mount the bottom end cap to the testing apparatus. This is accomplished by first attaching an aluminum base plate to the electromagnetic shaker table. Then, the bottom end cap is secured in position using an axial screw. Next, the housing is placed over the end cap and attached using 316 stainless steel hardware. 316 stainless steel was utilized for all hardware as it is austenitic, and therefore has minimal magnetic interaction. After the housing is attached, the remaining components are stacked on top: first, the lower bearing mount, then the stator assembly, then the remaining components. The upper bearing mount, spring spacer, top end cap, and translating mass assembly are installed simultaneously as this is the easiest method to ensure the spring is securely attached to the shaft and end cap. Once all the components are in position, a visual inspection can be performed to ensure proper alignment of all components. Finally, the end cap is secured to the harvester housing. The completed assembly is illustrated in Figure 4.6.

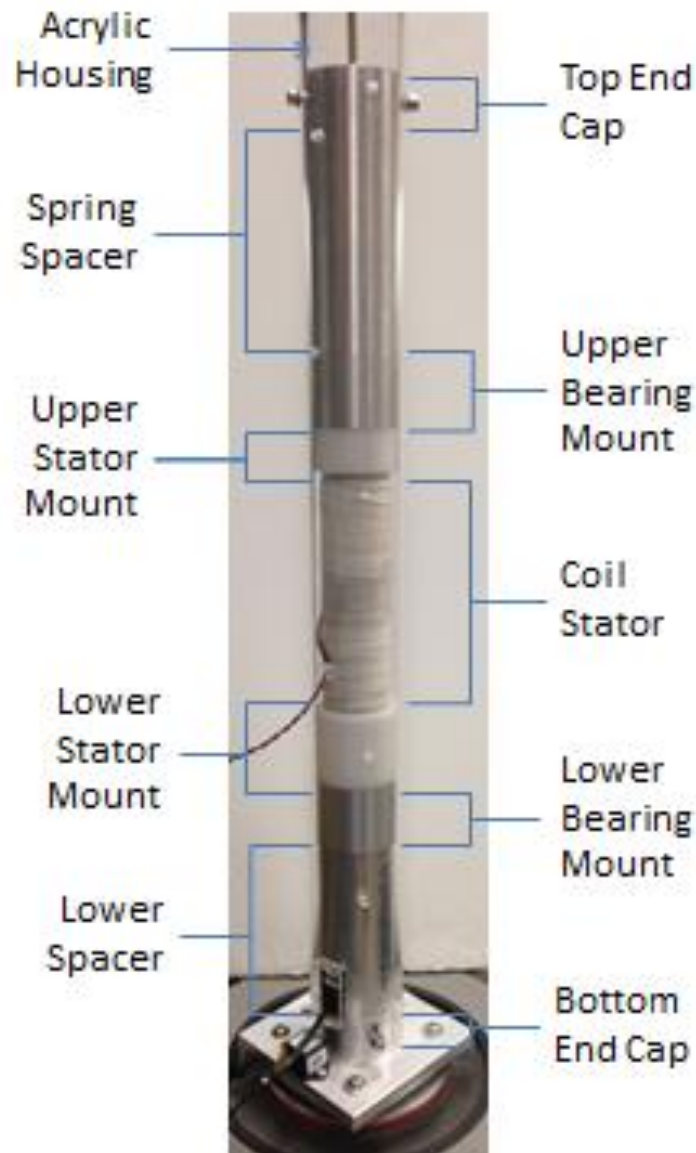


Figure 4.6. Completed harvester assembly with components labeled.

The modular nature of the system allows easy replacement or addition of components. In Figure 4.6, a lower spacer is added to accommodate a laser position sensor capable of measuring the relative displacement of the translating mass. This can also be removed if desired, with the only major modification to assembly being an additional set of mounting holes in the acrylic housing. In this case, the shaft was also

extended to allow measurement by the laser; however, the bearing mount is designed to allow full range of motion internally with the original shorter shaft. All components, excluding the small steel bearings, are non-magnetic so the magnetic fields are not distorted.

4.2 EXPERIMENTAL VALIDATION

4.2.1 Testing Apparatus

A testing apparatus was configured to measure the power generated by the harvester prototype, demonstrated in Figure 4.7. A laptop computer using NI's LabVIEW software was programmed to provide the driving oscillations as well as measure the performance of the harvester. To interface with the system, an NI CompactDAQ was utilized with NI 9269 Voltage Output and NI 9219 Universal Analog Input modules. The driving voltage was sent from the NI 9269 module to a Labworks (Costa Mesa, CA, USA) CP-123 Amplifier Control Panel and PA-123-500 Power Amplifier. The control panel and amplifier then drove a Labworks ET-127 Electromagnetic Shaker Table proportional to the voltage signal sent from the CompactDAQ.

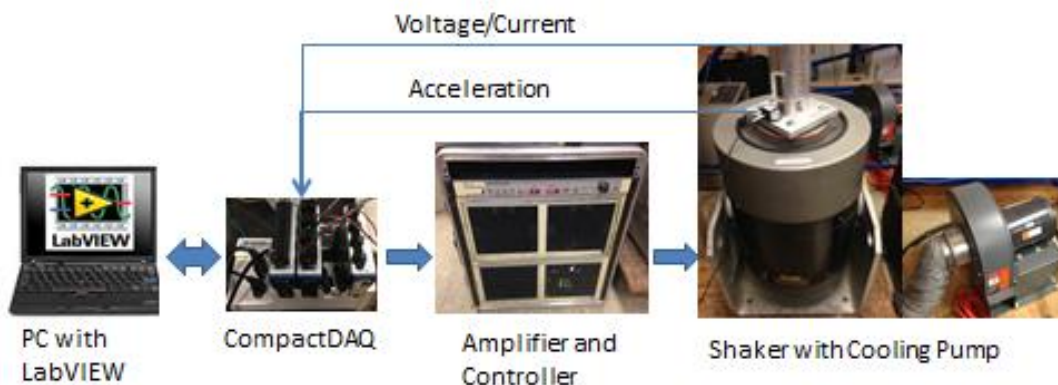


Figure 4.7. Schematic of laboratory testing apparatus.

To verify the harvester excitation matches the desired levels, a Crossbow (Milpitas, CA, USA) CXL04GP1Z single axis, 4G accelerometer was mounted to the harvester base plate. Then, using the accelerometer feedback, the Amplifier Control Panel and LabVIEW control panel gains can be adjusted to match the prescribed oscillation amplitudes. The accelerometer response, harvester voltage output, and harvester current output were recorded using the NI 9219 Universal Input module. Current was measured in series with the load using the module's internal shunt resistor. This system is capable of reading values ranging from +/- 60 V and +/- 25 mA.

4.2.2 Experimental Results

To validate and tune the harvester, a similar process was undertaken to that used for the simulation from Chapter 3. First, to determine the harvester's resonant frequency, a sweep was performed from 1.25 to 4.5 Hz (Figure 4.8) with a constant 0.25 g amplitude and an arbitrary 7 k Ω load resistor. To implement this, a model was utilized that maintained the desired amplitude within 5% over the tested frequency range. The lower bound was limited by the shaker's ability to accurately meet the desired excitations at low frequency levels. From this, the resonant frequency was measured at 1.91 Hz, fairly close to the originally desired 2.0 Hz.

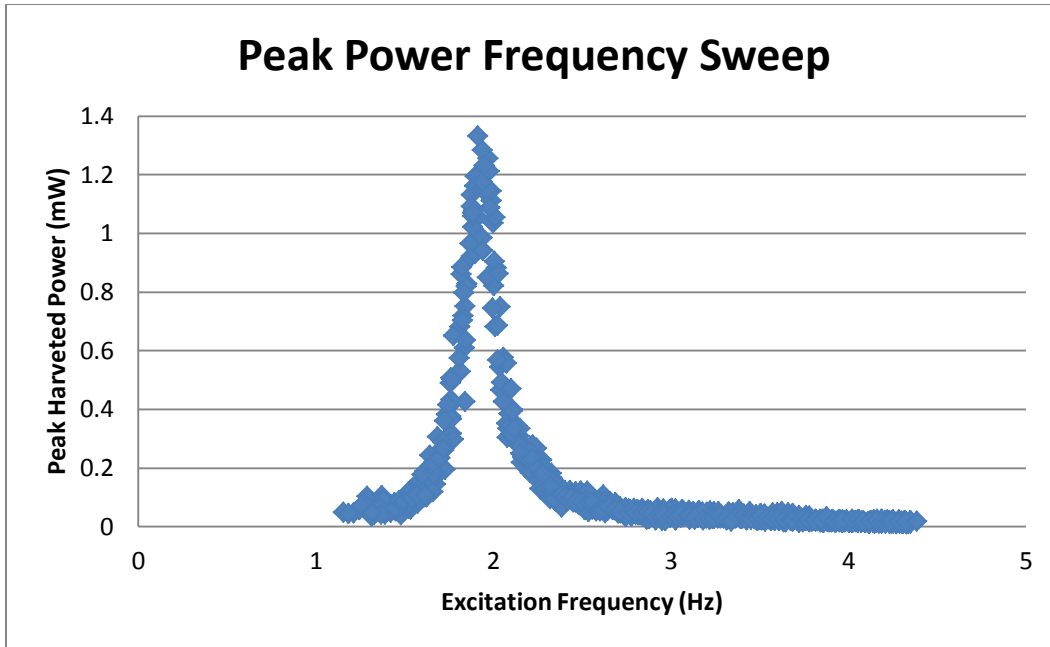


Figure 4.8. Frequency sweep results for 7 k Ω load and 0.25 g amplitude.

Next, the optimal load resistance was determined by varying the attached load from 0 to 10 k Ω using a 10 k Ω potentiometer placed in series with the circuit (Figure 4.9). Interestingly, it was found that the system was relatively insensitive to changes in load resistance as it relates to overall power output potential. Based on these results, a 6.95 k Ω load resistor was selected during further testing.

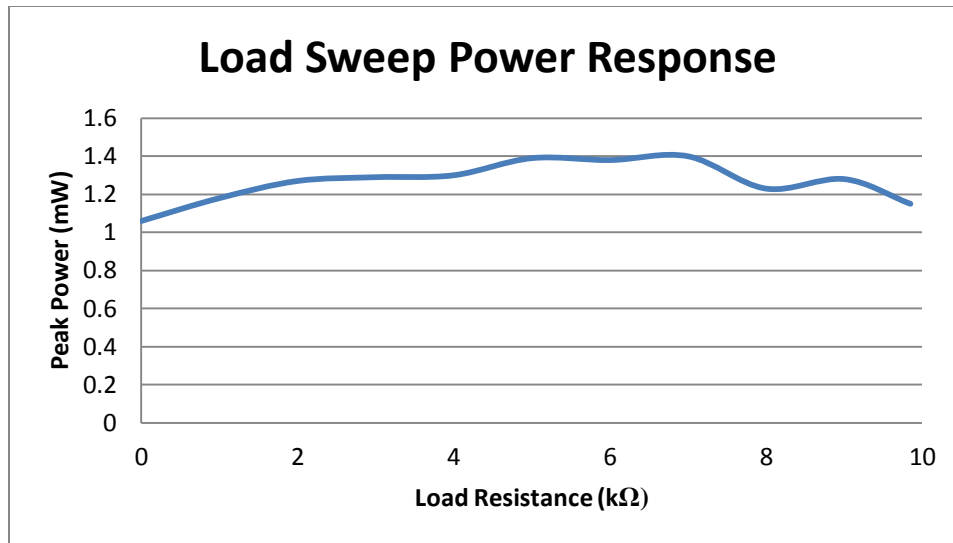


Figure 4.9. Peak harvested power as a function of load resistance at 1.91 Hz excitation frequency and 0.25 g amplitude.

Finally, the response was measured under increasing excitation amplitudes (Figure 4.10). The peak harvested power is plotted on a logarithmic scale versus the excitation amplitude. These results indicate a two order of magnitude increase in power output when increasing the excitation amplitude from 0.01 to 0.025 g. The testing was concluded at 0.05 g as this maximized the harvester’s displacement capabilities. As most bridge excitations gathered fall below this threshold, this was deemed adequate for testing. Interestingly, the increase in power output diminishes considerably after 0.03 g. This is likely a function of the oscillations becoming great enough to move the translating mass out of the desired oscillation region inside the coil.

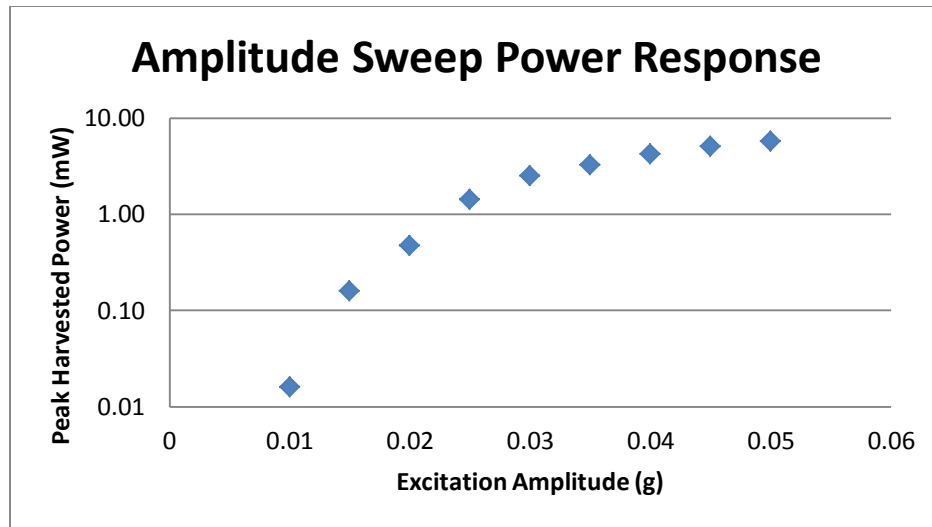


Figure 4.10. Peak harvested power under varying excitation amplitudes with 6.95 k Ω load resistor and 1.91 Hz excitation frequency.

In order to test the performance of the harvester under expected bridge excitations, a 50 second sample of data from the IH-35N Medina River Bridge was used to drive the shaker table. The harvested power was then collected in Figure 4.11 (bottom), while the acceleration as measured by the attached accelerometer was logged in Figure 4.11 (top). The results indicate that the instantaneous power output is generally proportional to the acceleration profile amplitudes as expected. Unfortunately, the results also indicate the average power generated over this time period is less than 10 μ W. This is more than an order of magnitude from providing the necessary power potential for an NI WSN node.

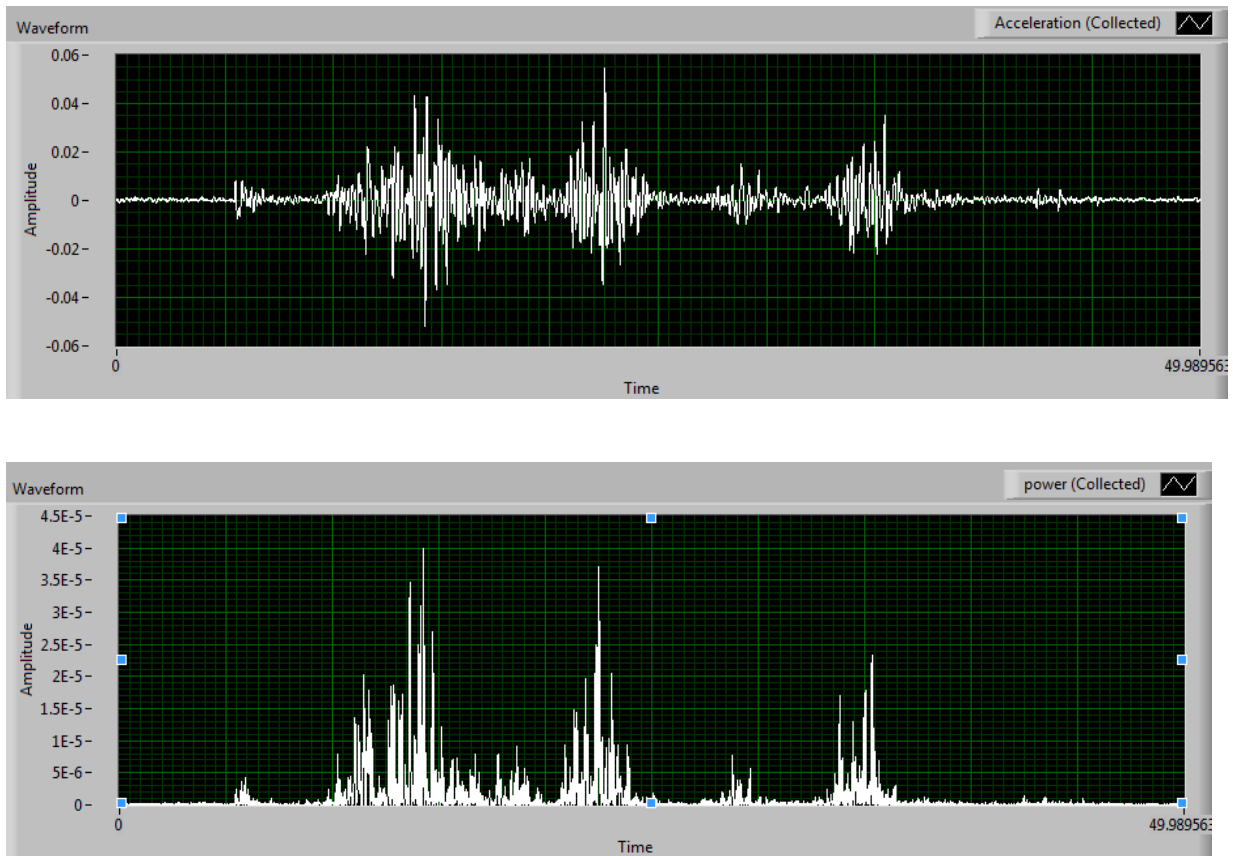


Figure 4.11. Instantaneous harvested power (bottom) under replicated IH-35N Medina River Bridge acceleration data (top) with 6.95 k Ω load.

4.2.3 Prototype Parameterization

In order to understand the diminished power output of the harvester prototype, it was necessary to calculate the final design parameters and compare those to the assumptions used in the simulation work. The first notable difference arose during the fabrication of the coil. The coil was not wound as densely as desired, such that only 1300 of the desired 1564 turns per coil were possible. This decreased the total number of turns from 9384 to only 7800. Next, the spring was tested with known masses to verify the spring constant (Figure 4.12).

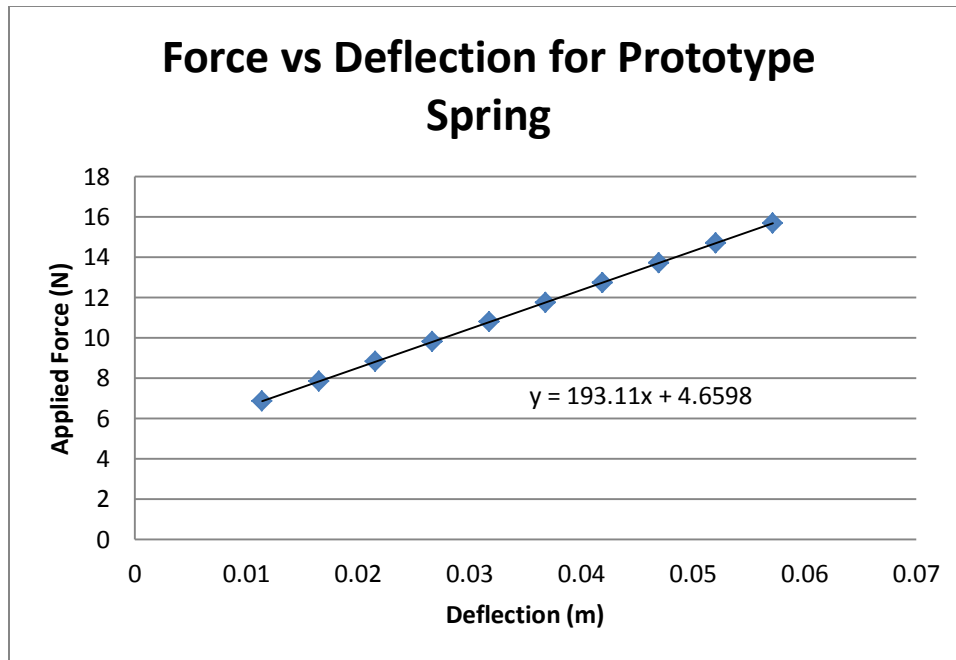


Figure 4.12. Load testing results to determine spring stiffness for prototype spring.

This resulted in a spring constant of 193.11 N/m, or 1.103 lbf/in. Next, the actual translating mass was weighed using a laboratory scale. This resulted in a translating assembly mass of 2.93 lbm, reduced from the 3.275 lbm calculated using expected material properties. These two numbers can be used to find the expected resonant frequency to be approximately 1.91 Hz, corresponding to the value measured using the frequency sweep. Reduction in these values can account for some loss, as was demonstrated using Equation 2.3.

The most important values to measure for the harvester device are the mechanical and electrical damping factors. During simulation work, these values were simulated using values from comparable devices in literature. Additionally, an exploration indicated that while increases in these values increase the bandwidth of the harvester, they also quickly reduce the power output by orders of magnitude. Generally, measurement of the damping parameters for underdamped systems is performed by applying a logarithmic

decrement to the decaying sinusoid created by the device. In this case, the mechanical damping ratio was found by measuring the open loop voltage output from the harvester when an arbitrary initial deflection was provided. Then, the combined damping ratio is calculated using the voltage output measured across the load with the load circuit attached. The difference in these values can then be found as the electrical damping factor.

In general, the logarithmic decrement, δ , is the natural log of the amplitudes of successive peaks:

$$\delta = \frac{1}{n} \ln \left(\frac{x}{x_n} \right) \quad (4.1)$$

where x is the amplitude of a peak and x_n is the amplitude of a second peak n periods away. The damping ratio can then be found using the logarithmic decrement:

$$\zeta = \frac{1}{\sqrt{1 + \left(\frac{2\pi}{\delta} \right)^2}} \quad (4.2)$$

To find the damping ratios, a LabVIEW virtual instrument (VI) was implemented to read the voltage outputs and calculate the damping ratio. A sample is provided in Figure 4.13. Three trials were performed for both the mechanical and combined damping and the average was taken for the results of Table 10.

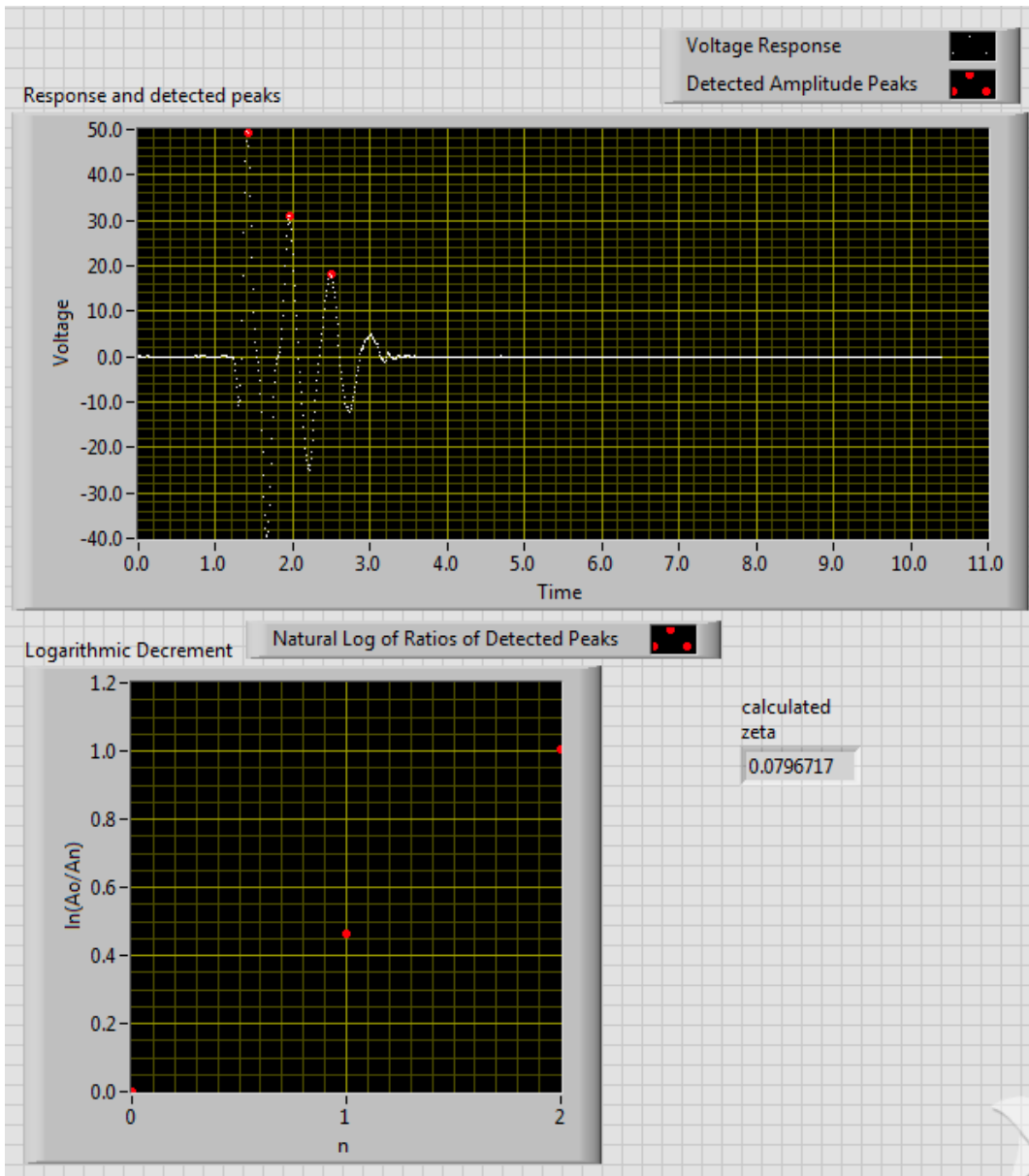


Figure 4.13. Sample of LabVIEW VI Front Panel used to calculate logarithmic decrement and associated damping ratio.

Table 4.1. Measured Experimental Prototype Parameters.

<i>Parameter</i>	<i>Value</i>	<i>Unit</i>
Load Resistance, R_l	6.95	k Ω
Coil Resistance, R_c	399	Ω
Turns per Coil, N	1300	
Translating Mass, m	2.93	lbm
Spring Stiffness, k	1.103	lbf/in
Natural Frequency, f	1.91	Hz
Mechanical Damping Ratio, ζ_m	0.0842	
Electrical Damping Ratio, ζ_e	0.0124	
Total Damping Ratio, ζ	0.0966	
Mechanical Damping Coefficient, c_m	2.699	Nm/s
Electrical Damping Coefficient, c_e	0.397	Nm/s
Total Damping Coefficient, c	3.096	Nm/s

4.2.4 Simulation Results with Prototype Parameters

To better understand the diminished power output results, the actual parameters from Table 10 were used to rerun the simulation of measured IH-35N-290E Bridge data from Chapter 3. The results in Figure 4.14 are consistent with the reduced power generation shown of the prototype. Of greatest effect is the lower than expected electrical damping coefficient. In general, it is preferred the electrical damping show an order of magnitude increase over the mechanical damping, and this was used during the assumptions in earlier simulations. However, the prototype's reduced electromagnetic coupling is indicative of a much lower average flux in the coil than originally desired.

This indicates the selected ratios between magnets, coil dimensions, and the associated air-gap do not meet the expected electromagnetic coupling levels. The ratios were chosen based on previous FEA and optimization work by von Buren & Troster (2007). While their work created ratios that should be somewhat scalable, the design space originally explored was considerably smaller than that incorporated in this harvester. In addition, similar ratios were used in work by Patel & Khamesee (2013), again for a smaller design. In general, it seems these ratios were not adequate to provide the expected flux densities in the coil and considerable leakage resulted when scaled to the desired levels.

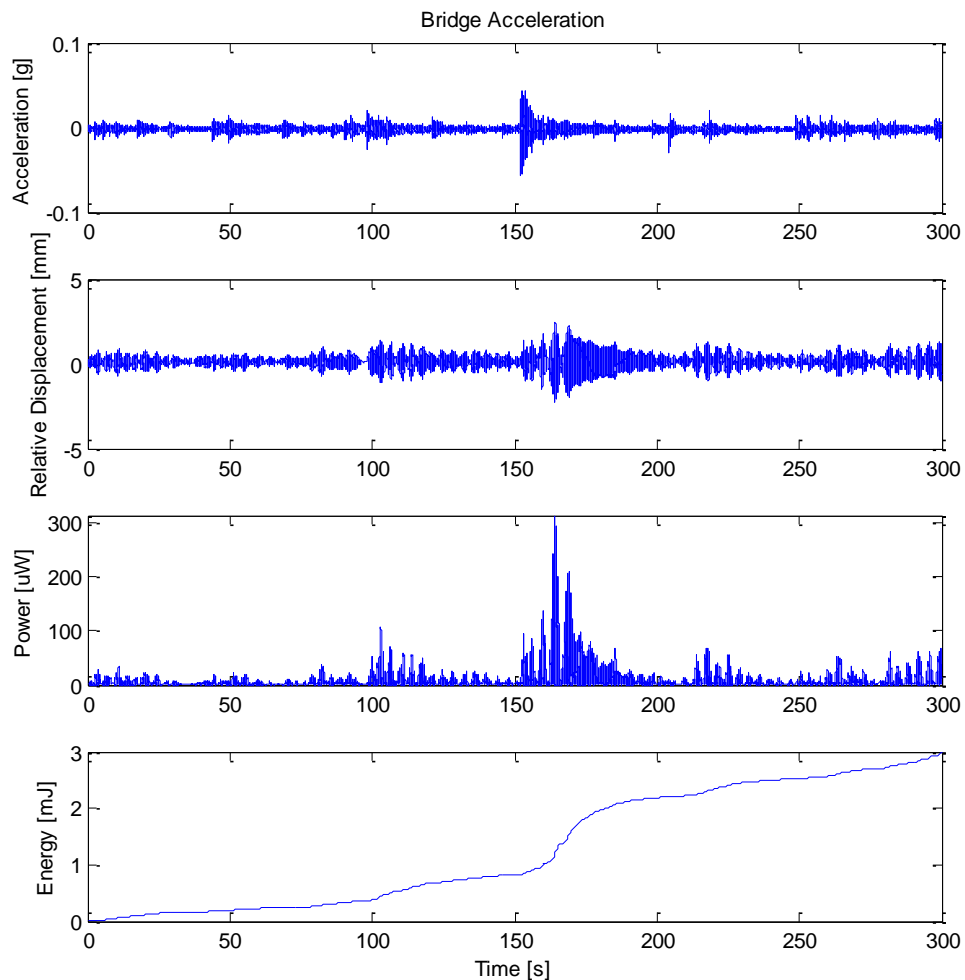


Figure 4.14. Simulation results for actual harvester parameters from Table 10.

4.3 VIBRATIONAL HARVESTING CONCLUSION

The vibrational energy harvesting prototype was manufactured reasonably closely to the desired parameters from Chapter 3. Using modern machining techniques, the tolerances were reduced to help minimize mechanical damping and match the desired parameters as strictly as possible. All components were manufactured using non-magnetic materials to minimize any undesired magnetic interactions. In the end, it was found that the prototyped harvester produced considerably less power than the desired levels indicated by earlier simulation work. The key difference was found in the damping of the system. While the total damping was near desired levels, the mechanical damping dominated the electrical damping by an order of magnitude. This is in direct opposition to the desired ratios. The mechanism behind this is likely a result of the selected geometric ratios based on previous literature originally focused on micro-scale devices. Future work should focus on optimizing the ratios between magnets, poles, and coils in a design space consistent with larger scale harvesters. Based on work by Reichenbach (2012), it would also be prudent to consider a larger overall translating mass. While a design with minimal losses should be capable of producing the desired 0.5 mW at the prototyped mass on some sampled bridges, a larger mass would provide a greater factor of safety and enable the device to function on bridges with lower excitation amplitudes.

Chapter 5: Solar Harvesting Overview and Prototype Validation

For the NIST-TIP project, the Mechanical Engineering team explored energy harvesting technologies for supplying power to the router and gateway WSN components in addition to vibration for the nodes. The gateway is, arguably, the most important single component as it gathers the data from all the individual access points, has the most intense data processing responsibilities, and transmits data offsite through the use of an attached cellular modem. This, in turn, translates to the greatest energy requirements; the combination of the NI WSN Gateway and attached cellular modem is estimated as a 14 W continuous, DC load (Inamdar, 2012). Of the available energy harvesting technologies explored, solar power presents with an order of magnitude greater potential than either wind or vibrational sources (Weaver, Crawford, & Wood, 2010). Solar power harvesting using photovoltaic cells is a mature, highly-scalable technology. This means a properly designed system is the logical choice for reliably powering the most critical WSN component.

The work presented in this chapter serves as a conclusion to the efforts previously undertaken by NIST-TIP team member Inamdar (2012). This chapter first provides an overview of solar power in terms of today's technology. Then a review of the work from the previous team member is presented, concluding with the design chosen for prototyping. Finally, this work details the results of the field testing undertaken and presents a final analysis of the feasibility of the selected design.

5.1 OVERVIEW OF SOLAR ENERGY HARVESTING

5.1.1 Introduction to Solar Power

The Sun bathes the Earth in enough energy in an hour to fuel the entire human race's energy needs for an entire year (Lewis, 2007). Long-term, reliable harnessing of

this energy for transitioning away from a fossil-fuel driven economy is still under development; however, the use of solar power in localized settings/devices is already an effective means to provide energy when grid-scale power access is unavailable. Solar energy harvesting can take several forms, but the most common are the “solar modules” or photovoltaic (PV) arrays designed to convert the solar energy directly to a DC electrical output.

Solar panel modules found in consumer equipment generally rely upon the photovoltaic effect to produce electricity. When light is incident upon a material surface, the electrons in the material absorb some of the energy from the photons and become free. This allows the free electrons to be harnessed to form an electric current. There are two primary types of PV technologies currently available in the marketplace: crystalline silicon panels, divided into mono and polycrystalline silicon, and thin film solar cells. Generally, thin film cells are the cheapest of the three on a “per Watt” basis, with poly next and monocrystalline cells being the most expensive. Conversely, monocrystalline cells support the highest efficiencies with the market leaders now over 20%, polycrystalline generally perform just over 15%, and thin film panels between 12 and 14% (Maehlum, 2014). Additionally, cells have been created in a lab setting (but are not currently feasible for mass production) that have reached efficiencies over 44% (Phys.org, 2013). With this in mind, the selection of a particular cell must include trade-offs among economic limitations and the acceptable power density for a given application.

Commercially available solar panels are usually composed of an array of individual solar cells. These are internally connected, either in series to increase total voltage output, or parallel to increase current. If the power requirements for a particular application are large, an array of PV modules is generally preferred over a single large

module. This eases installation and reduces interference effects that multiple solar cells connected in parallel may encounter.

5.1.2 Key Factors in a PV System

In order to estimate and size a photovoltaic array, a number of factors must be considered. Insolation is the amount of solar radiation received on a particular surface area during a given time. This can be affected by numerous factors, such as the tilt of the Earth in relation to the Sun, the angle at which the panel is tilted, and current weather factors. In general, the amount of insolation received at the Earth's surface is approximately 1000 W/m^2 ; reduced from the total extraterrestrial power density of 1367 W/m^2 at the top of Earth's atmosphere (Inamdar, 2012). Figure 5.1 breaks down the levels of solar irradiance at different levels on Earth with respect to the wavelength of light.

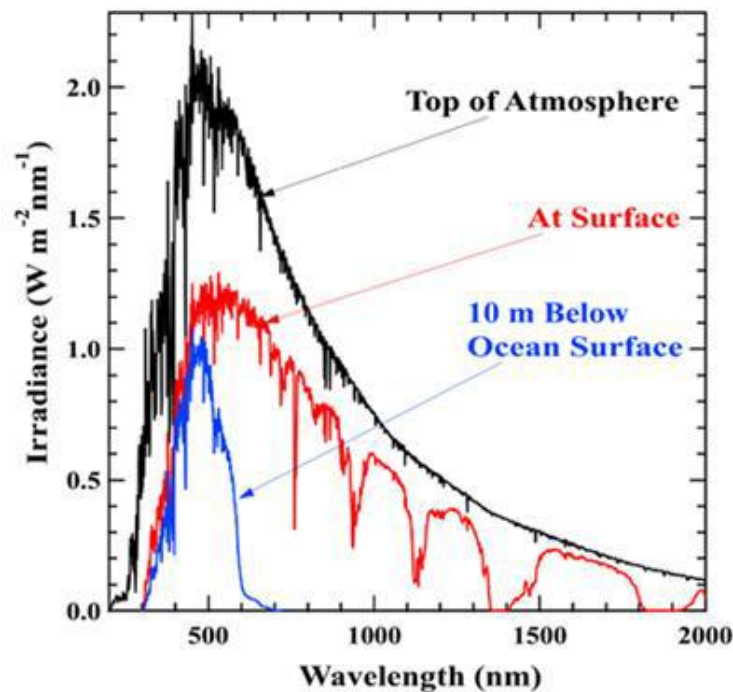


Figure 5.1. Solar irradiance spectrum at Earth's atmosphere and surface (LASP, 2014).

While this can be used as a general theoretical maximum power density available to a particular panel, the actual power density will likely be lower. Any change in geometric relations (from a panel statically mounted at a particular “tilt”) whereby the panel is not perpendicular to the Sun will result in a decrease in energy density. Additionally, adverse weather conditions have a direct effect on the amount of solar radiation that reaches the surface. While general cloud cover will not totally negate a PV panel’s ability to produce electricity, it will likely decrease the output. As weather for a particular location is somewhat random and unpredictable, models to predict the power production capabilities for a particular geographic location must rely on historical data. To aid in this process, repositories are available from sources such as the National Renewable Energy Laboratory (NREL) with historical data for hourly insolation of more than 1000 locations around the United States.

In order to maximize the power output of a PV array, it is desired to maximize the time the panel spends normal to the Sun. This can be quantified by the angle of incidence, i . The angle of incidence describes the angle between the normal to the solar collector and a line collinear with rays from the Sun; therefore, this angle is minimized for maximum power production. Equation 5.1 describes the relationship:

$$i = \cos^{-1}(\cos \alpha \cos(\alpha_s - \alpha_w) \sin \beta + \sin \alpha \cos \beta) \quad (5.1)$$

where α is the solar altitude angle, α_s is the solar azimuth angle, α_w is the panel azimuth angle, and β is the tilt angle. The panel azimuth angle and tilt angle are adjustable parameters defining the geometric orientation of the PV panel. The solar altitude angle provides the angle between the horizon and incidental solar radiation. The solar azimuth angle describes the Sun’s angular position east or west of solar noon, where solar noon is defined as the moment at which the Sun passes over the local meridian.

$$\alpha = \sin^{-1}(\sin \varphi \sin \delta + \cos \varphi \cos \delta \cos \omega) \quad (5.2)$$

$$\alpha_s = \sin^{-1} \left(\frac{\cos \delta \sin \omega}{\cos \alpha} \right) \quad (5.3)$$

Here, φ is the installation location latitude, ω is the hour angle, and δ is the declination angle. The hour angle describes the time of day in terms of degrees and the declination angle is the angle of deviation from the Sun being directly above the equator. The declination angle changes over the course of the year and can be found from Equation 5.4; while the hour angle changes throughout the day and is found using Equation 5.5:

$$\delta = 23.45^\circ \sin \left(\frac{360(n - 80)}{365} \right) \quad (5.4)$$

$$\omega = \frac{12 - T}{24} * 360^\circ \quad (5.5)$$

where n is the day of the year and T is the time of day on a 24-hour clock. Figure 5.2 is a depiction of each of these angles.

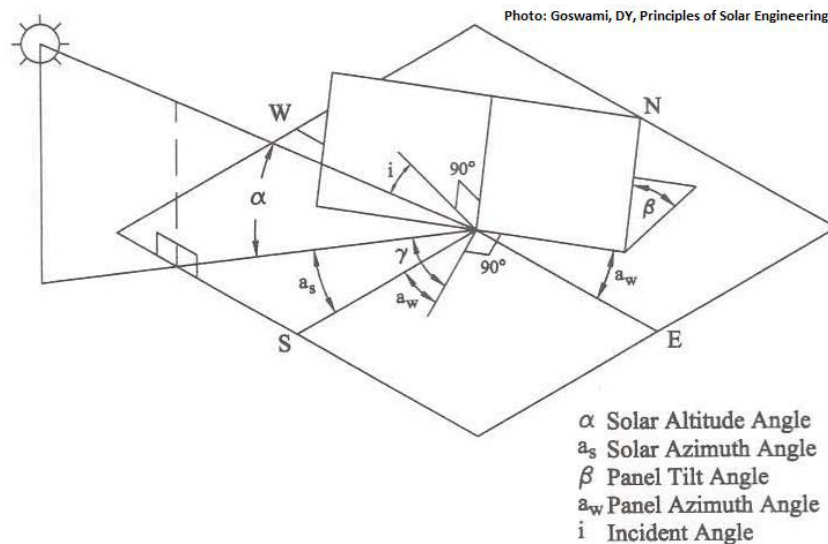


Figure 5.2. Angles of interest for solar panel power output (Goswami, Kreith, & Kreider, 2000).

5.2 REVIEW OF *DESIGN OF A SOLAR ENERGY HARVESTING SYSTEM FOR STRUCTURAL HEALTH MONITORING SYSTEMS*

5.2.1 Analytical Modeling and Experimentation

In order to analyze the optimal geometric orientation of the solar array, a simulation was created using the previously detailed relationships. First, the parameters were set using the values in Table 11. The climate data was taken from the NREL database for Austin, TX to simulate an average year's weather. A 50 W panel was selected for reference, but the results should be scalable to any size array. A charge controller using maximum power point tracking (MPPT) was included in the simulation to maximize the power delivered to the load. First, the optimal tilt angle was sought by setting the solar azimuth angle to 0°, or direct south. Figure 5.3 illustrates the results.

Table 5.1. PV Simulation Input Parameters (Inamdar, 2012).

Climate Data	Austin, TX (Camp Mabry TMY3)
PV Module	50W (BP 350J)
Tilt (degrees)	15 to 55
Solar Azimuth (degrees)	-45, -15 to +15, +45
Charge Controller	MPPT

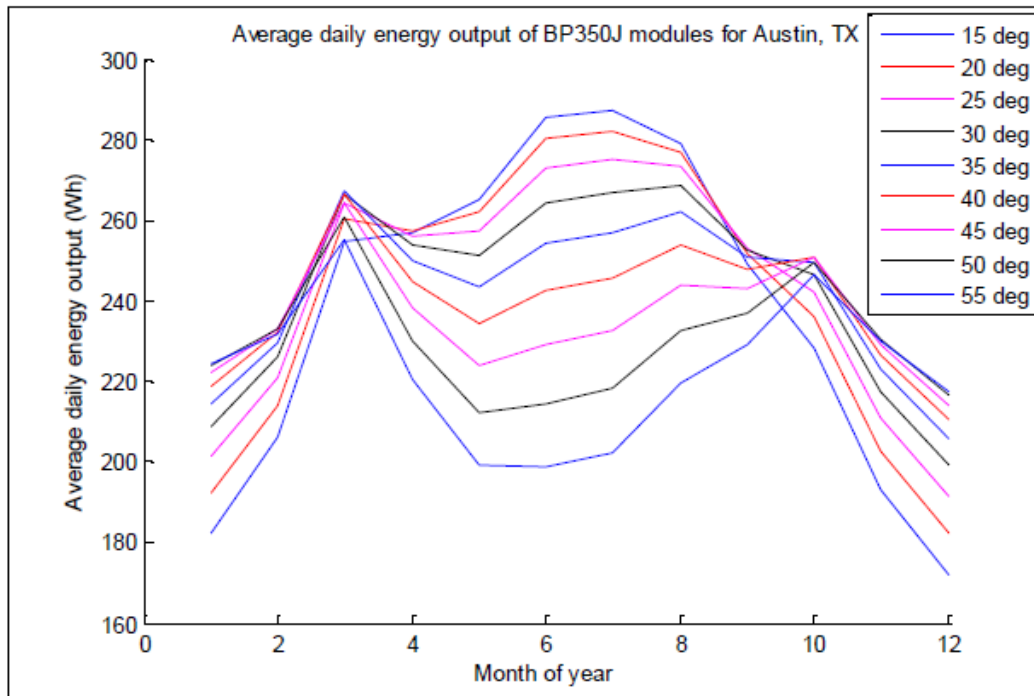


Figure 5.3. Average daily energy output for various tilt angles of a 50 W panel in Austin, TX (Inamdar, 2012).

The results indicate that the maximum power production occurs in the summer with lower tilt angles (such that the panel faces more towards the sky). However, in a year-long deployment, it is not necessarily ideal to generate the maximum power. Instead, it is desirable to find the angle that leads to the lowest minimal power output. This would be the limiting case and should be used to best find minimal output over the course of a year. The simulation indicates that a tilt angle of 45° will best serve to minimize the variability in energy production over a year. Next, the simulation was repeated with the tilt angle held at 45° to determine the optimal panel azimuth angle (Figure 5.4).

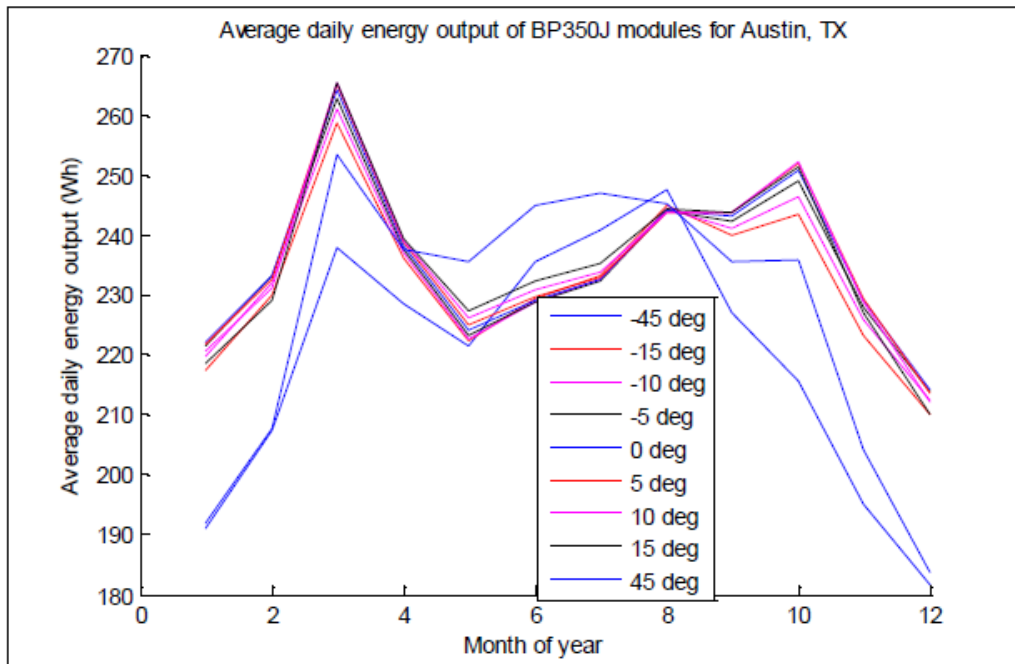


Figure 5.4. Average daily energy output for various azimuth angles of a 50 W panel in Austin, TX (Inamdar, 2012).

These results indicate that there is little difference in power production in the $+15^{\circ}$ to -15° range. In the end, the 0° angle, representing direct south, was found to allow the minimum energy production variability. From these results, it was decided that the optimal panel orientation for Austin, TX includes a 45° tilt facing direct south. Next, an analysis was performed to find the optimal solar panel and battery sizing for a static 14 W DC load, representative of the NI Gateway and cellular modem. This requires several factors to be weighed: (a) the cost of increasing/decreasing PV panel size, (b) the cost of the battery bank size, (c) the battery state of charge (SOC) and its impact on battery life, (d) the solar fraction (total energy provided by solar installation divided by the total energy required), and (e) the desired battery reserve with no solar input. The objective of the analysis was to find a battery/PV combination that minimized the overall cost while

maintaining a 100% solar fraction (such that the batteries are not being discharged over time). Table 12 contains the results.

Table 5.2. Results for Various PV and Battery System Configuration Simulations (Inamdar, 2012).

Rated PV Output (W)	Area (m ²)	Battery Size (Ah)	Annual Solar Fraction (%)	Average Battery SOC (%)	Total Cost (\$)	Annual Cost (10 yr)	Annual Cost (20 yr)
85	0.71	160	98.692	64.844	1790	179	137.5
85	0.71	200	99.138	65.599	2030	203	161.50
100	0.83	160	99.878	83.799	1828	182.80	139.40
100	0.83	200	100	84.981	2068	206.80	163.40
120	1.0	40	97.762	77.509	1167	116.70	70.35
120	1.0	80	99.782	86.162	1407	140.70	94.35
120	1.0	120	100	88.892	1647	164.70	118.35
120	1.0	160	100	89.233	1887	188.70	142.35
130	1.01	40	98.416	79.22	1185	118.50	71.25
130	1.01	80	99.849	87.324	1425	142.50	95.25
160	1.29	80	100	90.057	1502	150.2	99.1

With the criteria in mind, the 120 W PV panel with 120 Ah battery pack provides the lowest cost with 100% solar fraction. While the 160 W panel setup is actually slightly more cost-effective, the increase in area was ruled too great to be a valid option. The costs here are estimated based on the cost of the PV panel and batteries that must be replaced every 10 years. Battery life expectancy can be expected to exceed 10 years in

cases where the batteries are primarily discharged “shallowly”, or to less than 28% SOC (Inamdar, 2012). The PV panels are generally guaranteed for a life of at least 25 years. This setup should then meet the criteria set out by the initial project guidelines.

To help validate the numerical model, experimental testing was performed using several 50 W PV modules. The results of Figure 5.5 show that the analytical model outperforms the experimental results by nearly 38%. This can be accounted for in two ways. The analytical model uses weather data averaged from a 30 year timeframe as provided by the NREL database. This means it is likely to be less volatile than the real weather conditions. In addition, and perhaps more importantly, the simulation assumes a constant current draw, whereas the experimental setup utilized a static load resistance in the form of a resistor. As PV panels do not provide continuous current outputs, and instead follow an I-V curve, this means the load does not provide the optimal power output outside ideal conditions (i.e. 1000 W/m² insolation). The use of an MPPT charge controller would likely reduce the volatility of the experimental data, bringing it closer to the expected analytical results.

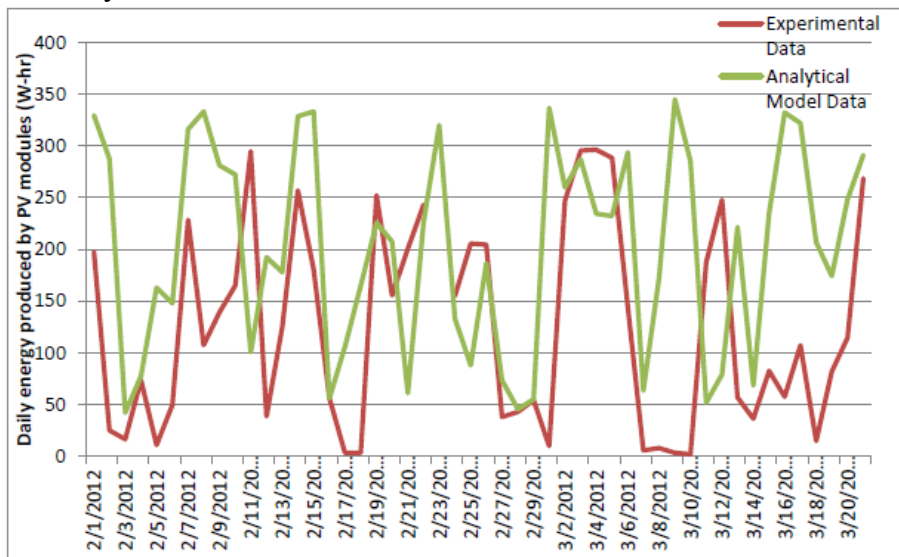


Figure 5.5. Comparison of daily energy production (Inamdar, 2012).

5.2.2 Design Embodiment

Based on the numerical simulation work, a concept was selected for embodiment. The components listed in Table 13 detail the final selections. As expected, the tilt angle was set at a fixed 45° position. The solar range allows mounting in any direction so that the panel can be positioned facing direct south. The selected PV panel, battery packs, and charge controller are listed for reference as well. The total package is fairly heavy at nearly 250 lbs, but this is largely due to a heavy duty mounting system composed of steel for structural strength. Figure 5.6 provides the solid model.

Table 5.3. Design Specifications for Selected Concept (Inamdar, 2012).

Design Feature	Specification
Tilt angle range	45°
Solar azimuth angle range	Any
Total package weight (panels, batteries, and all mechanical hardware)	248 lbs.
Pole Height	48 inches
Maximum system width (one end of panel to other end of panel with both $\alpha_s = 0^\circ$)	59 inches
PV panels	One Solarland 120W panels (SLP120-12U)
Battery bank	Three 12.8V 40Ah LiFePO ₄
Charge controller	Morningstar SunSaver MPPT
Supported load	14W constant DC

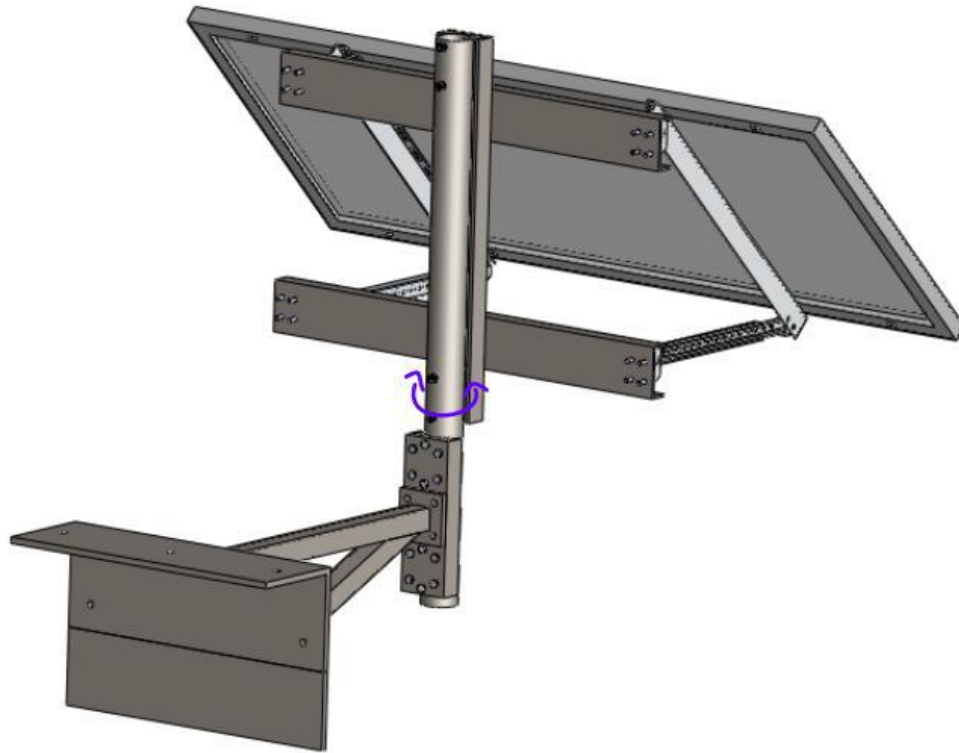


Figure 5.6. Solid model of selected concept (Inamdar, 2012).

To verify the selected mounting system is rugged enough to withstand the environmental conditions, mechanical analysis was performed using the FEA capabilities of SolidWorks Simulation. A sample of these results is included in Figures 5.7 and 5.8.

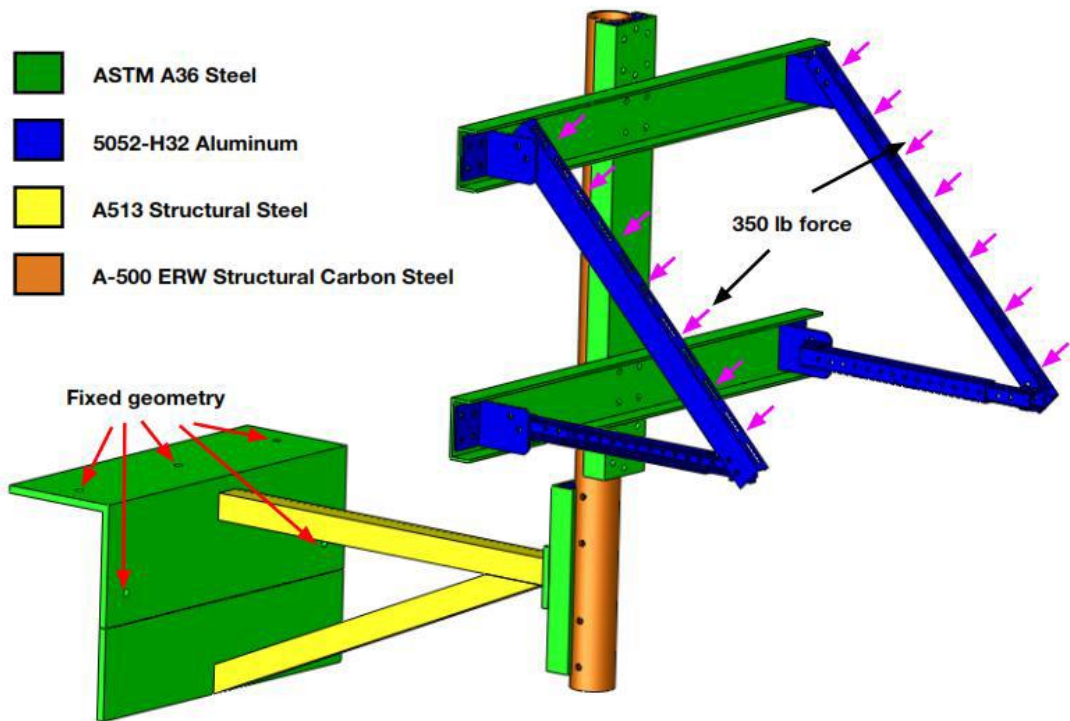


Figure 5.7. Color coded diagram of PV mount with part materials, fixtures, and forces listed (Inamdar, 2012).

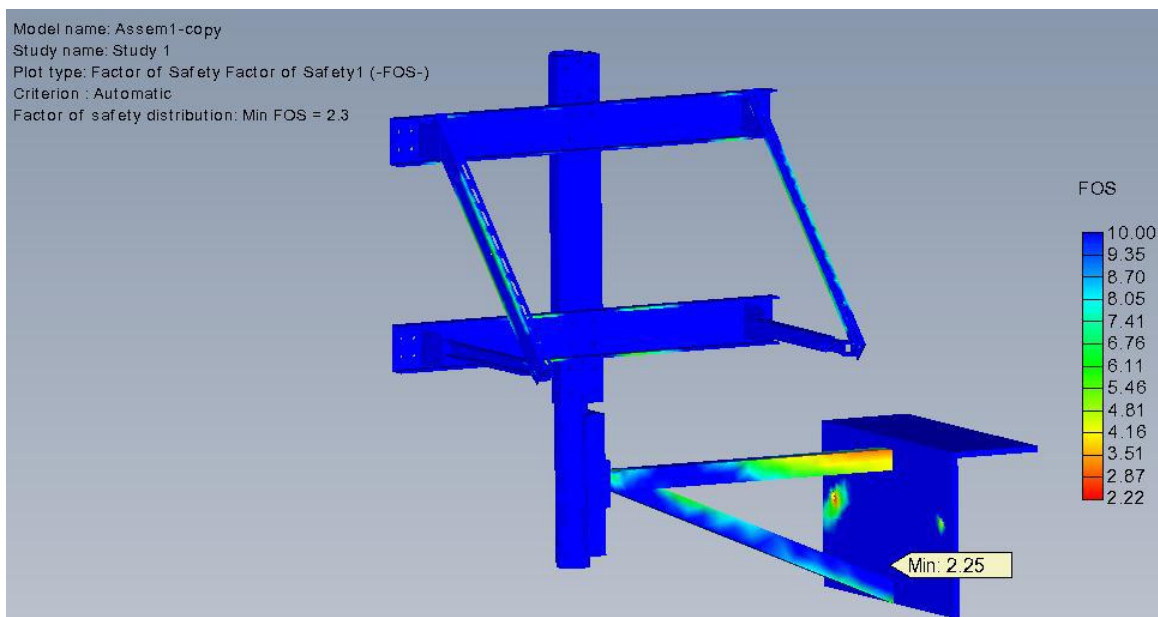


Figure 5.8. Sample FEA simulation results with factor of safety highlighted for panel in 90 degree configuration (Inamdar, 2012).

The FEA simulation was performed under a worst case condition with a 350 lb force corresponding to a 100 MPH wind gust. The results indicate that the factor of safety (FOS) is never lower than 2.2 for any configuration. The lowest FOS generally occurs around the anchoring points at the base of the attachment mechanism. While this should prove adequate, additional anchor points could be added with minimal overhead as desired.

5.3 SOLAR PROTOTYPE FIELD TESTING

5.3.1 Prototype Deployment

In order to test the proposed system, the prototype was assembled using the components and specifications from Table 13. The testing was carried out at the Pickle Research Campus (PRC) of The University of Texas at Austin. A concrete testing beam was selected to provide a realistic mounting location, such that the PV mount's installation difficulty and strength could be tested. The associated electronics were mounted in a weather-proof enclosure for protection from the elements. This enclosure is designed to be attached to the mounting pole; however, for this testing it was left free for easy access. Figures 5.9 and 5.10 provide views of the completed setup, while Figure 5.11 shows the internals of the enclosure.



Figure 5.9. Front view of PV panel, mount, and enclosure.



Figure 5.10. Rear view of PV panel, mount, and enclosure.

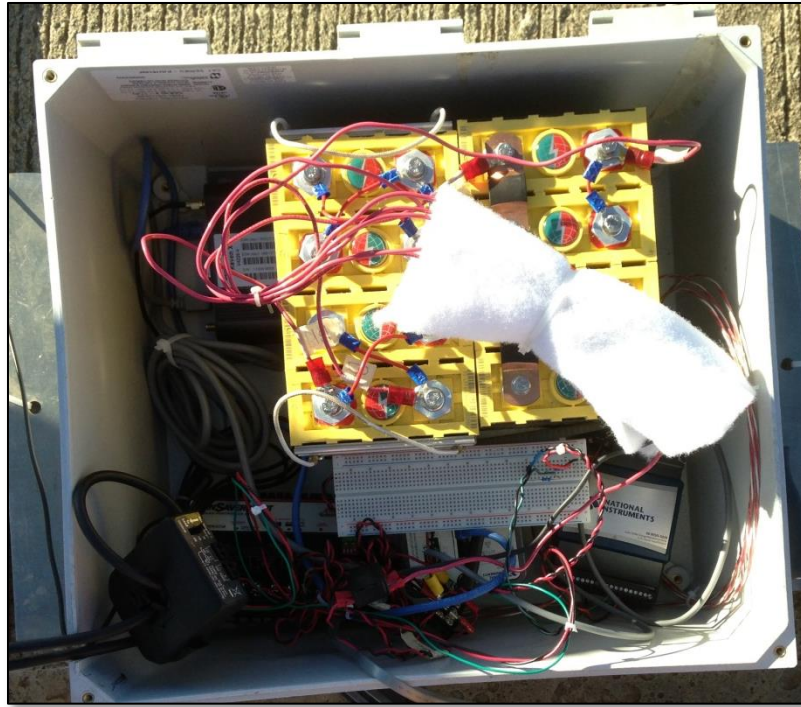


Figure 5.11. Internal view of the enclosure with associated electronics.

The panel mount was attached to the concrete beam using concrete anchors in the pre-drilled holes on the beam. During installation it was found that one of the concrete anchors was “stripped”, leaving it lodged in the hole and not easily removable. As this was only for testing, it was determined acceptable; however, in a final production prototype it is suggested that additional mount points be included as a contingency. Additionally, concrete is laced with rebar that can be difficult to locate before drilling. Redundant anchor points provide some robustness in the event of such difficulties during mounting.

The system was installed by a two-person team as the components were quite heavy. Before installation, the system was partially assembled into two major components, the PV panel and pole and the 90° angled mount and arm, in the lab. If

installation by an individual were required, leaving this assembly to be completed throughout the mounting process would drastically reduce the weight of the individual components. Due to the preassembly, the PV panel was mounted approximately 10° west of direct south. While this is not optimal, the results in Figure 5.4 indicate that this panel azimuth angle should have a minimal impact on performance.

In order to simulate a realistic load, the enclosure contained a number of electronics capable of logging the system's performance. These components included:

- Morningstar SunSaver MPPT Charge Controller
- NI 9792 Programmable WSN Gateway
- NI WSN-3226 Voltage/RTD Combination Node
- Sierra Wireless Airlink Raven X 3G Modem
- 3-Wire Resistance Thermometer (RTD)
- Veris Hawkeye 970HCA DC Current Transducer
- 12.8 V 40 Ah LiFePO₄ Battery Pack

The NI WSN node was programmed to record measurements at 30 minute intervals for the temperature, panel voltage, and current. The temperature was recorded inside the enclosure using the RTD to ensure the electronics were within their safe operating ranges. The power provided by the PV panel was measured using the product of the current and voltage. The voltage from the panel was outside the nominal range of the node, so a simple voltage divider circuit was used. One lead from the PV panel was wrapped through the current transducer several times to increase the sensitivity before being logged by the node. Only one battery pack was included to reduce cost and size.

The node was configured to upload the captured data to the gateway at the same 30 minute interval to maximize power draw. The gateway acted as the data storage repository and was connected to the Raven X modem to allow remote access to the

system and provide real-time data on-demand. This also allowed connectivity to the system to provide programming changes, such as increasing/decreasing the sampling rate and remote rebooting of the gateway/node. In addition to these sensors, the charge controller has several onboard logging capabilities that were monitored, including monitoring the charge state of the batteries and power draw from the load.

5.3.2 Field Testing Results

The testing was carried out from January to March 2013. Over that time period, the system remained operational with no downtime from lack of available energy. The listed safe operating temperature range for the electronics was -22°F to 140°F . To ensure the components did not overheat, an analysis was performed comparing the temperatures in the enclosure to those of the ambient air in the area. A three day span is provided in Figure 5.12.

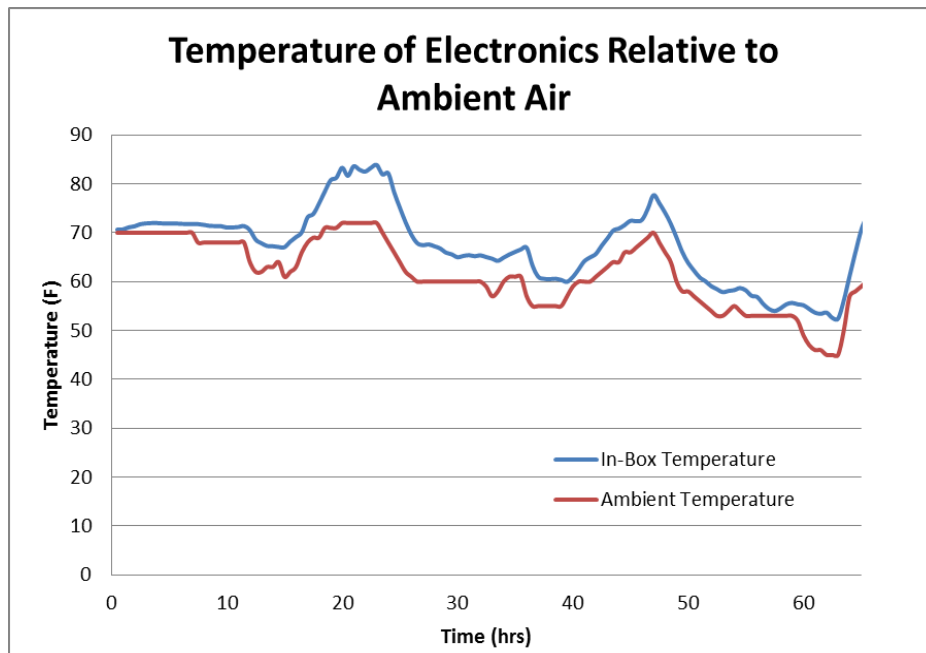


Figure 5.12. Comparison of enclosure temperature to ambient air.

The results show that the internal enclosure temperatures track 5° to 12° warmer than ambient consistently. In general, this pattern indicates safe temperatures for the electronics in all but the most extreme climates. As the ambient temperatures did not exceed 100° F during the testing period, the resulting enclosure temperatures remained in the safe operating range for the equipment. The PV power delivered to the charge controller was calculated using the voltage and current measurements. A two-week sample of power data from the end of the testing period is provided in Figure 5.13.

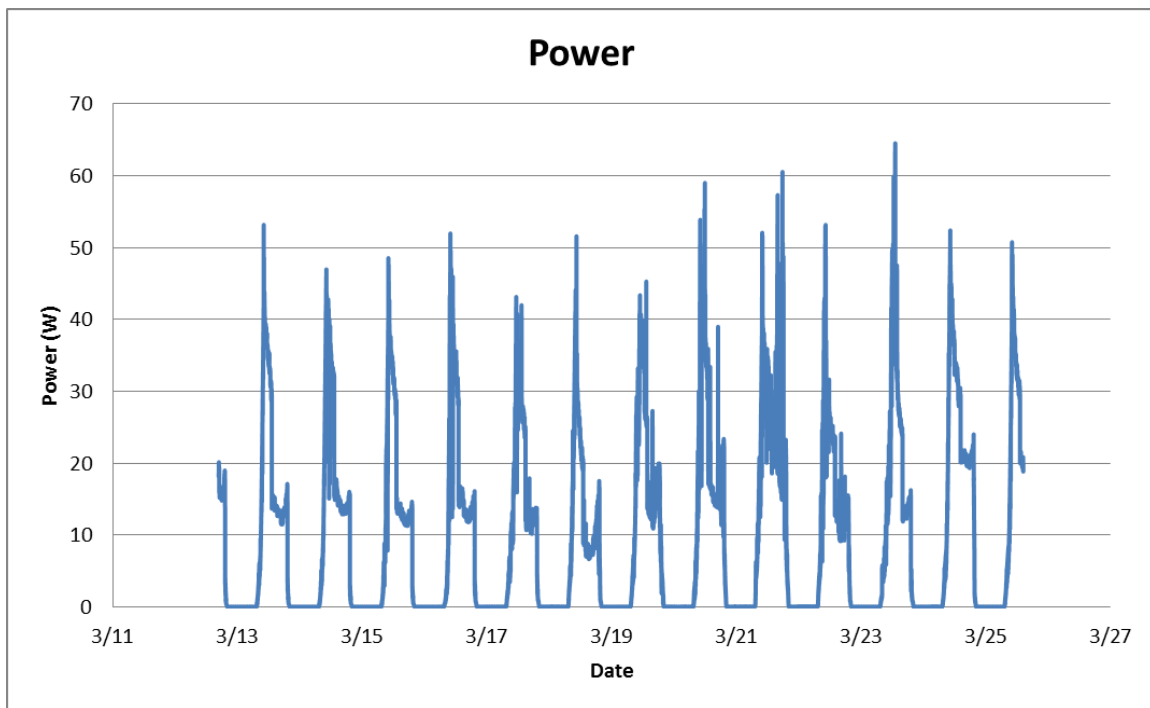


Figure 5.13. Solar harvester power data from two weeks of testing.

On first inspection, it appears the panel is far from reaching its potential generation capabilities. However, this is not unexpected for a system operating as anticipated. In a system that requires relatively little battery charging, the panel will only produce as much power as can be absorbed by the attached load. In this case, this means

the expected PV panel output should reach a maximum during battery charging and quickly drop to the load requirements as the batteries are fully recharged. This is more easily illustrated by looking at a single day's power output (Figure 5.14).

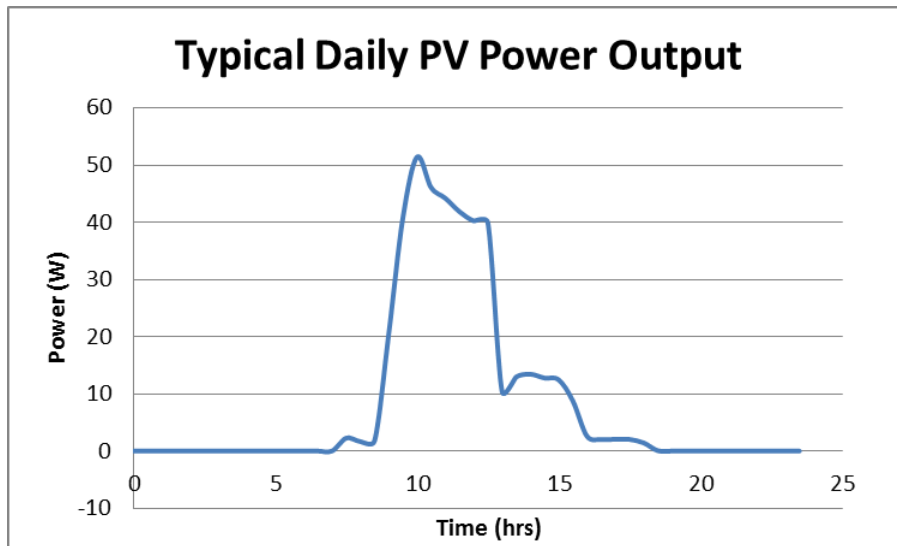


Figure 5.14. Typical daily PV power output for 24 hour period in January.

As indicated, the peak power output occurs early in the day. This is likely a function of the charge controller and the internal charging algorithm used for Li-ion type batteries. In general, Li-ion batteries are charged using a methodology that first brings the cell voltage to the desired level, then maintaining this voltage, reduces the current as saturation is reached. After this point, the battery is only “topped” on occasion to remain fully charged. Therefore, it is likely that in a battery that is only lightly drained (such as a single night of usage in this experimental setup), the power delivered to the battery will be throttled due to this charging algorithm and only continue to drop until completely cut at a full charge. This seems to follow the results of hours 9-12 in Figure 5.14. After this point, it is assumed the only load experienced by the panel is the monitoring electronics

and the power draw from the PV panel is reduced to the expected 12-14 W DC load.

Figure 5.15 demonstrates the expected charging algorithm for a Li-ion battery.

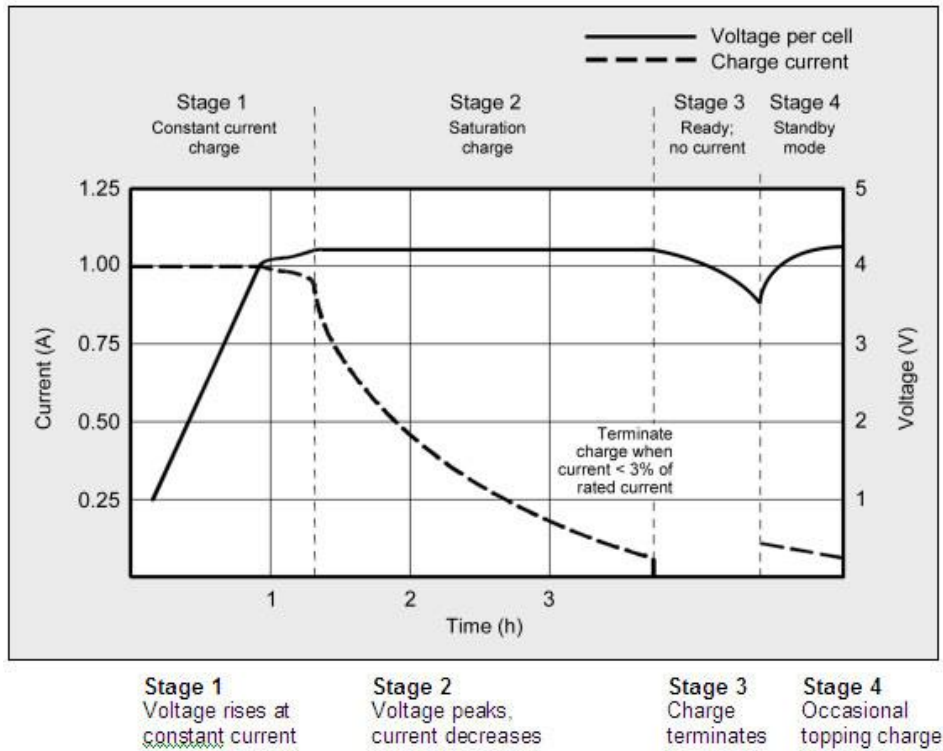


Figure 5.15. Representative charging break-down for Li-ion batteries (Battery University, 2014).

Long term data logging was performed by the SunSaver MPPT charge controller. The daily charge delivered by the PV panel and daily load delivered to the attached electronics are illustrated in Figure 5.16. As expected, the daily load is fairly consistent and fluctuates minimally throughout the process. The increase in power draw during the final 20 days is indicative of the increase in sampling rate (from 30 minutes per sample to 2 minutes per sample) used to test the system response to the increased demand.

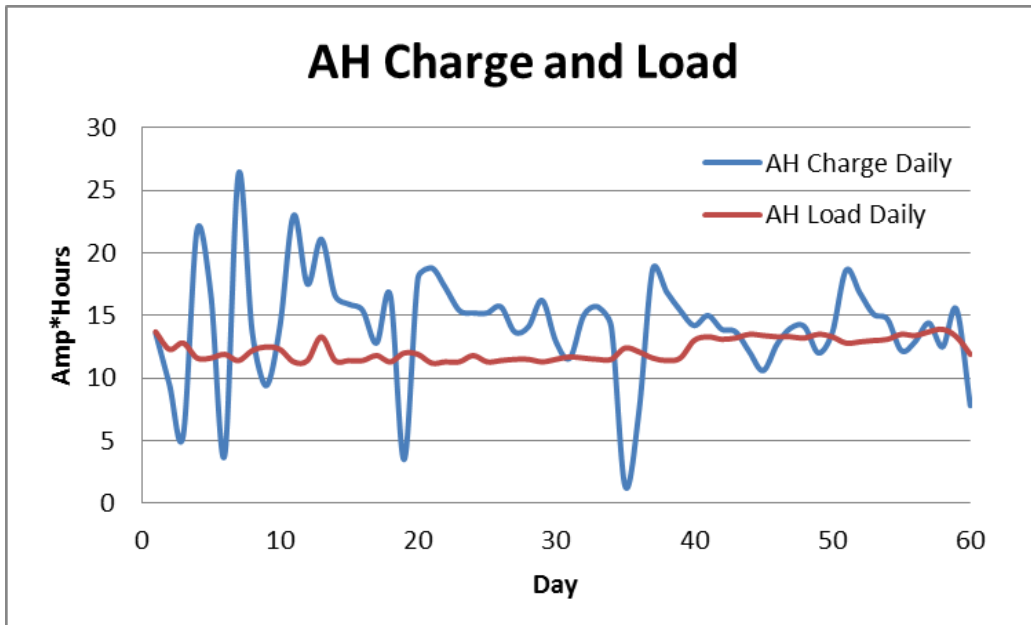


Figure 5.16. Daily Ah charge and load over 60 days of data acquisition.

Conversely, there is considerable fluctuation in the daily charge delivered. This illustrates several key points. In days following a particularly low charge output, the next day tends to have a corresponding increase to fully recharge the battery. This likely means the system is not taxed during periods of good weather, as would be expected from the power results in Figures 5.13 and 5.14. In addition, as long as the battery is capable of powering the system during sustained poor weather days, it should easily recharge the system as the weather improves. Additionally, during all 60 days that were monitored, the PV always generated some power and there were no extended periods of very low output. This is because the cloud cover does not reduce the insolation below the panel’s threshold even during the worst cases. Table 14 showcases this by comparing the charge, load, and corresponding cloud cover percentages for the first week of data (where the greatest volatility was seen).

Table 5.4. Daily Charge Controller Charge/Load Amp-Hours with Corresponding Cloud Cover Percentage.

Date	Charge Amp-hours	Load Amp-hours	Cloud Cover (%)
1/10/2013	13.6	13.7	50
1/11/2013	9.5	12.3	45
1/12/2013	5.4	12.8	85
1/13/2013	21.8	11.6	30
1/14/2013	16.7	11.6	50
1/15/2013	3.8	11.9	95
1/16/2013	26.3	11.4	0
Totals	97.1	85.3	

5.4 SOLAR HARVESTER CONCLUSIONS

The results from the field testing are promising for the long-term viability of using a solar array to power the gateway component of a bridge-health monitoring WSN. The proposed prototype was capable of powering a load representative of the gateway component with no outages for more than two months of uptime. Additionally, it appears the system is capable of quickly recharging a depleted battery after periods of low insolation once normal insolation levels are restored. With the proposed 120 Ah battery packs, the system should be capable of powering the system with no solar input for 8-10 days. However, during the 60 day testing period, zero days saw no power input from the PV panel and only 6 saw energy outputs lower than the energy delivered to the load. Therefore, it is likely the system proposed by Inamdar and tested in this work is capable of adequately powering the gateway component of the WSN under most conditions.

Chapter 6: Conclusions and Future Work

6.1 SUMMARY AND CONCLUSIONS

In the wake of two major highway bridge collapses and a statistically aging transportation infrastructure any method to efficiently and economically monitor the status of these critical structures must be considered. This thesis presented components of the efforts of NIST-TIP's project entitled, "Development of Rapid, Reliable, and Economical Methods for Inspection and Monitoring of Highway Bridges". Much of this project's focus was on developing a method to implement a wireless network system for structural health monitoring of fracture-critical bridges. Wireless network systems present a technologically viable way to effectively monitor large structures without the excessive costs associated with adding networking cable systems. The work in this thesis focused on overcoming one major obstacle in this process – powering the critical components in these WSN's.

The selected National Instruments WSN system has three primary components, each with different power requirements. This work looked at two potential energy harvesting technologies that could be used to power the lowest and highest consumption WSN components, the node and gateway, respectively. First, the use of traffic-induced bridge vibrations was explored for implementing a linear, electromagnetic harvester that might power the individual nodes. Vibrational harvesters have shown great promise in cases with consistent higher frequency sinusoidal excitations, but the usage of vibrational harvesters for aperiodic, low frequency (<10 Hz), low amplitude oscillations seen in most bridges has had minimal study. The primary advantage of a vibration-based energy harvester, as opposed to more common wind and solar energy harvesting devices, is the ability to completely seal the device from interaction with the elements. This means less device deviation over time and should result in less wear and tear. The second energy

harvesting technology explored was the use of solar photovoltaic (PV) arrays for providing power to the gateway component. The gateway is the critical data aggregating component of the WSN and requires more than an order of magnitude more power than the node (~14 W vs 0.5 W). As solar has an order of magnitude more energy production potential than either wind or vibrational sources, it is the logical choice for the largest power draw component. Additionally, photovoltaic arrays are a reasonably mature technology that is highly scalable depending on the system requirements.

To introduce the vibrational energy harvester, a critical review of relevant literature was discussed. This first included a general overview of the techniques used to harvest vibrational energy, including electrostatic, piezoelectric, and electromagnetic harvesters. Electromagnetic harvesters are generally preferred in low frequency applications as the impedance of these systems is directly proportional to frequency (as opposed to inversely proportional as seen in electrostatic and piezoelectric). So, a further review was conducted on low frequency electromagnetic harvesters found in the literature. It was found that two primary applications exist for such devices, harnessing energy from human body motion and previous studies into bridge vibrations. Reviewing designs from these two categories in literature reveals numerous designs with a few key consistencies. In general, the compliant member varied from linear springs to a flexible hinge system to non-linear magnet springs. Each has distinct advantages and disadvantages based on manufacturability, cost, and efficiency. The most important consistently seen design feature was the use of an oscillating mass made up of axially magnetized permanent magnet disks with iron flux concentrators placed between opposing poles. This creates a tubular, axisymmetric design that was shown to optimize the flux linkage with the surrounding copper coils.

As this thesis was the terminal work from the NIST-TIP project, several other works were seen to study similar energy harvesting systems. Two, the works by Reichenbach (2012) and Dierks (2011), were reviewed to provide background information and carry forward relevant concepts. Reichenbach (2012) served as a feasibility study in general vibrational energy harvesting as it relates to bridges. Dierks (2011) focused on developing a vibrational energy harvester for bridge applications and evaluating the critical parameters.

The work by Reichenbach provides background information into the methodologies used to instrument bridges and quantitatively evaluate their ability to support a vibrational energy harvester. Using spectral analysis of accelerometer data taken from a sample of representative bridges it was found that the frequency of vibration can greatly vary among bridges based on structure type, age, and temperature. Additionally, the amplitudes of these vibrations show similar discrepancies not only between bridges but between mounting locations on a single bridge. As the excitation frequency and amplitude are critical to harvester power output, these factors must be evaluated for any potential mounting location. Reichenbach concluded that a harvester must be capable of adapting to the slow changes in excitation frequency seen during aging and temperature shifts for effective long-term deployment. Finally, using numerical simulations, estimations concluded that only three of five instrumented bridges showed any promise for supporting vibrational energy harvesters; however, these three also corresponded to the most deserving candidates for a bridge health monitoring system. Using the same numerical models, a general recommendation was provided for a 0.1 damping ratio as a reasonable trade-off between peak power output and bandwidth.

The work by Dierks used a combination of simulation and experimental validation to evaluate potential harvester designs. The simulation work demonstrated that

tuning a potential harvester to the excitation frequency is critical for optimal power output. Additionally, tuning the load resistance for the purpose of impedance matching was necessary to maximize power output. By implementing captured accelerometer data into the numerical simulation work, it was found that the majority of the energy delivered to the load occurred in short bursts following large amplitude oscillation events, not gradually over time. Perhaps the most important concept studied by Dierks was the potential differences in linear and non-linear springs. These efforts concluded that linear springs outperformed non-linear springs by a factor of 100 in simulation work and consistently outperformed non-linear springs in similar experimental work. Additionally, a mounting methodology was developed that shows promise for the high variability seen in bridge superstructures.

This work then expanded upon these studies by developing numerical and FEA simulations in order to explore the potential harvester parameterization and predict performance. These studies indicated a strong dependence on the selected resonant frequency and damping values for harvester performance, consistent with previous studies. Numerical simulations indicate relatively small discrepancies between desired natural frequencies and the excitation source resonant frequencies have drastic implications on power production. Using larger damping factors, such as those suggested by Reichenbach, does result in harvesters with wider bandwidths; however, increasing the harvester damping also results in significant decreases in power output. A cross-over point exists such that the increased bandwidth provides a net increase in power potential for a given deployment location over time (as bridges frequencies experience the natural fluctuations). However, identification of this point requires significant analysis using acceleration data for each potential deployment location.

A topology was selected for experimental validation using the results from the numerical simulations, a developed electromagnetic finite element model, and comparable devices found in the literature. Using precision machining techniques and non-magnetic materials, a simple tubular, modular, stacking experimental prototype was fabricated. Laboratory testing was conducted using an electromagnetic shaker table and hardware and software from National Instruments. These results fell short of the 0.5 mW desired output under replicated bridge excitations. Parameterization of the prototype revealed the electrical damping coefficient to be significantly lower than desired, likely resulting in the reduced power output. Applying the prototype parameters in the numerical simulation produced performance results consistent with the experimental testing.

Exploration of solar harvesting technologies began with a review of modern photovoltaic technology. Then, a review of previous team member Inamdar's (2012) research was presented. Using numerical simulation work, Inamdar found that setting a PV panel at 0° (facing direct south) and tilted to 45° was optimal for maximizing the lowest energy production in Austin, TX. For multi-year deployments, this method of designing for the limiting case is best to ensure adequate year-round charging capacity in a solar module harvester. Next, a simulation was performed to properly evaluate the ideal PV panel and battery bank size that would incur minimal total cost in a ten year deployment. With this information a prototype was proposed and initial components were acquired. Finally, a mounting methodology relying on concrete anchors was developed and numerically validated for structural integrity using finite element analysis tools.

This thesis then focused on completing fabrication and field testing of the proposed prototype. A location was selected in Austin, TX that replicated potential bridge mounting conditions, and the prototype was deployed with an array of electronics that

allowed for performance logging while simulating a real-world electrical load. The field testing conducted focused on monitoring the temperatures the electronic components experienced, the power produced by the PV panel, and the charge delivered to the battery bank. Temperature testing revealed the internal electronics enclosure temperatures tracked between 5° F and 12° F above ambient air; given the operating ranges of the proposed electronics, this is safe for all but the most extreme environmental conditions. The prototype was deployed for more than two months with no downtime due to lack of energy. Analysis of the power output from the panel and charge delivered to the battery indicates behavior consistent with a properly charging Li-ion battery and minimally taxed PV panel. Overall, this system is capable of 8-10 days of uninterrupted operation during worst-case insolation conditions and will quickly recharge the battery pack once normal insolation levels are restored. This provides a robust system that should be capable of meeting the 14 W goal outlined by the NIST-TIP project.

6.2 FUTURE WORK

Future work for the vibrational harvester should focus on three main objectives: (1) optimizing the geometric parameters of the system, (2) development of a finalized energy storage circuit, and (3) integration with the proposed mounting system. Optimizing the harvester geometries should follow an approach similar to that described by von Buren & Troster (2007). Using a combination of an analytical model and electromagnetic finite element analysis software, an optimization should be performed to find dimensions that match the desired damping. Ideally, this would be performed using discrete sizes for the magnet components that match those found in the marketplace, to make fabrication possible. This could be performed using a genetic algorithm or simulated annealing, similar to the original work by von Buren and Troster.

As any final design must transform the AC output to a usable DC voltage for storage and use by the load, the circuitry should be investigated. A simple circuit might incorporate a Schottky diode full-wave rectifier (to minimize the voltage drop across the diode), a DC-DC voltage regulator, and a Li-ion battery for storage. Additionally, a charge controller should be included for the Li-ion battery to ensure long-term durability; however, batteries can be found that include this circuitry on-board the unit. A refined version might include the addition of a tantalum capacitor or explore replacing the Li-ion battery with a supercapacitor to increase efficiency.

Finally, conversion of the laboratory testing prototype to a model ready for field testing should involve the implementation of the mounting methodology described by Dierks (2011) in the beta prototype. Testing should validate the mounting mechanism's robustness in multiple bridge structures, test harvester performance under real-world excitations, and evaluate an electrical circuit design. With this information, the team should be able to better examine the long-term viability of an electromagnetic harvester excited by bridge oscillations.

Future work on the solar prototype should be minimal, focusing on examining any potential cost-savings using the newest solar panels and battery technologies. A market-ready electronics housing was developed by National Instruments that matches closely with that used by the field tested prototyped and should be explored. The addition of redundant concrete anchor points in the panel mount should be considered for contingency. Finally, the system can be deployed in an actual bridge health monitoring application for full validation.

Appendix A: Bill of Materials

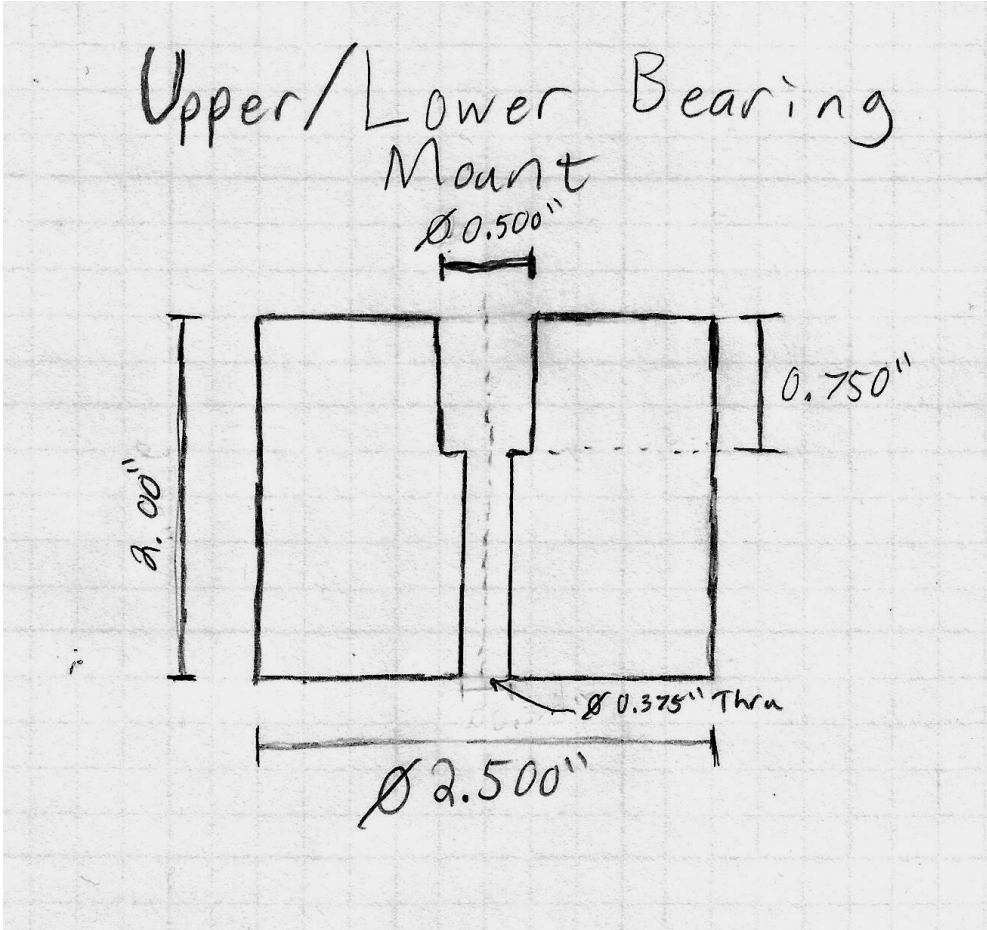
#	Part Name	Description	Supplier	Part No.	Qty.
1	Outer Housing	Optically Clear Cast Acrylic Tube, 3" OD x 2-1/2" ID, 3' Length	Mcmaster.com	8486K555	1
2	Top/Bottom End Cap	2-1/2" Dia. Round Bar 6061-T6 Aluminum	Metalsdepot.com	R3212	1 ft
3	Spring Spacer	2-1/2" OD x .375" wall x 1.75" ID 6061 Aluminum Round Tube	Metalsdepot.com	T3R21238	1 ft
4	Upper/Lower Bearing Mount	2-1/2" Dia. Round Bar 6061-T6 Aluminum	Metalsdepot.com	R3212	1 ft
5	Upper/Lower Stator Mount	White Delrin Acetal Resin Rod 2-1/2" Diameter, 1 Ft. Length	Mcmaster.com	8572K32	1
6	Coil Stator	White Delrin (r) Acetal Resin Tube, 2" OD x 1- 1/2" ID, 1' Length	Mcmaster.com	8627K889	1
7	AWG 30 Magnet Wire	Motor Winding Wire, 30 Gauge, 6000 Ft Spool	Mcmaster.com	7588K51	1
8	Mounting Plate	.500" (1/2") thick 6061- T651 Aluminum Plate, 12" x 12"	Metalsdepot.com	P312T6	1

9	Center Mount Socket Screw	Type 316 Stainless Steel Socket Head Cap Screw, 1/4"-20 Thread, 2-1/2" Length	Mcmaster.com	92185A555	1
10	Mounting Plate Screws	Type 316 Stainless Steel Pan Head Phillips Machine Screw, 1/4"-20 Thread, 1-1/2" Length	Mcmaster.com	91735A546	4
11	Housing Mount Socket Screws	Type 316 Stainless Steel Socket Head Cap Screw, 1/4"-20 Thread, 1" Length	Mcmaster.com	92185A542	6
12	Housing Mount Washers	Type 316 Stainless Steel Flat Washer, 1/4" Screw Size, 0.281" ID, 0.625" OD	Mcmaster.com	90107A029	6
13	Threaded Rod	Aluminum Fully Threaded Rod, 1/4"-20 Thread, 1 Foot Long	Mcmaster.com	94435A313	1
14	Nuts for Threaded Rod	Type 316 Stainless Steel Hex Nut, 1/4"-20 Thread Size, 7/16" Wide, 7/32" High	Mcmaster.com	94804A029	2

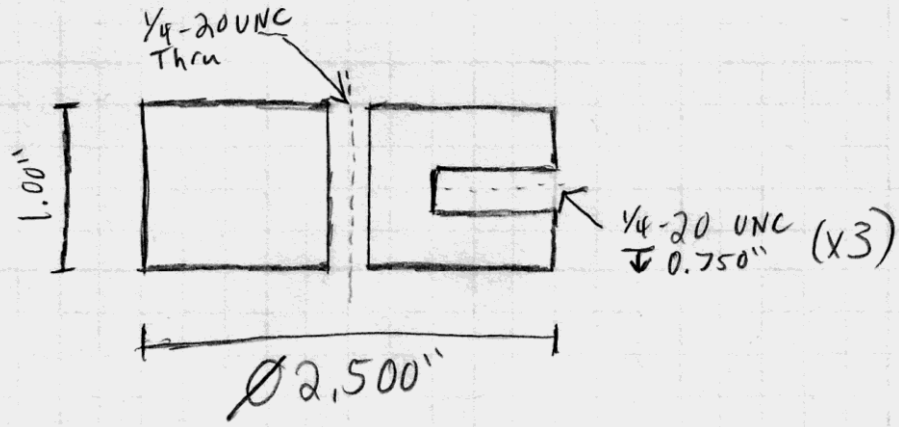
15	Washers for Threaded Rod	Type 316 Stainless Steel Flat Washer, 1/4" Screw Size, 0.281" ID, 0.625" OD	Mcmaster.com	90107A029	2
16	Helical Extension Spring	Extension Spring, 0.359" OD, 1.750" Length, 1.000 lb/in, Material: Music Wire	Centuryspring.com	80451	1
17	Linear Shaft	Precision Anodized Aluminum Shaft, 1/4" Diameter, 12" Length	Mcmaster.com	5911K21	1
18	Axial Magnets	N48 NdFeB, 1 1/2" OD x 1/4" ID x 1/2" Thick, Nickel Plated, Axially Magnetized	Kjmagetics.com	N/A	12
19	Core Iron Poles	VIM VAR Core Iron 1.5" Diameter Rod	Edfagan.com	N/A	6"
20	Shaft Couplers	Aluminum Set Screw Rigid Shaft Coupling, Without Keyway For 1/4" Diameter Shaft	Mcmaster.com	242K11	2

21	Linear Bearings	Steel Fixed-Alignment Linear Ball Bearing, Closed, for 1/4" Shaft Diameter, 3/4" Overall Length	Mcmaster.com	60595K11	2
-----------	-----------------	---	--------------	----------	---

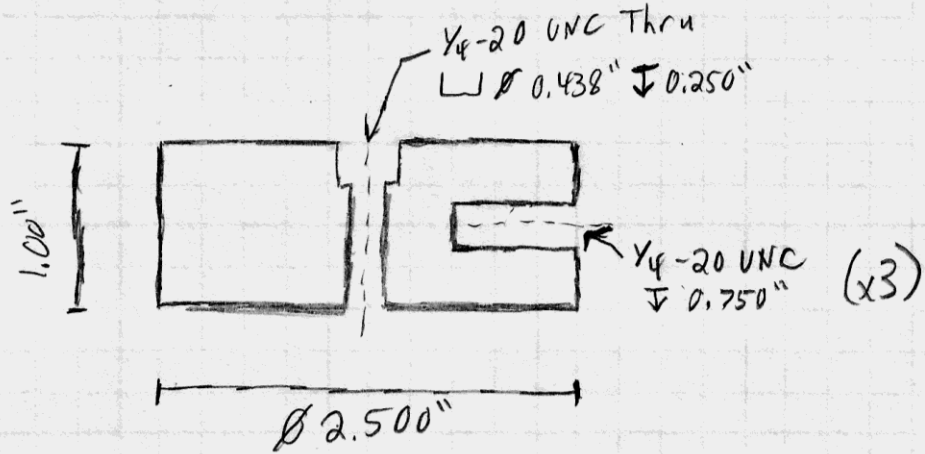
**Appendix B: Dimensioned Cross-Sectional View Sketches for Selected
Vibrational Harvester Components**



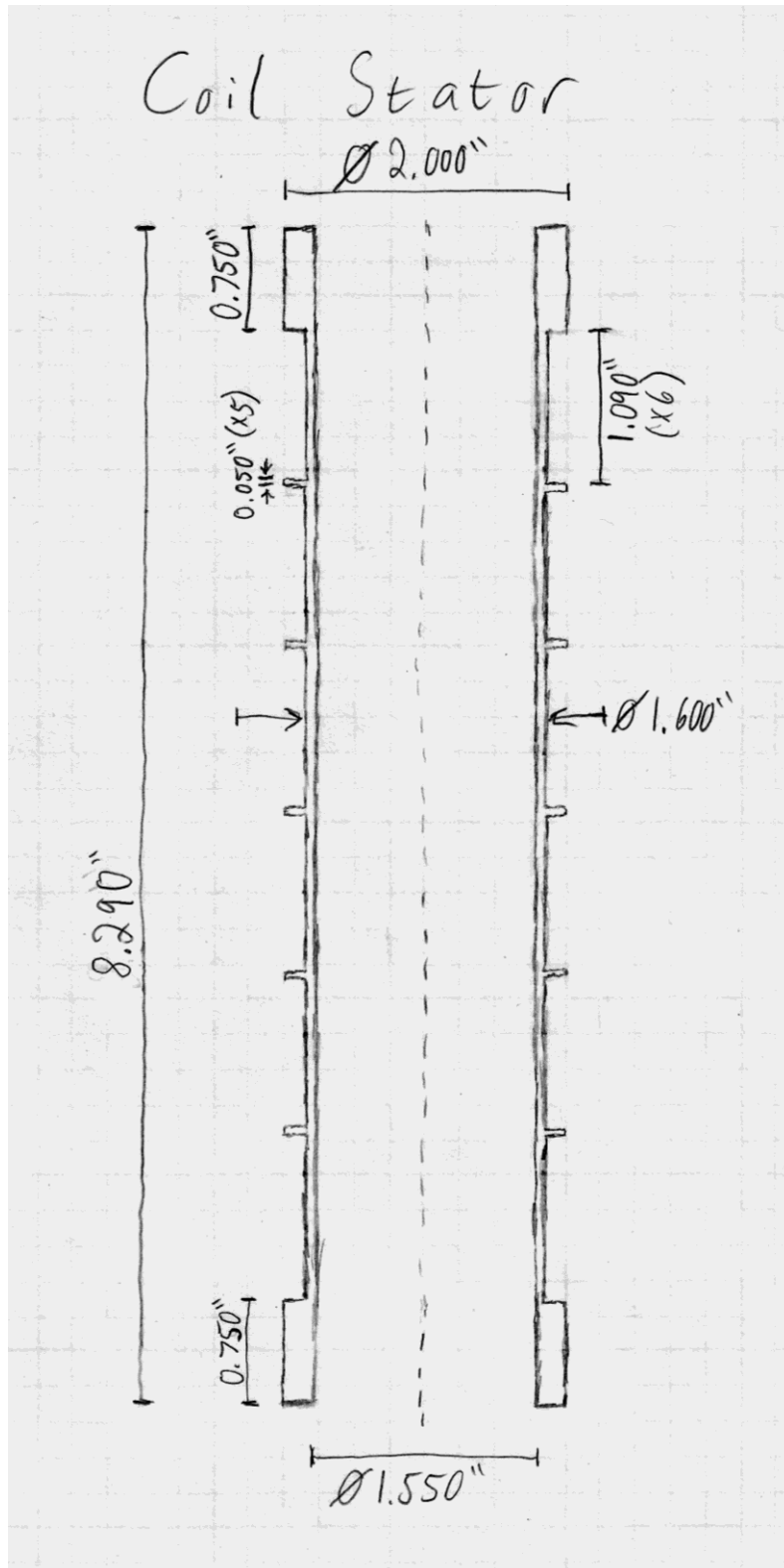
Top End Cap



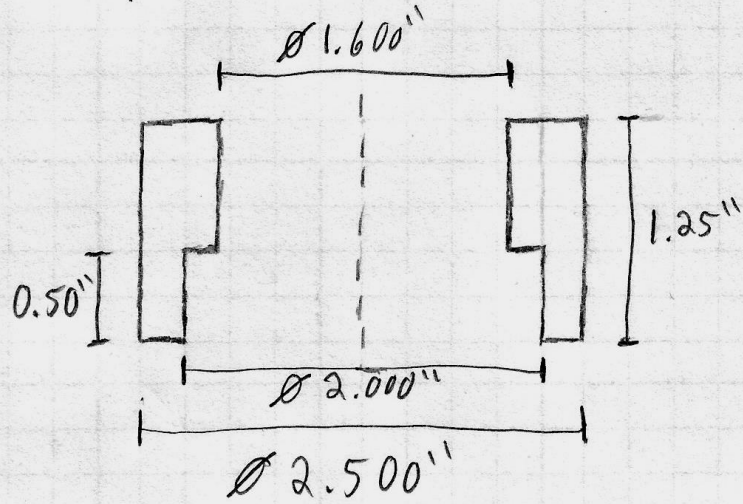
Bottom End Cap



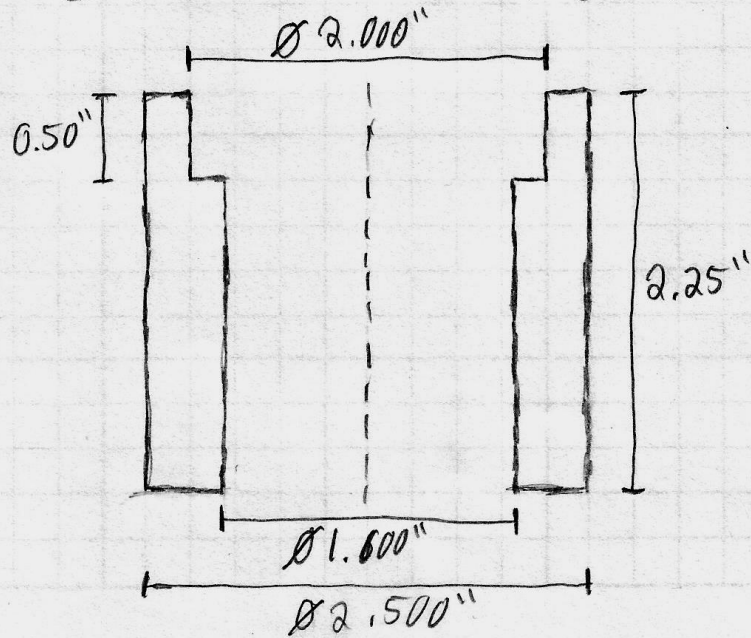
Coil Stator



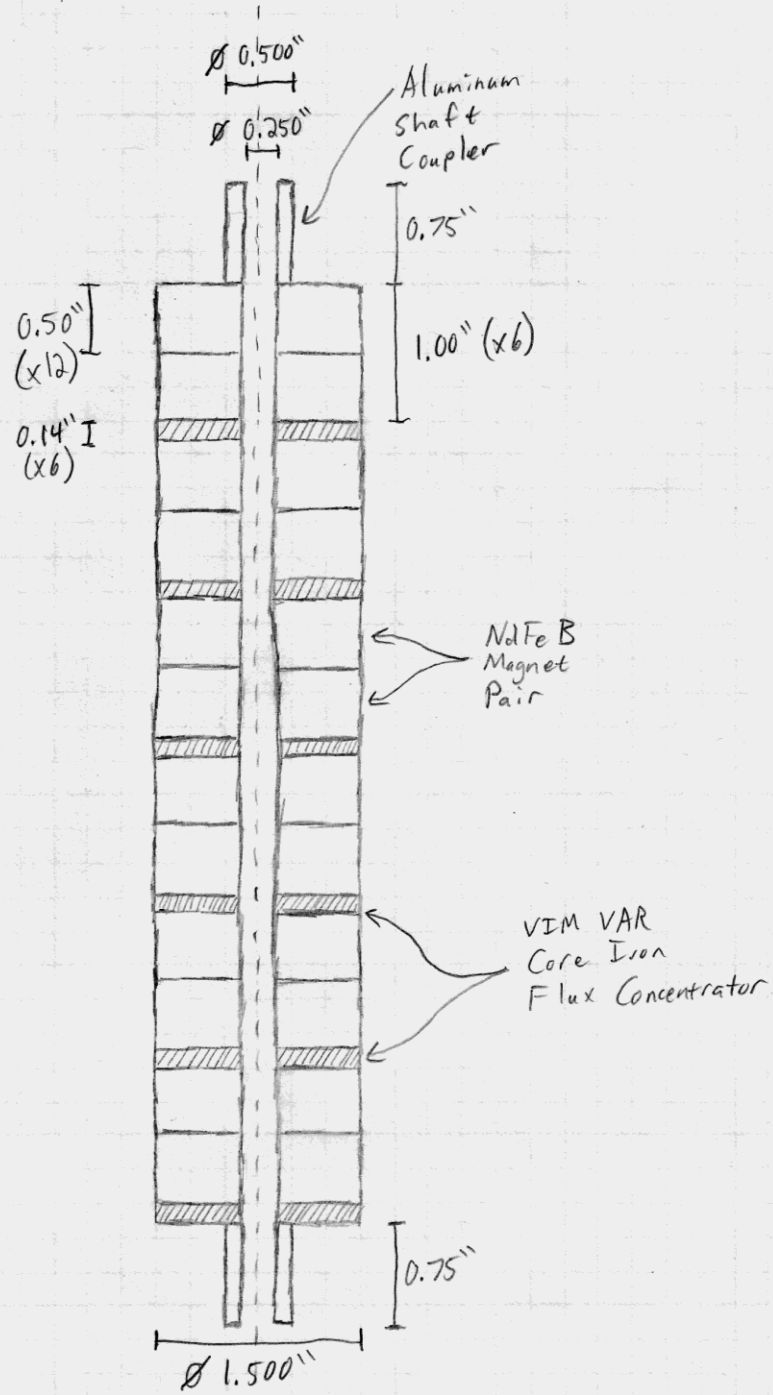
Upper Stator Mount



Lower Stator Mount



Translating Mass Assembly



Bibliography

- Battery University. (2014). *BU-409: Charging Lithium-ion*. Retrieved from Battery University:
http://batteryuniversity.com/learn/article/charging_lithium_ion_batteries
- Bello, M. (2013, May 24). *Bridge collapse shines light on aging infrastructure*. Retrieved from USA Today:
<http://www.usatoday.com/story/news/nation/2013/05/24/washington-bridge-collapse-nations-bridges-deficient/2358419/>
- Dierks, E. (2011). *Design of an Electromagnetic Vibration Energy Harvester for Structural Health Monitoring of Bridges Employing Wireless Sensor Networks*. Master's thesis. University of Texas at Austin, TX.
- Dunlap, B. (2014). *Active Learning Module Assessment and The Development and Testing of a New Prototyping Planning Tool*. Master's thesis. University of Texas at Austin, TX.
- Federal Highway Administration. (2012). *Annual Vehicle - Miles of Travel, 1957 - 2007*. Retrieved from
http://www.fhwa.dot.gov/policyinformation/statistics/vm03_summary.cfm
- Federal Highway Administration. (2012). *Fact Sheet: I-35 Bridge Collapse, Minneapolis, MN*. Retrieved from <http://www.fhwa.dot.gov/pressroom/fsi35.cfm>
- Federal Highway Administration. (2014). *Tables of Frequently Requested NBI Information*. Retrieved from <http://www.fhwa.dot.gov/bridge/britab.cfm>

- Gilbert, J., & Balouchi, F. (2008). Comparison of energy harvesting systems for wireless sensor networks. *International Journal of Automation and Computing*, 334-347.
- Goswami, D., Kreith, F., & Kreider, J. (2000). *Principles of Solar Engineering*. Philadelphia: Taylor & Francis.
- Inamdar, S. (2012). *Design of a Solar Energy Harvesting System for Structural Health Monitoring Systems*. Master's thesis. University of Texas at Austin, TX.
- Infolytica Corporation. (2014). *MagNet v7*. Retrieved from infolytica:
<http://www.infolytica.com/en/products/magnet/>
- Jiang, X., Li, Y., & Li, J. (2013). Design of a novel linear permanent magnet vibration energy harvester. *2013 IEEE/ASME International Conference on Advanced Intelligent Mechatronics (AIM)* (pp. 1090-1095). Wollongong, NSW: IEEE.
- LASP. (2014). *Class 4 - Sunlight on Atmospheres*. Retrieved from Laboratory for Atmospheric and Space Physics (University of Colorado Boulder):
<http://lasp.colorado.edu/~bagenal/3720/CLASS4/4Sunlight.html>
- Lewis, N. (2007). Toward Cost-Effective Solar Energy Use. *Science*, 798-801.
- Li, H., & Pillay, P. (2007). A Linear Generator Powered from Bridge Vibrations for Wireless Sensors. *Industry Applications Conference, 2007. 42nd IAS Annual Meeting. Conference Record of the 2007 IEEE* (pp. 523-529). New Orleans: IEEE.
- Li, H., & Pillay, P. (2011). A Methodology to Design Linear Generators for Energy Conversion of Ambient Vibrations. *Industry Applications, IEEE Transactions on (Volume:47, Issue: 6)*, 2445-2452.

- Library of Congress. (2014). *Alternators made in Budapest Hungary*. Retrieved from Prints & Photographs Online Catalog (PPOC):
<http://loc.gov/pictures/resource/ppmsc.04414/>
- Lopez-Lapena, O., Penella, M., & Gasulla, M. (2010). A New MPPT Method for Low-Power Solar Energy Harvesting. *IEEE Transactions on Industrial Electronics*, 3129-3138.
- Lueke, J., & Moussa, W. (2011). MEMS-Based Power Generation Techniques for Implantable Biosensing Applications. *Sensors*, 1433-1460.
- Maehlum, M. (2014, September 24). *What Are the Most Efficient Solar Panels? Comparison of Mono-, Polycrystalline and Thin Film*. Retrieved from Energy Informative: <http://energyinformative.org/most-efficient-solar-panels-monocrystalline-polycrystalline-thin-film/>
- MathWorks. (2014). *Translational Friction*. Retrieved from Mathworks:
<http://www.mathworks.com/help/physmod/simscape/ref/translationalfriction.html>
- McEvoy, T. (2011). *Wind Energy Harvesting for Bridge Health Monitoring*. Master's thesis. University of Texas at Austin, TX.
- N.E. Bridge Contractors Inc. (n.d.). *About Us*. Retrieved from
<http://www.bridgeriggers.com/about-us>
- National Institute of Standards and Technology. (2009). *TIP Project Brief - Development of Rapid, Reliable, and Economical Methods for Inspection and Monitoring of Highway Bridges*.

- National Instruments. (n.d.). *NI WSN-3214 (Programmable)*. Retrieved from National Instruments: <http://sine.ni.com/nips/cds/view/p/lang/en/nid/210012>
- National Instruments. (n.d.). *Why Choose NI Wireless?* Retrieved from National Instruments: <http://www.ni.com/wsn/whychoose/>
- NIST-TIP. (2014). *Final Report: Development of Rapid, Reliable, and Economical Methods for Inspection and Monitoring of Highway Bridges*. National Institute of Standards and Technology.
- NREL. (2014). *Renewable Resource Data Center - Solar Resource Data*. Retrieved from National Renewable Energy Laboratory: http://www.nrel.gov/rredc/solar_data.html
- Patel, P., & Khamesee, M. B. (2013). Electromagnetic micro energy harvester for human locomotion. *Microsyst Technol* (2013), 1357-1363.
- Perpetuum. (n.d.). *Perpetuum Vibration Energy Harvester (VEH)*. Retrieved from <http://perpetuum.com/products/vibration-energy-harvester.asp>
- Phys.org. (2013, September 24). *World record solar cell with 44.7% efficiency*. Retrieved from Phys.org: <http://phys.org/news/2013-09-world-solar-cell-efficiency.html>
- Precision Magnetics, Inc. (2014). *Neodymium Iron Boron*. Retrieved from Precision Magnetics: <http://www.precisionmag.com/magnet-material/neodymium-iron-boron>
- Priya, S., & Inman, D. (2008). *Energy Harvesting Technologies*. New York: Springer.

- Reichenbach, M. (2012). *Evaluating Vehicular-Induced Vibrations of Typical Highway Bridges for Energy Harvesting Applications*. Master's thesis. University of Texas at Austin, TX.
- Saha, C., O'Donnell, T., Wang, N., & McCloskey, P. (2008). Electromagnetic generator for harvesting energy from human motion. *Sensors and Actuators A: Physical*, 248-253.
- Sanders, S. (2013, January 9). *BigBelly Solar Powered Smart Waste & Recycling System*. Retrieved from Gadget Review: <http://www.gadgetreview.com/2013/01/bigbelly-solar-powered-smart-waste-recycling-system/>
- Sazonov, E., Haodong, L., Curry, D., & Pillay, P. (2009). Self-Powered Sensors for Monitoring of Highway Bridges . *Sensors Journal, IEEE (Volume:9 , Issue: 11)* , 1422-1429.
- Seiko. (2014). *Kinetic Perpetual*. Retrieved from Seiko: <http://www.seikowatches.com/world/technology/kinetic/perpetual.html>
- Stephen, N. (2006). On energy harvesting from ambient vibration. *Journal of Sound and Vibration*, 409-425.
- Sun, Q., Patil, S., Stoute, S., Sun, N.-X., & Lehman, B. (2012). Optimum Design of Magnetic Inductive Energy Harvester and its AC-DC Converter . *Energy Conversion Congress and Exposition* (pp. 394-400). Realeigh: IEEE.
- Survival Universe. (n.d.). *Guardian Real Shake, Forever Flashlight*. Retrieved from Survival Universe: http://www.survivaluniverse.com/_A/5/Q/Guardian-Real-Shake-Forever-Flashlight-B000NNXQ5A.htm

- Tang, X., Lin, T., & Zuo, L. (2014). Design and Optimization of a Tubular Linear Electromagnetic Vibration Energy Harvester. *Mechatronics, IEEE/ASME Transactions on (Volume:19 , Issue: 2)*, 615-622.
- The National Bridge Inventory Database. (n.d.). *I-5 Skagit River Bridge Collapse*. Retrieved from National Bridges: <http://nationalbridges.com/i-5-skagit-river-bridge>
- von Buren, T., & Troster, G. (2007). Design and optimization of a linear vibration-driven electromagnetic micro-power generator. *Sensors and Actuators A*, 765-775.
- Weaver, J., Crawford, R., & Wood, K. (2010). Design of Energy Harvesting Technology: Feasibility for Low-Power Wireless Sensor Networks. *ASME 2010 International Design Engineering Technical Conferences*, (pp. 1-10). Montreal.
- Williams, C., & Yates, R. (1996). Analysis of a micro-electric generator for microsystems. *Sensors and Actuators A: Physical*, 8-11.
- Zimowski, K. (2012). *Next Generation Wind Energy Harvester to Power Bridge Health Monitoring Systems*. Master's thesis. University of Texas at Austin, TX.